IMPROVING MECHANICAL PROPERTIES OF Ti_{n+1}-A-C_n (A=Al or Si) MAX PHASES THROUGH SOLID SOLUTION STRENGTHENING AND FIBER REINFORCEMENT

A Dissertation

by

HUILI GAO

Submitted to the Office of Graduate and Professional Studies of
Texas A&M University
in partial fulfillment of the requirements for the degree of

DOCTOR OF PHILOSOPHY

Chair of Committee,	Miladin Radovic
Committee Members,	Ibrahim Karaman
	Hong Liang
	Haiyan Wang
Head of Department,	Andreas A. Polycarpou

August 2016

Major Subject: Mechanical Engineering

ABSTRACT

Ti_2AlC and Ti_3AlC_2 belong to the family of MAX phase and they are considered to be good candidates for high-temperature structural materials as they show excellent oxidation resistance up to 1450^oC, good damage tolerance and pseudo-ductile behavior. This Ph.D. dissertation reports on the reaction synthesis of Ti_2AlC and Ti_3AlC_2 and improvements on their mechanical properties by either solid solution strengthening due to substitution of Al with Si, or reinforcement with alumina ceramic fibers.

The reaction synthesis of Ti_2AlC from Ti-Al-TiC powder mixture was investigated in the temperature range of 700^oC and 1500^oC using pulsed electric current sintering (PECS). A bulk high-purity Ti_2AlC was successfully fabricated with fine grain microstructure through PECS in one step, possessing the highest fracture strength ever reported. However, no $Ti_2(Al_{1-x}Si_x)C$ solid solution could be sintered from Ti-Al-Si-TiC using pressureless sintering as they are thermodynamically unstable.

Because it is unpractical to improve the mechanical properties of Ti_2AlC by substitution of Al with Si, they were reinforced by addition of Nextel^{TM} 720 and Nextel^{TM} 610 alumina fibers. 20vol.% of Nextel^{TM} 720-Ti_2AlC and 20vol.% of Nextel^{TM} 610-Ti_2AlC composites with uniform distribution of short fibers were successfully fabricated using colloidal processing and densification through PECS. With addition of alumina fibers, the elastic modulus of Ti_2AlC was improved only slightly (by ~4.5%), while Vickers hardness and fracture toughness were enhanced significantly, i.e. for more than 35.8% and 15% in alumina fiber reinforced composites, respectively. In addition, results of mechanical testing in compression show that fabricated composites have higher compressive strength than the pure Ti_2AlC, for more than 16% at both room temperature and 1100°C. Therefore, result of this study implies strongly that alumina fibers can be used to improve mechanical properties of the Ti_2AlC at both room and high temperatures.

In order to expand the application of Ti_3AlC_2 MAX phase at high temperatures, a series of high-purity $Ti_3(Al_{1-x}Si_x)C_2$ solid solutions with $0<x<1$ and fine and coarse grained structure were reaction sintered PECS. It was found that c-lattice parameter and elastic moduli (both Young's and shear modulus) increase linearly with increasing amount of Si in those solid solutions. Regardless of grain size, Vickers hardness results demonstrate significant hardening effect in $Ti_3(Al_{1-x}Si_x)C_2$ solid solutions with a maximum around $Ti_3(Al_{0.5}Si_{0.5})C_2$. At room temperature, the strengthening effect was found to be marginal for fine grained (FG) structure with improvement of only 7.3%, but significant strengthening effect was observed in coarse grained (CG) one of ~25.8%. Above brittle-to-plastic transition (BPT) temperature, the solid solution strengthening effect diminishes and the strength of solid solutions is still higher than that of Ti_3AlC_2 but less than Ti_3SiC_2. Meanwhile, $Ti_3Al_{0.6}Si_{0.4}C_2$ forms a protective alumina oxide layer at 1200°C with comparable oxidation resistance to Ti_3AlC_2.

DEDICATION

To Deanna, Laura, and all my loving family

ACKNOWLEDGEMENTS

I would like to sincerely thank my advisor Dr. Miladin Radovic for his guidance, support and understanding during my graduate studies at Texas A&M University. Without his guidance and help, this dissertation would not be possible. I am really grateful that Dr. Radovic gave me the opportunity to join such a fascinating group.

I would also like to thank my committee members Dr. Ibrahim Karaman, Dr. Helen Liang, and Dr. Haiyan Wang for serving in my committee and for their helpful suggestions.

Additionally, I would like to thank all members in my group, Liangfa Hu, Rogelio Benitez, Morgan O’Neil, Lucas Alkmim Fagundes Santos, Peipei Gao, Junwei Xing, Amy Bolon, Yexiao Chen and Matthew Westwick for helping me in sample fabrication and training on MTS and RUS, etc. I also want to thank Dr. Raymundo Arroyave, Dr. Anjana Talapatra, Dr. Thien Duong, Woongrak Son, Dr. Anup Bandyopadhyay, Dr. Qing Su, Dr. Shujuan Wang, Nick Barta, and Dr.Ankush Kothalkar for assistance on modeling, XRD, TEM and Instron.

Finally, I appreciate the financial support from National Science Foundation (NSF) and Air Force Office of Scientific Research (AFOSR).

NOMENCLATURE

HRTEM	High-resolution transmission electron microscopy
PS	Pressureless sintering
HIP	Hot isostatic pressing
HP	Hot pressing
SPS	Spark plasma sintering
PECS	Pulsed electric current sintering
Pa	Pascal
MPa	Megapascal
LLC	Limited liability company
Amp	Ampere
WDS	Wavelength-Dispersive Spectroscopy
E	Young's modulus
G	Shear modulus
K	Degree of Kelvin
hr	Hour
SHS/PHIP	Self-propagating high-temperature synthesis with a pseudo hot isostatic pressing
XRD	X-ray diffraction
SEM	Scanning electron microscopy
EDS/EDA	Energy dispersive spectroscopy
EBSD	Electron back scattered diffraction
H_v	Vickers hardness

BPTT	Brittle-to-plastic transition temperature
PDS	Plasma discharge sintering
EDM	Electrical discharge machining
TEM	Transmission electron microscopy
CTE	Coefficient of thermal expansion
RUS	Resonant ultrasound spectroscopy
DSC	Differential scanning calorimetry
TMA	Thermomechanical analysis
MTS	Materials testing system
UCS	Ultimate compressive strength
PAA	Polyacrylic acid
SHPB	Split-Hopkinson pressure bar
FG-	Fine grain
CG-	Coarse grain

TABLE OF CONTENTS

Page

LIST OF FIGURES

LIST OF TABLES

1. INTRODUCTION

1.1 General Introduction on MAX Phases

$M_{n+1}AX_n$ phases (n = 1 to 3) [1] are a family of nanolaminated ternary nitrides and carbides, where M is an early transition metal, A is an A-group element, and X is either carbon or nitrogen, with a hexagonal crystal structure that belongs to a P63/mmc space group in Figure 1 [2]. The crystal structures of M_2AX, M_3AX_2 and M_4AX_3 phases, in Figure 2 [3], show that MAX phase's structure consists of $M_{n+1}X_n$ inter-layered with A element layers and X elements that are located in every second octahedral site in $M_{n+1}X_n$ layers [1]. The high-resolution transmission electron microscopy (HRTEM) image of Ti_3SiC_2 in Figure 3 clearly illustrate their unique nano-layered structure [3].

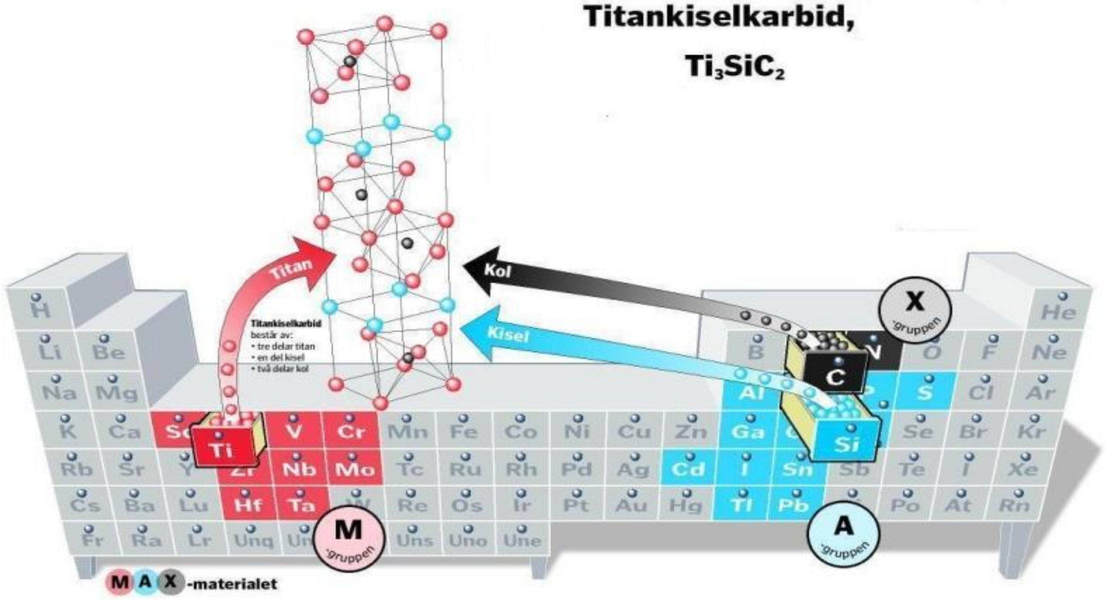

Figure 1 MAX phase elements in periodic table and its typical structure of Ti_3SiC_2 MAX phase [2].

Since the first MAX phase was discovered in the powder form in the early 1960s by Nowotny and his coworkers [4], more than 70 MAX phases with different compositions have been synthesized [2]. Nowadays, the MAX phases family is composed of 50 M_2AX, 6 M_3AX_2, 7 M_4AX_3, even newly discovered $Ti_5Al_2C_3$, and over approximately 100 MAX phases solid solutions on M, A or X site [2, 5, 6].

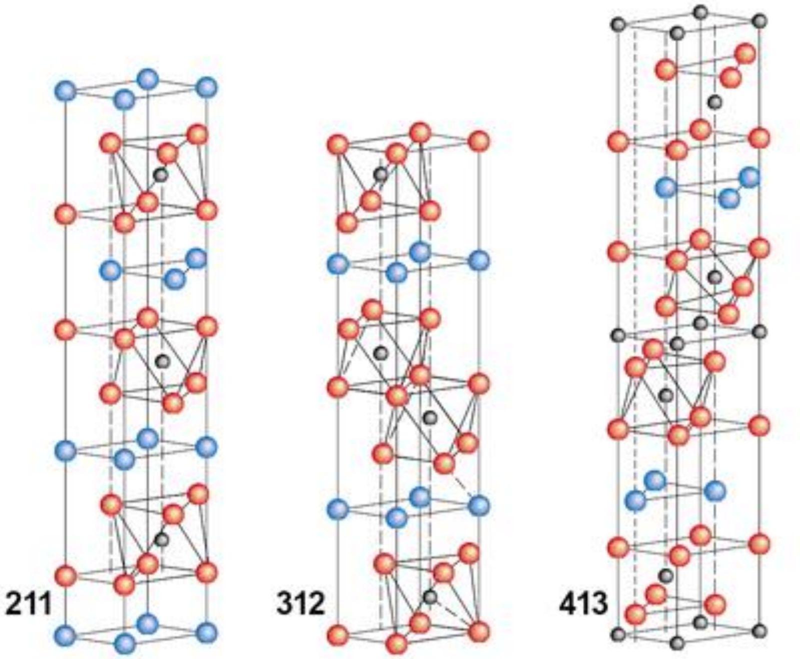

Figure 2 Schematic structure of M_2AX, M_3AX_2 and M_4AX_3 [3].

The MAX phases are sometimes called "metallic ceramics " and they are growing attention nowadays due to their unique combination of properties that sometimes bridge between properties of typical ceramics and metals [2]. Typically, the MAX phases have high stiffness, good thermal shock and chemical resistance, excellent machinability, and high thermal and electrical conductivity, etc [7]. The most intriguing property of MAX phases is their nonlinear elastic behavior, in which a cycling loading of the MAX phases results in a spontaneously reversible, hysteretic stress-strain loop [2].

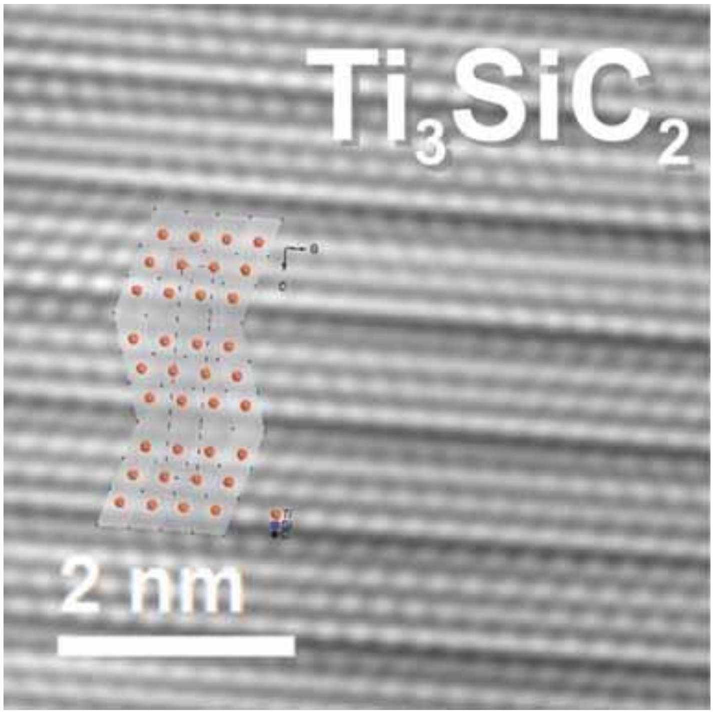

Figure 3 High resolution TEM image on Ti_3SiC_2 sample.

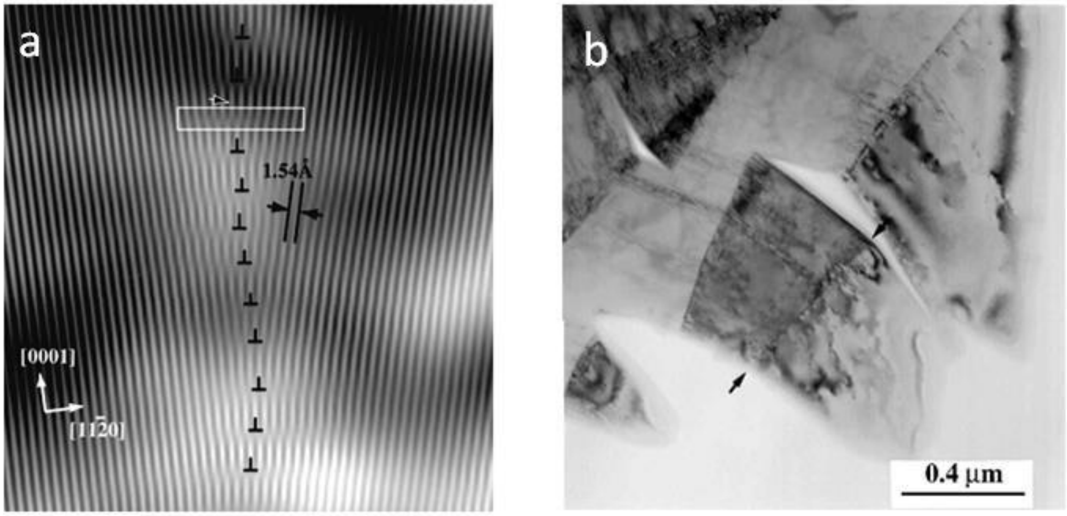

Figure 4 (a) TEM image shows basal plane dislocations arranged in a wall; (b) The kink band forming in Ti_3SiC_2 at room temperature [8].

The unique mechanical properties and good machinability of MAX phase are attributed to two types of atomic defects that are commonly observed in their structure, namely basal dislocation and stacking faults, in Figure 4 [9-12]. Due to the their unique anisotropic layered structure and high c/a ratio, the dislocations with the Burger vector is 1/3<11-20> are confined to form and glide easily only in the basal planes [11, 12]. The stacking faults are also confined to the basal plane and forms as the result of the dissociation of a perfect dislocation into two partials [10]. Therefore, some of the salient points are needed to understand mechanical behavior of the MAX phases can be summarized as following:

1. All dislocations are only mobile and multiply in basal planes at all temperature [10]. And their Burger vector is 1/3<11-20>. Therefore, the MAX phases have less than five independent slip systems that are needed for accommodating grain-to-grain constraints during plastic deformation;

2. These basal planes dislocations are mobile, and can multiply and arrange themselves either as pile-ups along slip plane, or in dislocation walls normal to arrays [8, 11];

3. Because of high c/a ratio, MAX phases cannot deform by twinning. However, they can be deformed by kinking and kind band formation. The later makes their mechanical properties different from the traditional brittle materials and other materials with less than 5 independent slip systems [10, 13].

4. Finally, they can delaminate by cleavage along basal planes which is much easier than along any other planes [2].

Kinking and kink band formation have been considered to be most important deformation mechanisms in MAX phases that are in large part responsible for their unusual mechanical behavior. The kink bands were first found by Orowan in single crystal of Cd and Zn [14]. Kink bands consist of regularly spaced basal dislocations arranged into two dislocation walls of opposite signs. The exact mechanism of kinking formation is still not clearly understood. However, it is postulated that they form in the bulked grains as incipient kink bands (IKBs), Figure 5a [15], grow with increasing stress until dislocation walls reach grain boundaries and develop into the full kink bands (KB). Figure 5b-c illustrate development of IKB into the full KB. Blue grains in Figure 5b-c represent soft grain, because their basal planes are oriented 45^o relative to the applied compressive stress, i.e. they have high Schmid factor for dislocation glide in basal plane. Therefore, the local stress in soft grains readily achieve critical resolved shear stress during loading, resulting into dislocation glide or slip along the basal planes. However, those red grains with basal planes paralleled to direction of applied compressive load are referred as hard grains. Once the stress in those hard grains reaches the critical value, they will buckle and IKBs would nucleate and grow until they meet the grains boundaries forming fully developed KB, like in Figure 5c. Then the region between two dislocation walls in KB can deform by formation of additional KBs. The latter results in the formation of low angle kinking boundaries (LAKB), Figure 5d.

On the other hand, the formation of KB is usually accompanied by delaminations along basal planes, as illustrated in Figure 6 [10, 11, 15]. Delaminations were observed at the intersection of the dislocation walls and arrays, to eliminate the latter and resulting in large strain energy releases [10, 11, 15].

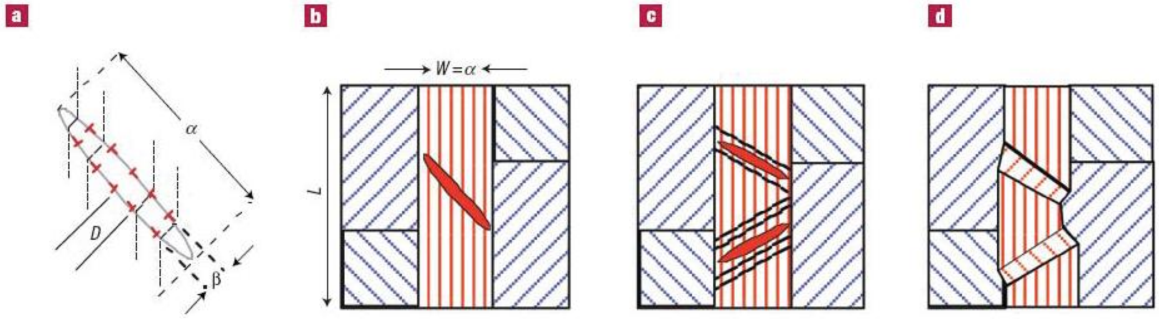

Figure 5 The formation of kink bands. (a) The formation of IKBs consisting of two dislocation walls with opposite sign; (b) The formation of an Initial Kink Band in hard grain; (c and d) Schematic of the development of IKB into full KB [15].

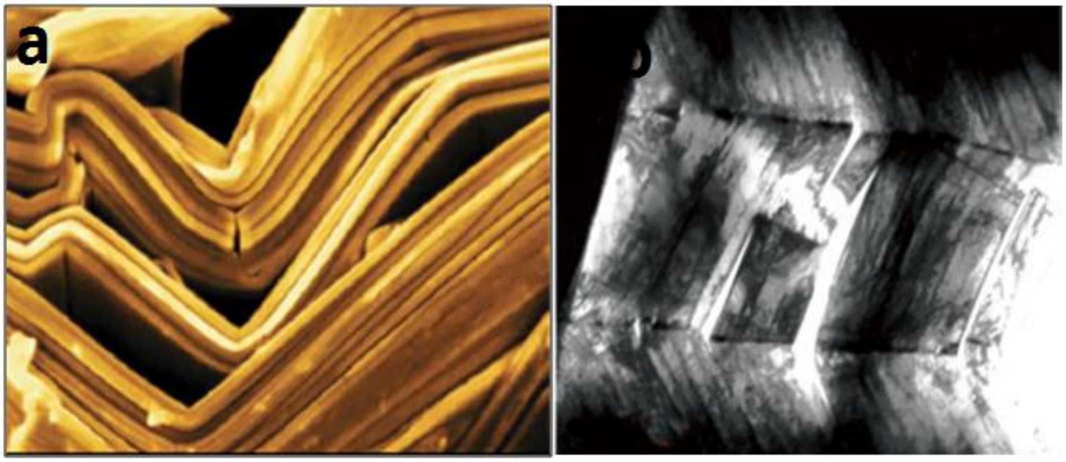

Figure 6 (a) SEM image of typical kink and delamination in Ti_3SiC_2 [16]; (b) Bright-field transmission electron microscopy image of a kink band with a high misorientation (stove-pipe) angle containing elimination cracks [11].

1.1.1 Microscale Model for Kinking Nonlinear Elasticity

The most intriguing property of MAX phases is their nonlinear and hysteretic stress-strain behavior that was always observed during cyclic loading in compression or tension tests even at room temperature, like Figure 7 [2, 17, 18]. When MAX phases are subjected to cyclic loading and unloading, their stress-strain curves do not obey the Hook's law like other stiff ceramics, but rather they form hysteresis loops that are fully closed and strain-rate independent [19, 20]. The shape and size of these hysteretic loops are strongly dependent on the grain sizes, i.e. the larger is grain size, the larger hysteresis loop at the same stress level in Figure 7 [21, 22]. The area of stress-strain loops present mechanical energy dissipated in each loading cycle, and for some MAX phases, it can be up to 25% of total stored mechanical during cyclic loading. Such a large energy dissipation during cyclic loading is typical for some polymer (i.e. propylene and nylon) [23, 24] , but not for stiff and brittle ceramics. As their hysteresis behavior is believed to be result of attributed to formation of IKBs and KBs, they are sometimes referred to as Kinking Nonlinear Elastic (KNE) solids [15, 18, 20, 25].

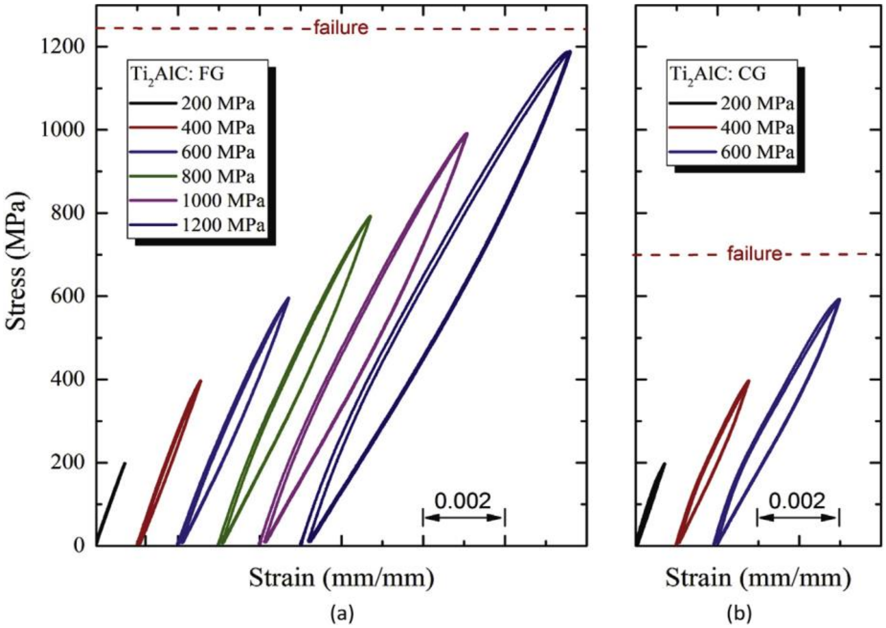

Figure 7 Typical stress-strain behavior (a) fine grain structure and (b) coarse grain Ti_2AlC in compression test [26].

To explain the hysteretic behavior in MAX phases, Barsoum et al. [15, 18, 20, 25] proposed a microscale model referred to as kinking nonlinear elastic model. This KNE model was build on Frank and Stoh's theory [27], assuming that the formation, growth of IKB during loading and their annihilation in unloading results in the observed energy dissipation, and hysteretic stress-strain behavior. According to this model, the total strain ϵ_{tot} during loading-unloading can be described as:

$$\epsilon_{tot} = \sigma/E+\epsilon_{IKB}+ \epsilon_{DP} \qquad 1.1$$

where, σ/E is the linear elastic strain; ϵ_{IKB} is nonlinear strain due to IKBs formation in the hard grains; and ϵ_{DP} is nonlinear strain due to dislocation pileups in the soft grains, in Figure 8. Both nonlinear strains are fully reversible and we only discuss ϵ_{IKB} in the following [18].

Based on KNE model, IKBs forms elliptical structure of nested dislocations loops as shown in Figure 8a-b, with length of 2α and width of 2β [18, 27], and they grow to the fully developed KB once the remote critical shear stress reaches critical value (τ_t) of :

$$\tau_t \approx \frac{\sigma_t}{M} = \sqrt{\frac{4G^2 b\gamma_c}{\pi^2 2\alpha} \ln \frac{b}{w\gamma_c}} \qquad 1.2$$

where, M is Taylor factor that is equals 3 for randomly oriented polycrystalline structure, while b, G, w and γ_c are Burger vector, shear modulus, dislocation core width, and critical kinking angle, respectively.

For MAX phases, 2α is considered to be equal to the grain thickness (or grain width) along [0001] direction [28], and γ_c critical kinking misorientation angle defined as [27, 29]:

$$\gamma_c = b/D \approx \frac{3\sqrt{3}(1-\upsilon)}{8\pi e}\left(\frac{b}{w}\right) \qquad 1.3$$

where, υ is Poisson's ratio. If one assumes that $w = b$, the γ_c is 3°. On other hand, If $w = 5b$, the γ_c is on the order of 0.57rad, which is rather small [30].

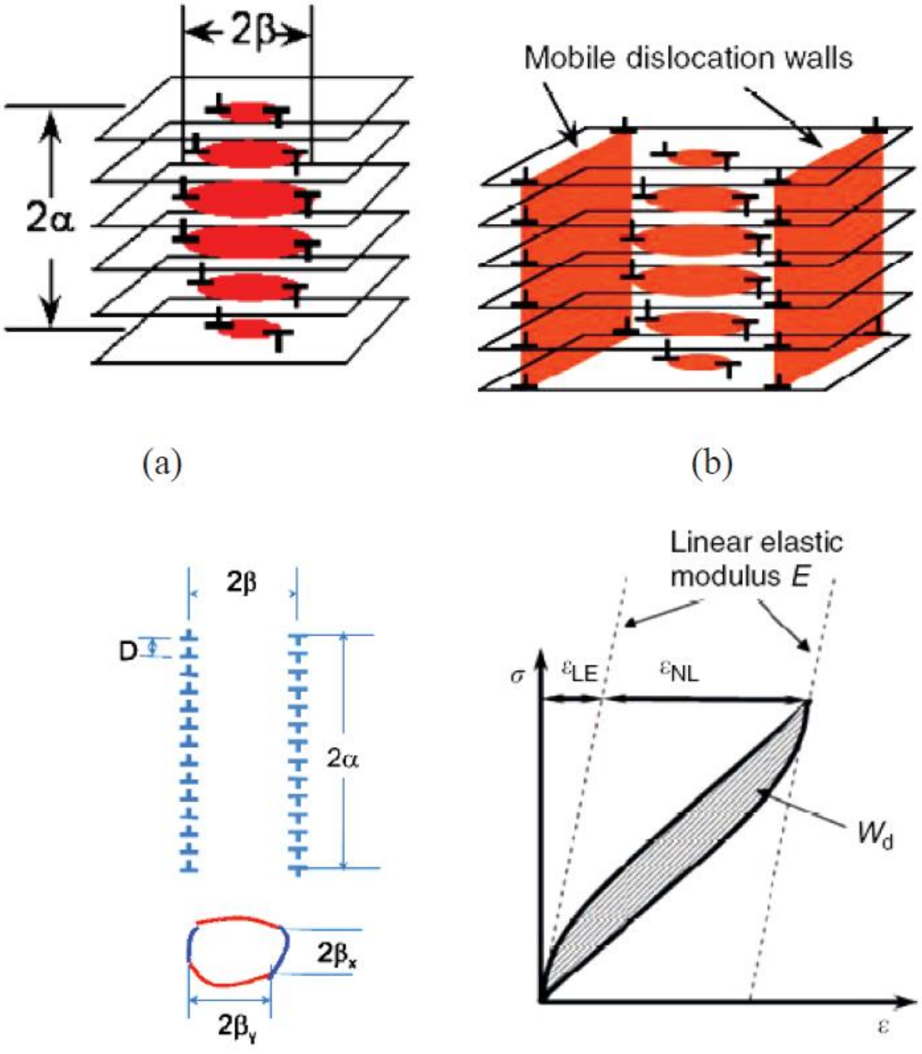

(a) (b)

(c) (d)

Figure 8 (a) Schematic of an IKB in ellipsoid shape with the length of 2α and diameter of 2β, (b) MDWs confining a fully developed KB, (c) dislocation walls and dislocation loops of an IKB and (d) typical stress-strain loop [31].

Furthermore, if we assume that IKB consists of several parallel dislocation loops and that each loop is made up of two edge and two screw dislocations segments with length of $2\beta_x$ and $2\beta_y$, respectively [27, 30], as it is shown in Figure 8c.

$$2\beta_x \approx \frac{2\alpha(1-v)}{G\gamma_c}\frac{\sigma}{M} \text{ and } 2\beta_y \approx \frac{2\alpha}{G\gamma_c}\frac{\sigma}{M} \qquad 1.4$$

The formation of an IKB can be separated into two segments: nucleation and growth. Because the nucleation process is still unclear, KNE model only consider IKB growth from $2\beta_{xc}$ and $2\beta_{\gamma c}$ to $2\beta_x$ and $2\beta_{\gamma c}$, respectively [17, 32], Figure 8a - c. Therefore, the IKB-induced axial strain resulting from their growth when remote stress σ is larger than threshold stress σ_t can be expressed as :

$$\varepsilon_{IKB} = \frac{\Delta V N_k \gamma_c}{k_1} = \frac{N_k \gamma_c 4\pi\alpha\left(\beta_x\beta_\gamma - \beta_{xc}\beta_{\gamma c}\right)}{3k_1} = \frac{4\pi(1-v)N_k\alpha^3}{3k_1 G^2 \gamma_c M^2}\left(\sigma^2 - \sigma_t^2\right)$$

$$= m_1\left(\sigma^2 - \sigma_t^2\right) \qquad 1.5$$

where, m_1 is an constant that can be determined by plotting experimentally measured ϵ_{IKB} (Figure 8b) vs σ^2-$\sigma_t{}^2$, N_k is the number of IKB per unit volume, ΔV is volume change as the IKB grow from critical size σ_c to their size at σ.

The dissipated energy per unit volume is due to formation and annihilation of IKB, can be then expressed as [17, 32] :

$$W_d = \frac{4\Omega\pi N_k\alpha}{D}\left(\beta_x\beta_\gamma - \beta_{xc}\beta_{\gamma c}\right) = \frac{4\pi(1-v)N_k\alpha^3}{3k_1 G^2\gamma_c M^2}\frac{\Omega}{b}\left(\sigma^2 - \sigma_t^2\right)$$

$$= m_2\left(\sigma^2 - \sigma_t^2\right)$$

1.6

where m_2 is an constant that can be determined by plotting experimentally measured dissipated energy as a area of dislocation loops (Figure 8c) vs. $\sigma^2 - \sigma_t^2$. This model also predicts that dissipated energy is linear function of ε_{IKB}, which is linear function of ε_{IKB} in Figure 9.

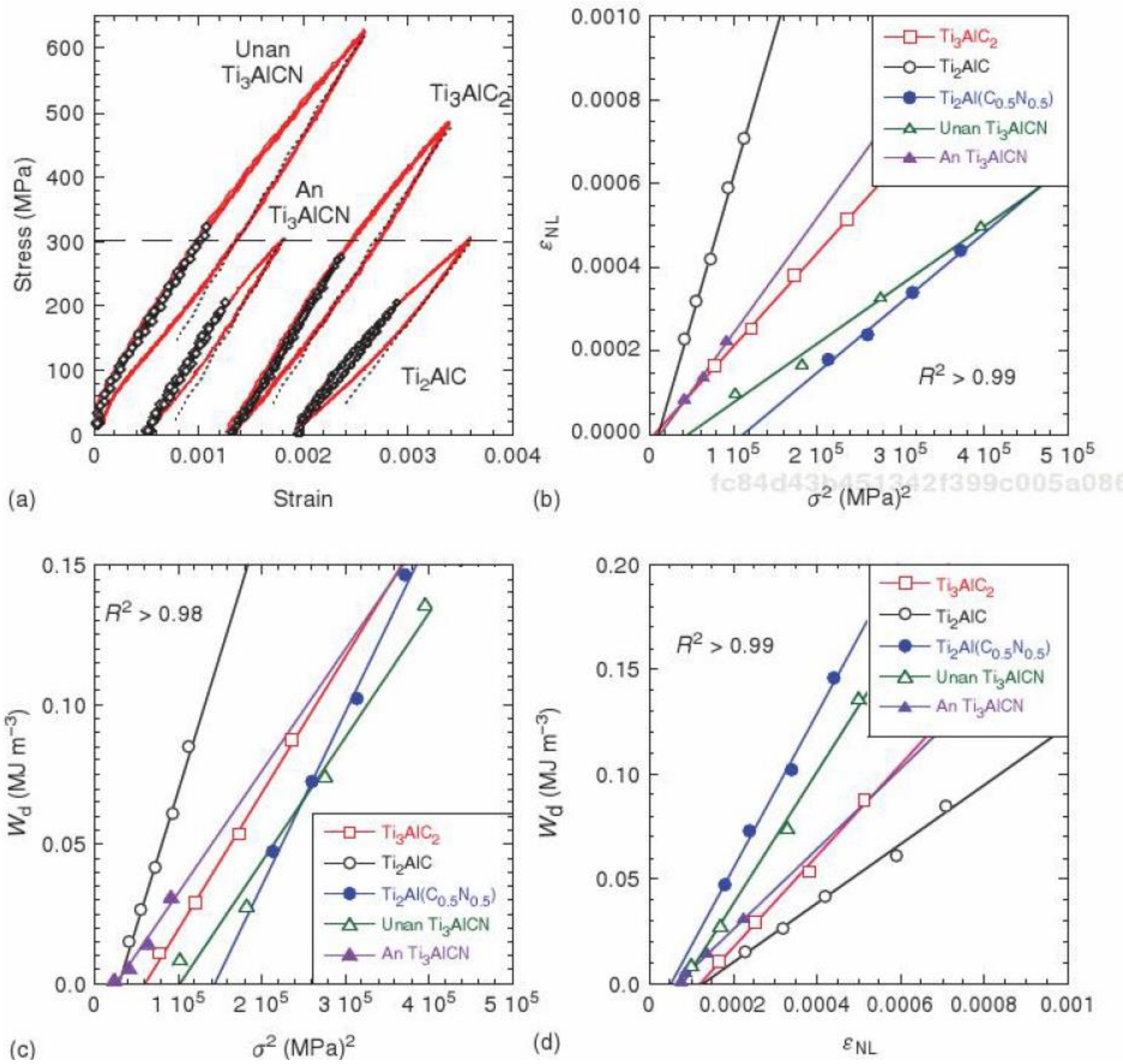

Figure 9 (a) Cyclic compressive stress-strain curves for MAX phase; (b) ϵ_{NL} vs. σ^2; (c) W_d vs. σ^2 ; (d) W_d as a function of ϵ_{NL}[9].

This model is in good agreement with experimental results that the dissipated energy per unit volume per cycle and the non-liner elastic strain should be proportional to σ^2 , and the dissipated energy should be linear function of the non-liner elastic strain.

In addition it allows to determine $N_{k,}$ ΔV and Ω/b from constant m_1 and m_2. More impotently, IKB model also predicts that Ω/b should be proportional, if not equal to the critical resolved shear stress in the MAX phase's basal planes.

1.1.2 Mechanical Behavior at Room and High Temperatures

In the following section, the mechanical properties of MAX phases at ambient temperature are summarized briefly [13, 33]. Our current understanding of their mechanical properties is based on the fact that individual MAX phase single crystals are highly plastically anisotropic, as dislocation can form and easily glide only in the basal plans and they can arrange themselves in the dislocation pile ups in the basal planes or dislocation walls. The later is important for the formation of KB.

It was demonstrated in previous studies that highly-oriented Ti_3SiC_2 samples with an average grain of 2mm, the samples yielded at 200 MPa even at room temperature when the basal planes oriented ~45^o relative to the direction of applied compressive stress [11]. In this loading case, deformation exceeding 10% can be reach due to easy glide of dislocations in the basal planes. However, if the slip (basal) planes were parallel with the applied compressive stress, a significant strain-softening can be observed after reaching the maxima of 290 MPa, due to kinking and KB formation. Once KB forms, the sample deforms plastically due to shear-bend formation at almost constant stress of 200 MPa. The microstructural analysis of the highly oriented Ti_3SiC_2 samples after decohesion testing in different directions also confirmed that the deformation of MAX phases are controlled by KB formation, delaminations within individual grain, and shear-band formation.

When polycrystalline MAX phases were tested in compression at room temperatures, their mechanical behavior is strongly dependent on grain size and strain rates. Previous results [21, 33, 34] showed that the ultimate compressive strength is a function of grain size and obeys the Hall-Petch law, i.e. the compressive strength decreasing grain size [35]. On the other hand, not all MAX phases fail suddenly, CG-samples exhibit very graceful failure with strains to failure reaching up to 2% before failure [2].

Although MAX phases possess an interesting properties at room temperature, the high-temperature properties also attract more and more attention. In this paragraph, the mechanical properties at high temperatures were understood and clarified. At high temperatures, all MAX phases would undergo a brittle to plastic transition (BPT) [2]. The BPT temperatures are different from phase to phase, but for most containing Al- and Si- MAX phases, they lie between 900-1100^{o}C [33, 36, 37]. Above BPT temperature, not only the strength and the fracture toughness drop significantly, but also they can be plastically deformed up to 25% even in tension [35]. The nature of BPT transition is not still clear at this point. It was proposed that activation of temperature-dependent grain boundary decohesion and/or delamination together with grain boundary sliding results in BPT [2, 21, 38]. Most recently, it has been postulated that activation of the secondary slip systems causes BPT [39]. However, the later cannot explain the observed drop in fracture toughness above BPT temperature.

1.2 Synthesis of Selected MAX Phases

1.2.1 Ti_2AlC MAX Phase

Since Ti_2AlC was first discovered in late 1960s [4], it has been one of the most important MAX phase among over 70 known to date. Its remarkable physical properties of Ti_2AlC MAX phase are summarized in Table 1. Ti_2AlC has a low density of 4.1 g/cm^3 [1], a high Young's modulus and shear modulus of 277 GPa and 119 GPa, respectively [40], and excellent thermal and electrical conductivity of 46×10^{-6} W/K and 2.8×10^{6} S/m [41]. Ti_2AlC is one of the most promising choice for the high temperature application. One of the most important characteristics of Ti_2AlC is its excellent long-term oxidation resistance and a self-healing ability at elevated temperatures, which resulted from the formation of an adherent continuous layer of alumina on the surface during oxidation [42]. Meanwhile, Ti_2AlC possesses adequate mechanical properties with a reported compressive strength between 540 – 763 MPa [1, 36], the flexural strength of 430 MPa [36], and the fracture toughness of 6.5 MPa*m$^{1/2}$ [36]. The brittle-to-plastic transition temperature (BPTT) is reported between 900–1000^{o}C under the flexural load [43].

Barsoum et al.[36] synthesized for the first time a high-purity Ti_2AlC sample from $Ti:Al_4C_3:C$ powder mixtures by HIP and HP at 1600^{o}C for 4 hours. X-ray diffraction (XRD) results showed that their samples were the single phase pure MAX phase. Later on, Mei et al. also synthesized a high-purity bulk Ti_2AlC sample using a simpler procedure. They reaction sintered from the 2Ti: 1.2Al: 1C powder mixture by HPing at 1100^{o}C for only one hour [44]. More recently, the SHS/PHIP (combustion synthesis/pseudo heat isostatic pressing) method has been developed to fabricate Ti_2AlC

from a 2.9Ti:2Al:1C powder mixture at load of 420 MPa for 10–15s by Bai et al. [45]. They, as many researchers after them, added more Al (10-20%) in initial powder mixture to compensate for the Al loss during sintering because it melts and evaporates well below sintering temperature, i.e. at 660°C. All samples described above were analyzed by XRD without any microscopic analysis (e.g. secondary electron and back scattered microscopy). However, as it was pointed out earlier [36], even XRD pure Ti_2AlC can contain large amount of secondary phases because it is difficult to differentiate $TiAl_x$, Ti_3AlC_2 and Ti_2AlC only through XRD analysis. This difficulty comes from the fact that some of the XRD peak positions of impurity phases are very close to those of Ti_2AlC and because $TiAl_x$ can give very broad peaks due to high deviation from stoichiometry. Therefore, to more precisely examine the purity of the Ti_2AlC samples, more thorough analysis, including Scanning Electron Microscopy (SEM) with Energy-Dispersive Spectroscopy (EDS), Wavelength-Dispersive Spectroscopy (WDS) and/or Electron-Backscatter Diffraction (EBSD) should be performed in addition to XRD analyses. More recently, Dubois et al. demonstrated that a non-stoichiometric Ti_2AlC_x can be synthesized from a powder mixture of 2Ti:1.05Al:0.85C by HIPing, based on thorough XRD and SEM analysis of samples [46]. More importantly, they showed that purity of final Ti_2AlC is very sensitive to processing conditions, especially composition of the initial powder mixture that has to be carefully optimized to fabricate high purity single phase samples.

1.2.2 Ti_3AlC_2 MAX Phase

Bulk Ti_3AlC_2 was first discovered by Pietzka and Schuster et al. in 1994 [47], and the typical properties of Ti_3AlC_2 are listed in Table 1. Ti_3AlC_2 is one of the best characterized MAX phases that is usually considered one of the most representative members of this family of ternary carbides. It has high Young's modulus and shear modulus of 297 GPa and 124 GPa, respectively [48]. Its Vickers hardness is about 3.5 GPa, i.e. it is a little softer than Ti_3SiC_2. The room-temperature electricity resistance at is 0.35 ±0.03 μΩ*m and the coefficient of thermal expansion in temperature range of -20 to 1200°C is $9.0\pm0.2*10^{-6}\ K^{-1}$. The compressive strength was reported to be between 560 - 768 MPa at room temperature [34, 48]. The flexural strength and fracture toughness are 552 MPa and 9.1 $MPa*m^{1/2}$, respectively [49]. The BPT temperature in Ti_3AlC_2 was reported to be in the temperature range of 1000-1050°C, above which compressive strength decreases significantly to 200 MPa [50]. At high temperature, it oxidizes and forms a surface oxide layer that is mixture of Al_2O_3 and TiO_2 due to the outward diffusion of Al [51]. Formation of predominately Al_2O_3 was reported to contribute to the crack self-healing in Ti_3AlC_2 during oxidation [52].

Like Ti_2AlC, Ti_3AlC_2 is also fabricated through pressureless sintering, HIPing, HPing, SPSing and the novel method such as combustion synthesis. In 2009, Zhou et al. claimed that Ti_3AlC_2 can be pressureless-sintered at 1450°C for 150 minutes from 3Ti:1.1Al:1.88C powder mixture that was embedding in Al_4C_3 powders [53]. This study showed that high-density and high purity Ti_3AlC_2 sample can be fabricated without decomposition due to Aluminum-rich atmosphere in sintering chamber. In 2000, Tzenov et al.[48] fabricated the high-purity polycrystalline Ti_3AlC_2 from the mixture of Ti:Al_4C_3:C through HIP at 1400^{o}C for 15 hrs. Their samples had grain size of 25 μm and 4.8 vol.% Al_2O_3 impurity. Wang et al.[50] prepared pure phase Ti_3AlC_2 from 3Ti:1.1Al:1.8C powder mixture by solid-liquid reaction synthesis in HP at 1500^{o}C for 5 mins in 2002. The reaction mechanism that they proposed includes formation of Ti-Al intermetallics at about 740^{o}C that subsequently reacts with TiC resulting in only Ti_3AlC_2 phase at 1500^{o}C. Zhou et al. also demonstrated for the first time that Ti_3AlC_2 can be successfully synthesized by HP and SPS from Ti, Al_4C_3 and C powders as starting materials. Their final product after SPSing contained Ti_2AlC, Ti_3AlC_2 and TiC phases, and their amount varied with soaking time and soaking temperature [54]. A powder mixture of 7Ti/Al_4C_3/3TiC was used for synthesis of Ti_3AlC_2 through pulsed discharge sintering (PDS) by Zou et al.[55] via the reaction of the intermediate phases and TiC resulting in the samples with grain width of 5 -10 μm and length of 50 μm. In 2008, Han et al.[56] indicated that polycrystalline bulk Ti_3AlC_2 can be fabricated by HP from TiC_x and Al powders. The main fabricated phase using this method was Ti_3AlC_2, with a small amount of Ti_2AlC as secondary phase. They also found that with increasing the temperature, Ti_3AlC_2 partially melts at 1600^{o}C. Samples processed using this approach also had higher flexural strength of over 900 MPa and higher Vickers hardness of about 4.5 - 6.5 GPa, i.e. higher than those previously published in the literature, most likely due to finer grain size and the secondary nano-sized phase reinforcement, such as residual TiC_x and Ti_2AlC [56]. Zhu et al. claimed to fabricate the high-purity Ti_3AlC_2 from TiC/Ti/Al powder mixtures in one step through SPS. They also showed that addition of small amount of Si improved the synthesis of Ti_3AlC_2 and the fracture toughness [57]. Later on, Chen et al. developed fabrication of Ti_3AlC_2 from 3Ti:1.2Al:2C powder mixture with TiC addition by combustion synthesis [58].

1.2.3 Ti_3SiC_2 MAX Phase

Ti_3SiC_2 was synthesized for the first time in 1967 through chemical reaction method by Nowotny et al.[4]. Like other MAX phases, it has the hexagonal crystal structure with space group of P63/mmc but with a-lattice parameter 3.06Å and c-value 17.67Å. The density of $Ti_3SiC_2$is 4.5 g/cm^3. Ti_3SiC_2 is the best characterized MAX phases and its mechanical properties seems to be much better when compared to other MAX phases. For example, its compressive strength reaches over 1 GPa [15].

In 1996, Barsoum et al.[59] demonstrated that bulk Ti_3SiC_2 can be fabricated from Ti, C and SiC powders mixture through HP. Their samples had compressive strength of 600 MPa at room temperature, which dropped to 260 MPa at 1300^{o}C. In addition, they measured high room-temperature electrical and thermal conductivities of $4.5*10^6\ \Omega^{-1}m^{-1}$ and 43 W/(m*K), respectively, for the first time for one of the MAX phases. In addition, they reported coefficient of thermal expansion and heat capacity for Ti_3SiC_2 of $10*10^{-6}\ K^{-1}$ and 588 J/(kg*K), respectively [59]. El-Raghy et al. also studied the grain size effect on Ti_3SiC_2 phase fabricated from Ti/C/SiC powder mixtures . Reaction HIPing of this powder mixture at 1450^{o}C and 1600^{o}C for 4hrs, resulted in samples with fine grained (FG) structure with 3-5 µm grains and coarse grained (CG) structure with 100-200 µm grains, respectively. Both microstructures exhibited excellent damage-tolerant properties and the brittle-to-plastic transition (BPT) temperature at around 1200°C [33]. However, CG samples were much more thermal shock resistance than FG ones.

In 2002, Zhang et al. fabricated Ti_3SiC_2 from 5Ti/2Si/3C and 2Ti/2Si/3TiC powder mixtures at 1400°C through PDS, and in their best cases it resulted in pure phases with TiC content ranging between 2 wt.% and 6 wt.% [60]. Pampuch et al. synthesized Ti_3SiC_2 from 3Ti:Si:2C powder mixtures through solid combustion synthesis and their final product contained small amount of TiC and with equiaxed grain at a size of 1-5 μm. They also demonstrated an excellent resistance to oxidation combined with good thermal shock and tolerance of Ti_3SiC_2 [61].

A thorough review of the literature on reactions synthesis of Ti_3SiC_2 suggests that it is quite difficult to process this MAX phase without any ancillary TiC impurity. This is because that Ti_3SiC_2 was formed from the layer of Si inserted into Ti_3C_2 layers that are closely related to the structure of TiC [62]. Therefore, there was always ancillary TiC impurity during Ti_3SiC_2 processing.

1.3 Properties and Applications of Selected MAX Phases

Table 1 is the typical properties of selected-Ti_2AlC, Ti_3AlC_2, and Ti_3SiC_2 MAX phases, which are three of the most promising candidate for structure application among all MAX phases by now. All three MAX phases possess a combination of traditional ceramic and metal properties, such as high hardness, good thermal shock resistance, machinablity, and good electrical and thermal conductivity, etc [2, 13, 20, 63].

Table 1 The typical properties of Ti_2AlC, Ti_3AlC_2, and Ti_3SiC_2 MAX phases.

	Ti_2AlC	Ti_3AlC_2	Ti_3SiC_2
Lattice parameter (A)	a = 3.05Å c = 13.64 Å	a = 3.07 Å c = 18.58 Å	a = 3.06 Å c = 17.67 Å
Density (g/cc)	4.11[36]	4.25	4.50
Vickers hardness (GPa)	4.7[45]	3.5	4-5
Young's modulus (GPa)	277[40]	297[48]	339[64]
Shear modulus (GPa)	119[40]	124[48]	143[64]
Compressive strength (MPa)	540-763[1, 36]	560-768 [34]	1000[33]
Fracture strength (MPa)	430[36]	552[49]	600[33]
BPTT (°C)	900-950[43]	1000-1050	1000-1050[33]
Electrical resistance (μΩ·m)	0.36[36]	0.35[48]	0.0227[2]
Thermal conductivity (W/K)	46[2]	40[2]	34[2]
Thermal expansion coefficient ($10^{-6}K^{-1}$)	8.2-8.8[2, 36]	9.0±0.2[48]	9.1[2]
Fracture toughness ($MPa/m^{1/2}$)	6.5[36]	9.1[49]	-

Of the three, Ti_2AlC has the lowest density with the best oxidation resistance at elevated temperature due to a formation of continuous alumina layer on the surface [42, 65]. Meanwhile, Ti_3AlC_2 also has as good oxidation resistance as Ti_2AlC with a formation of continuous alumina layer on the surface at elevated temperature [42, 66]. Those properties triggered the interest of the research community in Ti_2AlC and Ti_3AlC_2 as potential high-temperature materials candidate. Both were regarded as potential materials for high temperature applications, such as heating elements, gas burner nozzles, oxidation resistant films for coatings, etc [9, 67]. Among those three MAX phases, Ti_3SiC_2 is the worst oxidation resistance, but the best mechanical properties at high temperature with higher BPT temperature [68, 69]. Ti_3SiC_2 was used for electrical contacts, glove molds, concrete drilling, non-stick coatings in cooking and cladding materials for nuclear applications, etc [9, 70].

1.4 Problem Statement

Up to now, over 70 MAX phases have been discovered without consideration MAX solid solutions [70]. With consideration of substitution on M, A and X sites, there are over millions of possible MAX phases waiting to be synthesized and characterized [9]. Several methods are used to synthesize bulk MAX phases, such as pressureless sintering (PS) [53, 71], hot isostatic pressing (HIP)[36], hot pressing (HP), pulse electric current sintering (PECS) [60, 72], and combustion synthesis with HIPing. Compared with all these traditional methods, PECS-commonly but inadequately referred to as spark plasma sintering (SPS) is also one of the most popular and efficient processes-offering less energy consumption, short reaction time and simple procedure, i.e. reactive sintering and densification in one step. The goal of this work is to synthesize the bulk high-purity MAX phase from elemental powders by utilizing PECS and to explore the strengthening mechanism of MAX phases between microstructure and mechanical behavior.

Although there are over hundreds of studies on synthesis and mechanical characterization of Ti_2AlC MAX phase [43], the reaction mechanism of Ti_2AlC is still not clearly understood, especially by PECS. Even though Ti_3AlC_2, Ti_3SiC_2 and Cr_2AlC have been successfully fabricated through PECS from elemental powders [49, 60, 66], Ti_2AlC was only reported to be synthesized in two papers without detail microstructural analysis [73, 74]. From the Ti-Al-C ternary phase diagram [75], several compounds are competing with Ti_2AlC such as TiC, Ti_3AlC_2, Ti_3AlC, Al_4C_3 and $TiAl_x$, where x=0-1. As known, the impurities such as TiC and $TiAl_x$ play an important role on mechanical properties and oxidation resistance of Ti_2AlC, especially above the BPT temperature. Therefore, the first goal of this study is to synthesize the high-purity Ti_2AlC, to study the reaction mechanism from elemental powders and explore the relationship between microstructure, mechanical properties and oxidation resistance. In addition, we investigated possibility of reaction sintering $Ti_2(Al_{1-x}Si_x)C$ solid solution. The later is of the particular interest because previous studies showed that Ti_2SiC is thermodynamically unstable [9].

To improve mechanical properties of MAX phases and extend their potential applications to even higher temperatures, reinforcement with ceramic fibers and solid solution strengthening are considered to be potentially the most promising methods. Among all ceramic addition, Al_2O_3 has been proposed as potentially good candidate for reinforcing Ti_2AlC because of its high hardness, high modulus and good chemical stability, etc [76]. The second goal of this dissertation is to reinforce the Ti_2AlC with Nextel^{TM} 610 and 720 fibers through slip casting and investigate the effect of fiber on mechanical properties of Ti_2AlC.

On the other hand, solid solution strengthening was also considered to be one of the effective methods to further improve mechanical properties of the MAX phases [77, 78]. Since Ti_3AlC_2 and Ti_3SiC_2 are two of the most important potential structural materials, with unique distinct properties, it is speculated that $Ti_3(Al_{1-x}Si_x)C_2$ solid solution can combine the best attributes of both, i.e. good mechanical properties like Ti_3SiC_2, and maintain the excellent oxidation resistance similar to Ti_3AlC_2 at the same time. To test this hypothesis, we conducted systematic study of the physical and mechanical properties of $Ti_3(Al_{1-x}Si_x)C_2$ solid solution.

1.5 Research Objectives

The main goals of Ph.D. dissertation work are to study reaction synthesis of bulk high-purity MAX phase, namely Ti_2AlC, Ti_3AlC_2 and Ti_3SiC_2 and their solid solutions, from elemental powders by utilizing PECS and to explore the different strengthening mechanisms using solid solution strengthening and addition of ceramic reinforcement fibers.

The more specific objectives are:

- To generate in-depth understand of the reaction mechanism during reaction synthesis of Ti_2AlC in Ti-Al-TiC system using PECS, that has never been reaction sintered in the pure form using PECS;
- To explore possibility of using PECS method to reaction sinter $Ti_2(Al_{1-x}Si_x)C$ solid solutions, that has never been fabricated before using any method;
- To fabricate Ti_2AlC composites reinforced with Nextel^{TM} 610- and 720 alumina fibers through slip casting and PECS;
- To explore the relationship between the structure and microstructure of alumina fiber reinforced Ti_2AlC composites at room and elevated temperatures;
- To synthesize for the first time a series of high-purity $Ti_3(Al_{1-x}Si_x)C_2$ where x =0, 0.2, 0.4, 0.6, 0.8 and 1.0 from elemental powders using PECS;

- To study effects of solid solution effects in $Ti_3(Al_{1-x}Si_x)C_2$ on their mechanical properties at room and elevated temperatures;
- To evaluate oxidation resistance of $Ti_3(Al_{1-x}Si_x)C_2$ solid solutions at high temperatures.

2. PULSED ELECTRIC CURRENT SINTERING OF Ti_2AlC FROM Ti, Al AND TiC POWDERS

2.1 Synopsis

The mechanism of reaction synthesis of Ti_2AlC from Ti-Al-TiC powder mixture is studied in the temperature range of 700^oC and 1500^oC using Pulsed Electric Current Sintering (PECS) method. Results of the interrupted sintering tests indicate that reaction synthesis process occurs through the series of reactions: (i) between Ti and Al to form TiAl, Ti_3Al, $TiAl_3$ and $TiAl_2$ below 1000^oC; (ii) between TiC and different Ti_xAl_y to form Ti_2AlC above 1000^oC and Ti_3AlC_2 above 1100^oC. After optimizing composition of initial powder mixture and sintering conditions, the PECSed high-purity Ti_2AlC samples containing less than 5.2 vol% of impurities (mostly TiA_x) were reaction sintered from the powder mixture with Ti:Al:TiC=1:1.05:0.75 molar ratio at 1450^oC for 15 mins. Fabricated samples have the compressive strength of 1200±50 MPa that is the highest ever reported for Ti_2AlC, due to the very fine grain size.

2.2 Introduction

The MAX phases are a family of ternary carbides and nitrides with a common chemical formula $M_{n+1}AX_n$ (where M is an early transition element, A is a group A element, and X is either C or N element, n=1, 2 and 3) and inherent layered hexagonal structure (space group P63/mmc) in which $M_{n+1}X_n$ layers are interleaved with layers of A-group element [1]. As a result of their characteristic nanolaminated crystal structure and combination of covalent, metallic and ionic bonding within, the MAX phases have unique set of properties that place them at the middle ground between typical ceramics and metallic materials [2]. In other words, the MAX phases are not only elastically stiff, refractory and stable at high temperatures, but also thermal shock resistant, damage tolerant, and machinable [16]. In addition, they are good thermal and electrical conductors while some of them also show excellent oxidation and corrosion resistance [7]. Typical MAX phases show strain rate independent hysteretic nonlinear elastic stress-strain behavior even at room temperature [2, 26], while at higher temperature (above ~900 - 1000^{o}C) they can be deformed plastically in both tension and compression for more than 25% [16, 21].

Out of more than 70+ MAX phases known today, Ti_2AlC is one of the best candidates for high temperature structural applications [9] because of its excellent oxidation resistance. When Ti_2AlC is exposed to ambient air or steam in 1000-1400^{o}C temperature range, it forms protective and self-healing Al_2O_3 layer that does not spall off even after a large number of thermal cycles [42, 79, 80]. Ti_2AlC also has relatively low density of 4.1 g/cm^3 [1, 36], high Young's and shear moduli of 277 GPa and 119 GPa, respectively [40], and good thermal and electrical conductivity of 46×10^{-6} W/K and 2.8×10^{6} S/m, respectively [41]. In addition, Ti_2AlC possesses good mechanical properties with room temperature compressive and flexural strength of 540 MPa–763 MPa[36] and 430 MPa [36], respectively and fracture toughness of 6.5 MPa*m$^{1/2}$ [36, 81]. At higher temperatures, its creep resistance in 1000-1400^{o}C temperature range is quite good when compared with other creep-resistant materials, and it offers a great promise for future improvement [16, 82].

Since Ti_2AlC was first fabricated in late 1960s [4], several methods have been used to synthesize it in bulk, such as pressureless sintering (PS), hot isostatic pressing (HIP), hot pressing (HP), pulse electric current sintering (PECS)[1], and self-propagating high-temperature combustion synthesis with the pseudo–hot isostatic pressing process (SHS/PHIP) [67]. In general, two types of reaction routes have been used to reaction synthesize Ti_2AlC: (i) solid state reaction from Al_4C_3, Ti (or TiC) and C, or (ii) solid-liquid reaction from Ti, Al, C (or TiC) powder mixtures [46, 67]. The first bulk high-purity Ti_2AlC were sintered from the mixtures of Ti, Al_4C_3 and C powder using HP [83] and HIPing [36]. Later on, Gauthier-Brunet et al.[84] showed that pressures reaction synthesis of Ti_2AlC from Al_4C_3, Ti and C for an hour involves complex reaction mechanism with numerous intermediate phases forming between 570^{o}C-1400^{o}C, some of which remains present even in the final products (such as TiC and Ti_3AlC_2). Nevertheless, this processing route requires relatively high temperatures and extended reaction synthesis times, e.g. HIPing or HPing for 1300-1600^{o}C for 4-30 hrs, to process high purity samples [36, 83]. Therefore, most of the bulk Ti_2AlChas been synthesized in the recent years from Ti:Al:C powder mixtures.

Although first report on synthesis of Ti_2AlC from Ti, Al and C was published in the 60s and 70s [4, 85], they did not contain details on phase composition of the final products. However, judging from the properties of Ti_2AlC reported in those studies, the final products contained significant amount of secondary phases. Wang et al. [50]

---

[1] This method is also commonly referred to as spark plasma sintering (SPS), field assisted sintering (FAST), pulse discharge sintering (PDS), etc.

carried out the first systematic study on the reaction synthesis of Ti_2AlC from Ti, Al and C powder mixtures, and pointed out that a significant reduction in processing time can be achieved using this route as Al melts at 660°C, forming a liquid that promotes fast reaction and sintering. Based on X-ray diffraction (XRD) of final products, they concluded that pure Ti_2AlC can be reaction sintered from powder mixture with Ti:Al:C atomic ratios of 2:1:1 by HP at 1400°C and 30 MPa for only an hour. Alternately, the same reactants have been used in self-propagating high-temperature synthesis (SHS) to produce high purity Ti_2AlC in the order of seconds by taking advantage of highly exothermic reaction between Ti and molten Al [45, 86-88]. A major drawback of using pure Al powder as a reactant is that it evaporates during sintering, and therefore its amount in initial powder mixture has to be increased (usually for 5-20% above stoichiometric) to compensate for the Al that volatizes during synthesis or otherwise final product would have large amount of secondary phases such as TiC or $TiAl_x$ [46, 89]. The latter is particularly critical for Ti_2AlC as it is stable only in very narrow compositional range and thus the final stoichiometry has to be near perfect to avoid formation of secondary phases. On the other hand, as it was pointed out by Barsoum et al. [90], even XRD pure Ti_2AlC samples still can contain substantial amount (4-5vol%) of secondary phases, most likely $TiAl_x$ and TiC. Therefore, some of the previous studies reporting on processing of the pure Ti_2AlC from Ti, Al and C (or TiC) based solely on XRD results have to be considered with additional cautions.

When compared to other reaction sintering methods, PECS (commonly referred to as SPS) enables further reduction of reaction sintering and densification time and higher energy efficiency. Mei et al. [44] and Zhou et al. [73] reported that single phase Ti_2AlC can be reaction sintered by PECS at 1100^oC and 30 MPa for an hour, from the mixture of Ti, Al, and C powders with atomic ratio of 2:1.2:1. Sun et al. [91] also briefly reported on reaction synthesis of Ti_2AlC using PECS, and concluded that high purity samples can be obtained from the mixture of Ti, Al, and C powders with atomic ratio of 2:1.05:0.95 at 1250^oC for 20 mins. In all those studies, the phase composition of the final products were studied only by XRD. Another study also reported on synthesis of the high purity Ti_2AlC by PECS from Ti, Al, and C powder mixtures with atomic ratio of 2:1:1 at 1300^oC [74], although the XRD results in that study showed a strong peak for TiC. Interestingly, several studies also report on reaction synthesis of Ti_2AlC composites by PECS. Zhou et al. fabricated Ti_2AlC-Ti_3AlC_2 [92] from the mixture of Ti, Al, and TiC powders with atomic stoichiometric ratio of 1:1:1 at 1300^oC for 8 min, while Yang et al.[93] fabricated TiAl-Ti_2AlC from the mechanically allowed Ti-Al powders (Ti:Al atomic ratio is 2:1) containing 10vol.% of carbon nanotubes.

In this paper, we report on systematically study of the reaction between Ti, Al and TiC during PECS in the 700^oC– 1500^oC temperature range. As a result of that study, a high-purity Ti_2AlC_x is fabricated using the PECS at 1450^oC under a uniaxial pressure of 50 MPa. The mechanical properties and oxidation resistance of the high-purity Ti_2AlC are also studied to compare with other Ti_2AlC reported in literature.

2.3 Experimental Details

Commercial powders Ti (-325 mesh, 99.5% purity), Al (-325 mesh, 99.5% purity) and TiC (2–3µm average particle size, 99.5% purity) powders, all from Alfa

Aesar, MA, USA, were used as starting raw materials to synthesize Ti_2AlC. A series of powder mixtures with different ratios were used to study the reaction mechanisms and optimize parameters for fabrication of the high purity Ti_2AlC. All nominal chemical compositions of samples fabricated in this study are represented as $Ti_2Al_xC_y$ since they are all processed from the powder mixtures having Ti:Al:TiC=(2-y):x:y molar ratios.

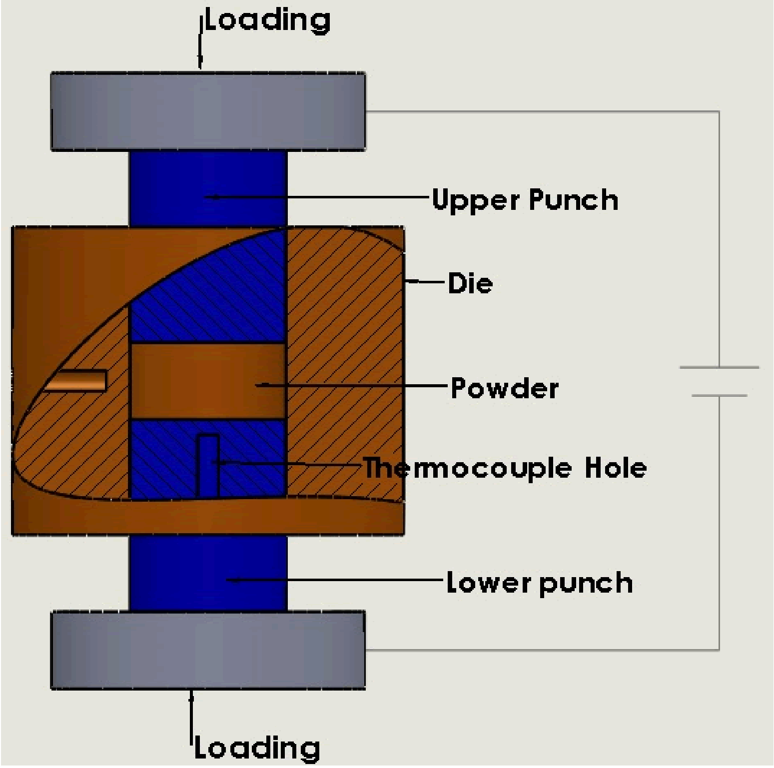

Figure 10 Schematic of pulsed electric current sintering method (PECS).

To prepare homogenous powder mixtures, Ti, Al and TiC powders were first weighed to achieve desired Ti:Al:C ratios and mixed together using ball-milling with zirconia beads in a glass jar at the speed of 300rpm for 24hrs. The powder mixtures were then packed between two cylindrical graphite punches into a cylindrical graphite die for PECS with an inner diameter of 20mm, Figure 10. Graphite foil was inserted between powder mixture and die set before compacting powder mixture into the die set. The die set with compacted powder mixture was placed in the PECS machine (SPS25-10, Thermal Technology LLC, USA) and pre-loaded at 5 MPa. The C-type control thermocouple was inserted in a hole located in the lower graphite punch to measure the temperature in the center of the die. The PECS system is composed of two water-cooled steel electrodes, which also served as loading plates from upper and lower rams. Before sintering, the PECS chamber was evacuated to $<10^{-3}$ Pa and then back-filled with an ultra-high purity argon to avoid oxidation during the sintering process. The powder mixtures were sintered in the 700–1500^{o}C temperature range using heating rate of 50^{o}C/min, the holding time at the target temperatures ranging from 15 to 60 mins, and the cooling rate of 200^{o}C/min. A constant load of 50 MPa was applied throughout the sintering process. Once the temperature of the die dropped below 100^{o}C, the die set was removed from PECS chamber to remove the sintered sample from it.

An additional two–step method was also used to process high purity Ti_2AlC samples using pressureless sintering and PECS. In this method, powders were weighed to achieve anatomic ratio of Ti:Al:C=2:1.05:0.95 and mixed by ball milling for 24 hrs. The powder mixture was then placed in alumina boats and reaction sintered in a high vacuum tube furnace (GSL1600X, MTI Corporation, USA) at a calibrated temperature of 1400°C under flowing ultra-high purity argon at 1 atm. The sintered compact was then drill milled and sieved to produce -170 mesh Ti_2AlC powders and densified using PECS for 15 minutes at 1300°C. The flow chart of fabrication of high-purity Ti_2AlC powder was represented in Figure 11 (a).

The surfaces of sintered samples were ground with SiC paper (down to 1000 grit) to remove graphite foil and any reaction layer, and subsequently polished using diamond suspensions (down to 1μm) to characterize their microstructure and composition. The phase identification of samples sintered at different temperatures was conducted using X-ray diffraction (Mode D8 Advance, Bruker AXS, Madison, WI) with a Cu_{α} radiation, at a rate of 0.015s/step and a step time of 0.2s. Microstructure of the fabricated samples was characterized using a field emission scanning electron microscope (FE-SEM; Quanta 600 FEG, FEI, Oregon, USA) equipped with energy dispersion spectrometer (EDS, Oxford Instruments, UK). The later was used for quantitative chemical analysis of different phases. After structural analysis of the polished surfaces by XRD, FE-SEM and EDS, they were etched for 10–15 seconds to expose the Ti_2AlC grains using a solution of $H_2O:HNO_3:HF=1:1:1$ and examined again using FE-SEM. The area fractions of impurity phases and grain size of the Ti_2AlC phase were quantified from FE-SEM images using ImageJ software.

The compressive strength was measured using universal testing machine (MTS 810, MTS, USA) in a displacement control mode at the displacement rate of 10^{-3} mm/s. A series of specimens with dimensions of $3.5 \times 3.5 \times 7$ mm^3 were cut from the centers of PECSed Ti_2AlC discs using Electrical Discharge Machining (EDM) (FX-10, Mitsubishi Co, Japan). The Vickers hardness was measured using a micro-hardness tester at the indentation loads ranging from 1N to 10N on the polished surface with a dwelling time of 15 s. The Vickers hardness was determined using as $H=2P/d^2$, where P is indentation load and d is average length of the indent's diagonal. For the oxidation resistance, a series of rectangular bars, $3.5 \times 3.5 \times 7$ mm^3, were cut using a diamond saw, and the final surfaces were grounded to 1000 grit. The initial weight and dimensions of samples were recorded before oxidation. In addition, fabricated samples where oxidized between at 1000–1300^{o}C for 10 hrs and 20 hrs in the ambient air, and the weight gain was recorded after the oxidation. The cross-section of oxidized sample were polished and examined using FE-SEM with EDS.

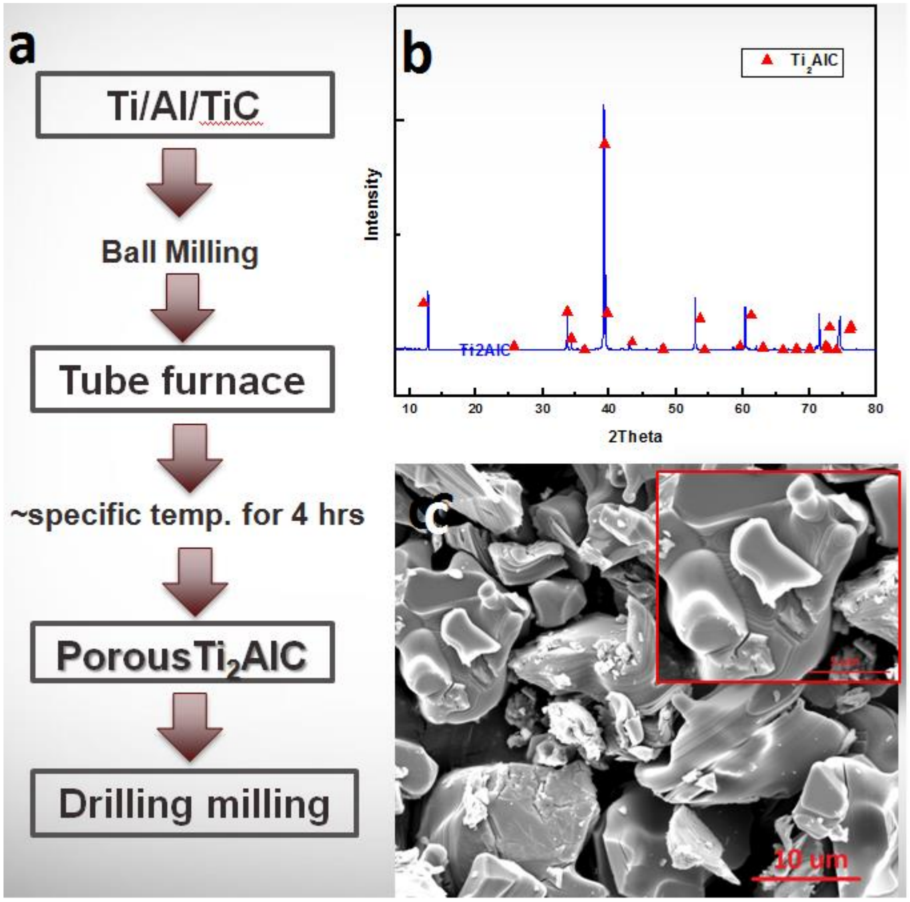

Figure 11 (a) A flow chart showing different steps in fabrication of high-purity Ti_2AlC powders; (b) XRD pattern of Ti_2AlC powder and (c) FE-SEM images of Ti_2AlC powders.

2.4 Results and Discussion

2.4.1 Synthesis of High-Purity Ti_2AlC Powder through Pressureless Sintering

XRD of the Ti_2AlC powders that were pressureless reaction sintered Ti:Al:TiC powder mixture with atomic ratio of1.05:1.05:0.95 (Figure 11b) indicate the high purity of the fabricated powders with less than 1% impurities. Typical layered structure of the individual Ti_2AlC particles can be observed in the FE-SEM images of the fabricated powder. In order to fabricate high-purity bulk Ti_2AlC samples from the reaction sintered powders, the reacted Ti_2AlC porous samples should be first drill-milled, then sieved and finally densified into the bulk samples by PECS or other densification methods. In order to process high-purity bulk Ti_2AlC samples more efficiently, the direct reaction sintering by PECS was utilized.

2.4.2 Reaction Mechanisms of Ti-Al-TiC Powders during PECS

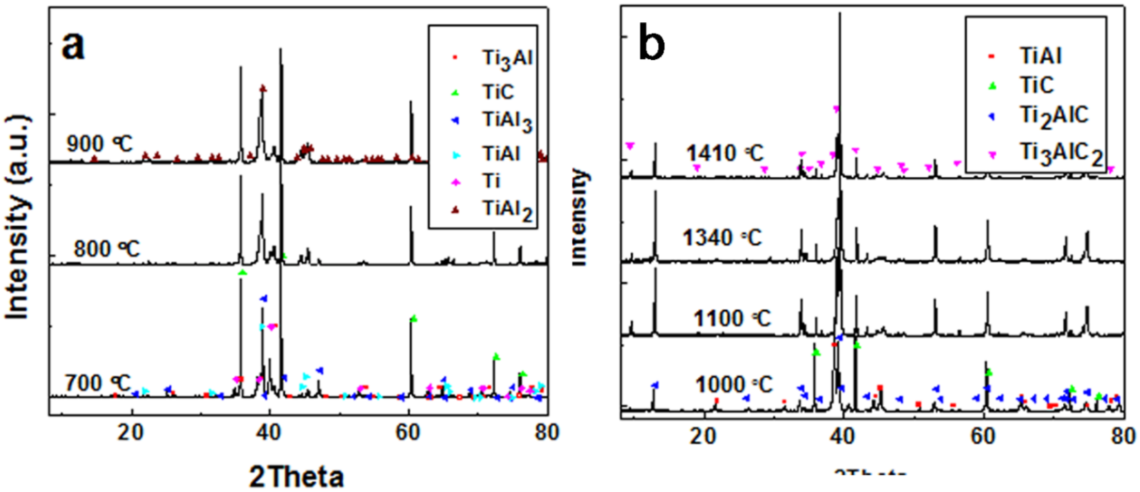

Figure 12 XRD patterns of Ti_2AlC samples sintered from powder mixture with Ti:Al:TiC =1.05:1.05:0.95 at a temperature range of 700-1410℃ for 30min by PECS from powder mixture of Ti_2_$Al_{1.05}$_$C_{0.95}$.

To understand the mechanisms of the solid-liquid reactions between Ti, Al and TiC during PECS, the powders mixture with Ti:Al:TiC molar rations of 1.05:1.05:0.95 (corresponding to the nominal composition of $Ti_2\_Al_{1.05}\_C_{0.95}$) were sintered in the 700°C–1410°C temperature range for 30 mins under a constant load of 50 MPa and cooled down rapidly at a rate of 200°C/min to ''freeze'' the intermediate phases. Figure 12 shows the XRD patterns of the PECSed samples with a nominal composition of $Ti_2\_Al_{1.05}\_C_{0.95}$ after reaction sintering at different temperatures, while Table 2 summarizes phases composition of all samples. In addition, the relative amount of phases were determined from the relative intensities of the peaks corresponding to different phases in the collected XRD patterns, and results are plotted in Figure 13 as a function of reaction synthesis temperature.

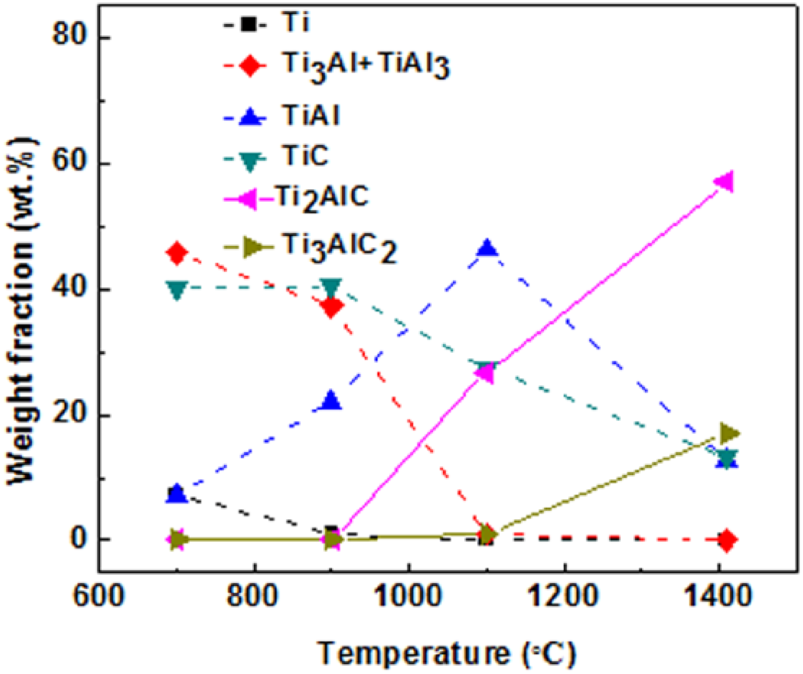

Figure 13 The relative amount of phases determined from XRD results.

Table 2 Phases determined through XRD patterns at different temperatures.

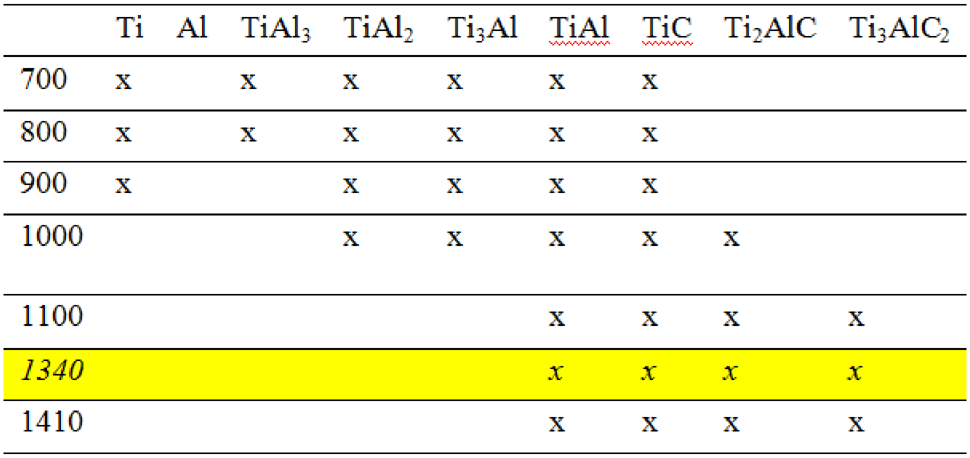

	Ti	Al	$TiAl_3$	$TiAl_2$	Ti_3Al	TiAl	TiC	Ti_2AlC	Ti_3AlC_2
700	x		x	x	x	x	x		
800	x		x	x	x	x	x		
900	x			x	x	x	x		
1000				x	x	x	x	x	
1100						x	x	x	x
1340						*x*	*x*	*x*	*x*
1410						x	x	x	x

Results in Figure 12, Figure 13 and Table 2 show that different intermetallic ($TiAl_3$, $TiAl_2$, TiAl and Ti_3Al) are present in the samples after sintering at 700°C and 800°C for 30 mins, besides TiC and Ti. Note that even after reaction sintering at only 700°C, no Al can be detected in the final product. After sintering at above 700°C, the amount of Ti, $TiAl_2$, $TiAl_3$ and Ti_3Al decreases gradually, while that of the TiAl phase increases. After sintering at 1000°C, only TiAl intermetallic and TiC can be detected from XRD results, together with the small amount of Ti_2AlC. Above reaction synthesis temperature of 1000°C, the amount of TiAl and TiC decrease gradually with the temperature, while that of Ti_2AlC increases. At the sintering temperature of 1100°C and above, the ancillary Ti_3AlC_2 phase can be detected in addition to TiC, TiAl and Ti_2AlC. It seems (Figure 13) that amount of Ti_3AlC_2 increases with increasing sintering temperature above 1100°C, together with that of Ti_2AlC. Further extension of the sintering time to 60 minutes at 1340°C (results not shown here) did not improve the purity of the samples, because Ti_3AlC_2,TiAl and TiC were present together with Ti_2AlC

in the reaction sintered sample. Figure 15 shows a back-scattered FE-SEM image of the sample reaction sintered at 1340°C by PECS for 30 minutes, together with the phase composition determine from the EDS quantitative analysis in selected spots. Dark gray and medium gray in Figure 15 were identified as TiC and TiAl, respectively. Light gray areas are either Ti_2AlC or Ti_3AlC_2. Note here that difference between Ti_2AlC from Ti_3AlC_2 cannot be observed in the back-scattered FE-SEM image as the contrast between two phases is insignificant. Results of FE-SEM with EDS analysis are in good agreement with XRD results (Table 2) as they show presence of Ti_2AlC, Ti_3AlC_2, TiC and TiAl in the reaction sintered sample.

To better understand the reaction mechanisms, sintering curves showing temperature and displacement of the puncher as a function of time during PECS were also examined. As it can see in the selected, but typical sintering curve in Figure 14, the sample continuously at the beginning of heating most likely as a result of the softening of Al and Ti powders. The shrinkage is particular accelerated in 600 – 683°C temperature range, i.e. around melting point of the Al. Above 683°C, it expands again as most of the molten Al is consumed by that temperature according to the reactions described below to form solid intermetallic phases. At around 850°C, the samples starts to shrink again as a result of accelerated densification.

Based on the XRD results summarized in Figure 12, Figure 13 and Table 2, possible reaction paths between Ti, Al and TiC powders during PECS are discussed in more detail below.

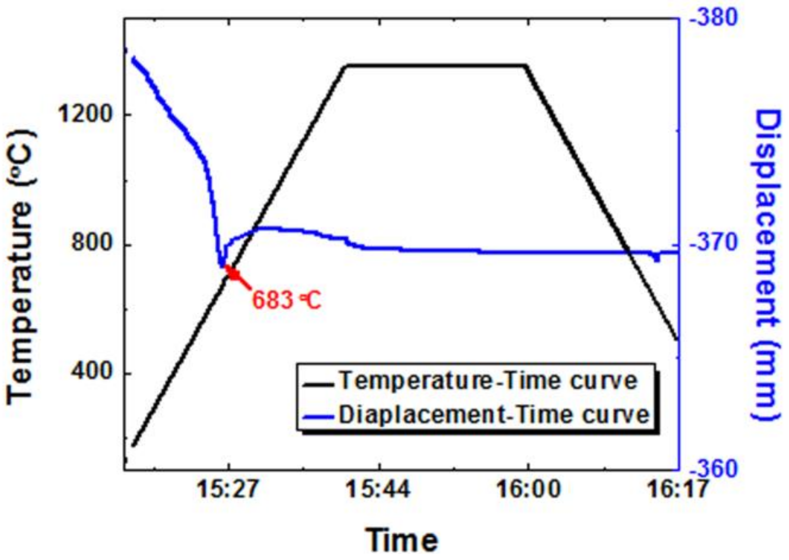

Figure 14 Typical shrinkage curve at 1410°C under applied load of 50 MPa showing temperature and displacement of the punches as a function of time.

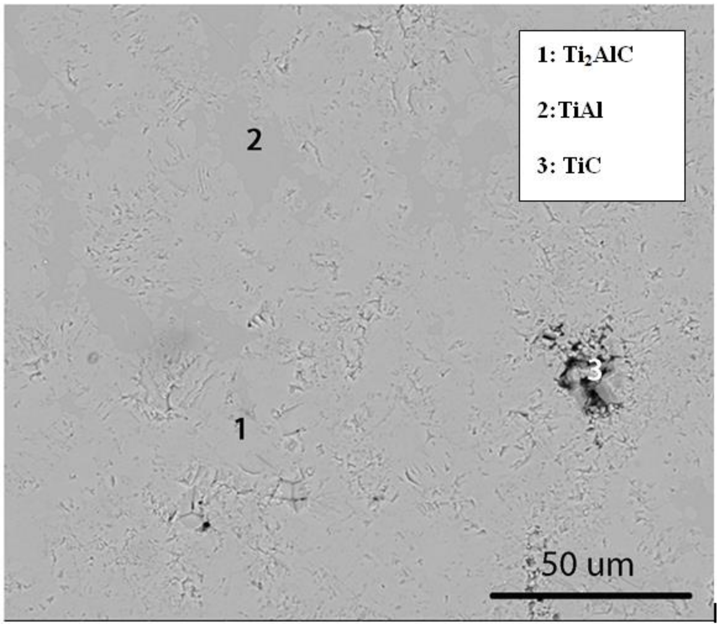

Figure 15 SEM image in the back-scattered mode of Ti_2AlC sample sintered at 1340°C by PECS, as labeled yellow in Table 2.

As Al melts at 660°C, it reacts completely with Ti below 700°C forming a series of Ti-Al intermetallic according to :

$$Al\ (s) = Al\ (l\ or\ g) \qquad 2.1$$

$$3Ti+Al=Ti_3Al\ (s) \qquad 2.2$$

$$Ti+Al=TiAl(s) \qquad 2.3$$

$$Ti+3Al=TiAl_3(s) \qquad 2.4$$

$$Ti+2Al=TiAl_2(s) \qquad 2.5$$

Note that all formed intermetallics are in the solid form as their solidus temperatures are well above 700°C [75]. Previously, Wang et al. [50] proposed that molten Al reacts with Ti to form only Ti_3Al and $TiAl_3$, based on the XRD of HPed elemental powders. However, results presented here suggest that both $TiAl_2$ and TiAl start to form as result of reaction between Ti and Al(l) in addition to Ti_3Al and $TiAl_3$, at temperature that is only 40°C higher than melting point of Al. More importantly, all molten Al is consumed by reactions 2.2-2.5 at that temperature. As the temperature increases to from 700°C to 1000°C, $TiAl_3$, $TiAl_2$, Ti_3Al and Ti probably reacted to form TiAl according to Equations (2.6-2.8),

$$Ti_3Al\ (s)+TiAl_3(s)=TiAl\ (s) \qquad 2.6$$

$$TiAl_3(s)+Ti\ (s)= TiAl\ (s) \qquad 2.7$$

$$TiAl_2(s)+Ti\ (s)= TiAl\ (s) \qquad 2.8$$

As a result, all $TiAl_3$ is consumed completely below 900°C in the reactions 2.6 - 2.7. Moreover, all Ti from the initial powder mixture reacts below 1000°C to form TiAl according to the reaction 2.8. All reactions in this temperature range (2.6-2.8) are solid state reactions, and they were also previously proposed as intermediate reactions during synthesis of Ti_3AlC_2 from the elemental powders [94]. Most importantly, results in Figure 12, Figure 13 and Table 2, suggest that Ti_2AlC starts to form between 900°C-1000°C most likely according to:

$$TiAl(s)+TiC(s)=Ti_2AlC(s) \quad 2.9$$

Most previous studies [43, 50, 88, 95] also suggested that Ti_2AlC phase initially forms through the reaction between TiAl and TiC according to reaction 2.9 at around 1000°C. With further heating to 1100°C, all $TiAl_2$ gets consumed in the reaction 2.8., leading to the increase of TiAl in the sintering product. At the same time, Ti_3AlC_2 ancillary phase starts to form between 1000°C and 1100°C most likely as a result of following reactions:

$$TiAl(s)+2TiC(s)=Ti_3AlC_2(s) \quad 2.10$$

$$Ti_2AlC(s)+TiC(s)=Ti_3AlC_2(s) \quad 2.11$$

Both reactions 2.10 and 2.11 were previously proposed as possible for formation of intermediate/ancillary Ti_3AlC_2 phases in different reaction sintering methods [43, 94]. It is worth noting here that Wang et. al. and Zou et al. presented that Ti_3AlC_2, at 1250°C, as ancillary formed according to Equations (2.10–2.11) [43, 94]. Once formed at 1100°C, the amount of ancillary Ti_3AlC_2 phase increases with the sintering temperature together with the amount of Ti_2AlC, suggesting that sold state reactions 2.9, 2.10, and 2.11 occurs simultaneously. Which one occurs, depends most likely on the local availably of the reactants, i.e. local chemical composition. Therefore, since PECS is very fast process, final produces after sintering even at 1410°C contains not only targeted

Ti_2AlC phase, but also TiAl, TiC and Ti_3AlC_2 ancillary phases. As it is mentioned, one sample was reaction sintered for 60 minutes at 1340°C with the hope that the amount of TiC and TiAl ancillary phases would decrease by completion of reaction 2.9-2.11, and/or that all Ti_3AlC_2 and TiC will be consumed thorough the following:

$$Ti_3AlC_2(s)+TiC(s)=2Ti_2AlC \qquad 2.12$$

as it is proposed by Zhu et al.[96] earlier. However, even after PECSing for 60 minutes at 1340°C all three ancillary phases, namely TiAl, TiC and Ti_3AlC_2 were observed in the final product. The later suggest that either diffusion and reaction kinetics are very sluggish, or that some other reactions, such the 2.11 one proposed by Gauthier-Brunet et al. [84] in the 1300-1400°C temperature range, can take place simultaneously with reactions 2.9. Finally, it is possible that ancillary phases are present as a result of deviation from Ti:Al:C=2:1:1 stoichiometry in the final product. Note here, that amount of Al and C were 20% above and 9% below stoichiometric, respectively, to account for the volatilization of molten Al and carbon reach atmosphere during PECS. Therefore a series of powder mixtures with different Ti:Al:TiC molar rations, all listed in Table 3 were reaction sintered in 1300–1400°C for 15-60 minutes. However, all fabricated samples contained substantial amount of ancillary phases as it could be seen in Table 3. Since samples reaction sintered from powder mixture with Ti:Al:TiC ratio of 1:1.05:0.75 (i.e. with the nominal composition of $Ti_2Al_{1.2}C_{0.85}$) had smaller amount of ancillary phases, they were selected to the further optimize reaction sintering parameters and reaction sinter high-purity Ti_2AlC samples by PECS.

Table 3 Phase composition of samples reaction sintered from the Ti:A:TiC powder mixtures with different molar ratios in 1300-1400°C temperature range.

Powder mixture	Nominal composition	Ancillary phases detected by XRD
Ti:Al:TiC=1.15:1.05:0.85	$Ti_2Al_{1.05}C_{0.85}$	10.5%Ti_3AlC_2, 4.5%TiAl, tiny TiC
Ti:Al:TiC=1.15:1.02:0.85	$Ti_2Al_{1.02}C_{0.85}$	14%Ti_3AlC_2, 7.7%TiAl, tiny TiC
Ti:Al:TiC=1.05:1.05:0.9	$Ti_2Al_{1.05}C_{0.9}$	Ti_3AlC_2, TiAl, TiC
Ti:Al:TiC=1.05:1.05:0.95	$Ti_2Al_{1.05}C_{0.95}$	20.3%Ti_3AlC_2, tiny TiAl, 21%TiC
Ti:Al:TiC=1.15:1.05:0.80	$Ti_2Al_{1.08}C_{0.8}$	5.6%Ti_3AlC_2, tiny TiAl, 2.6%TiC

2.4.3 Reaction Synthesis of the High-Purity Ti_2AlC by PECS

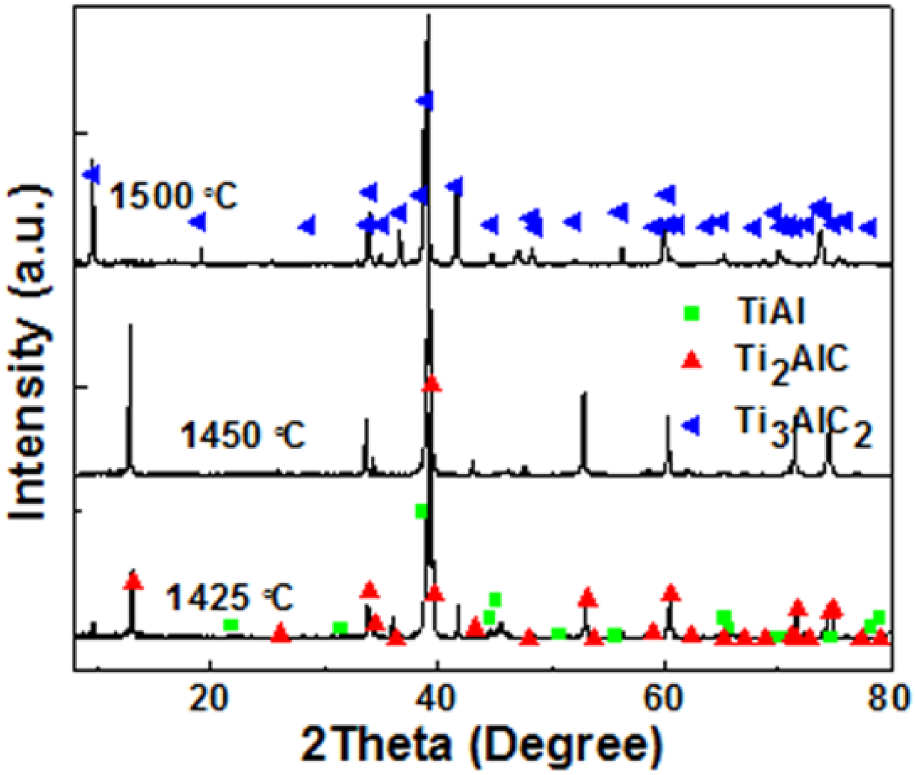

Figure 16 XRD patterns of the samples with nominal composition of $Ti_2Al_{1.2}C_{0.85}$ after reaction sintering at 1425°C, 1450°C and 1500°C.

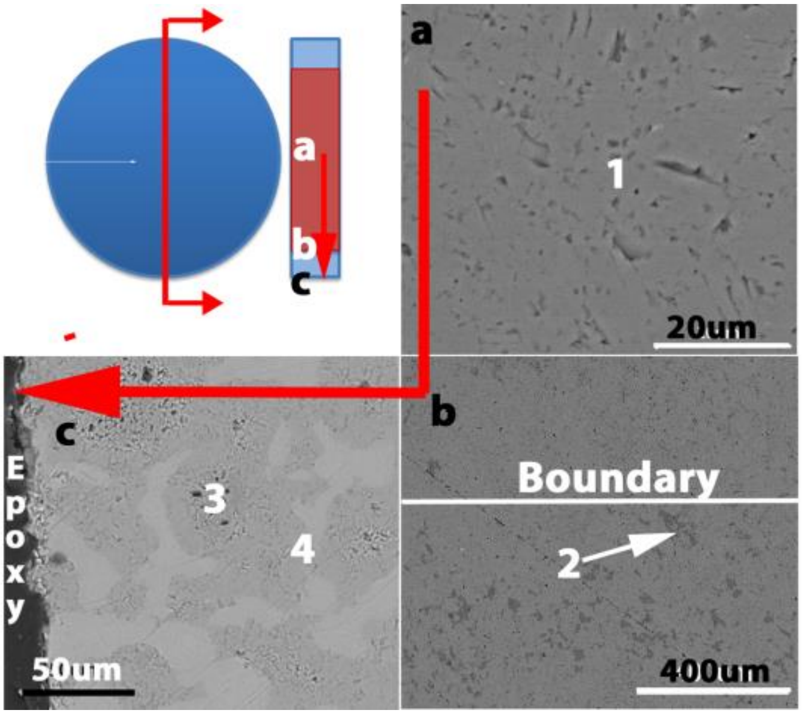

Figure 17 Schematic of the reaction sintered sample at 1450°C for 15 minutes from the powder mixture with the nominal composition of $Ti_2Al_{1.2}C_{0.85}$. a, b and c are FE-SEM images in the back-scattered electrons mode of area (a), (b) and (c) in the top right one, respectively. Possible phases were identified from the results of quantitative EDS analysis.

To further enhance kinetics of reaction 2.2-2.9 and decrease amount of the unreacted phases/impurities in the final products, the powder mixtures with Ti:Al:TiC ratio of 1:15:1.2:0.85 (nominal composition of $Ti_2Al_{1.2}C_{0.85}$) were sintered at higher temperatures, namely 1425°C, 1450°C and 1500°C. It is also expected that some intermetallic that forms according to reactions 2.2-2.7, will be in the liquid form in the 1425°C– 1500°C temperature range, most notably with compositions of TiAl, $TiAl_2$ and $TiAl_3$ as their congruent or incongruent melting points lie between 1393°C and 1491°C (for more details see Ti-Al phase diagram in [75]). The later was expected to further promote reactive sintering and homogenize the chemical and phase composition of the samples during short reaction sintering using PECS.

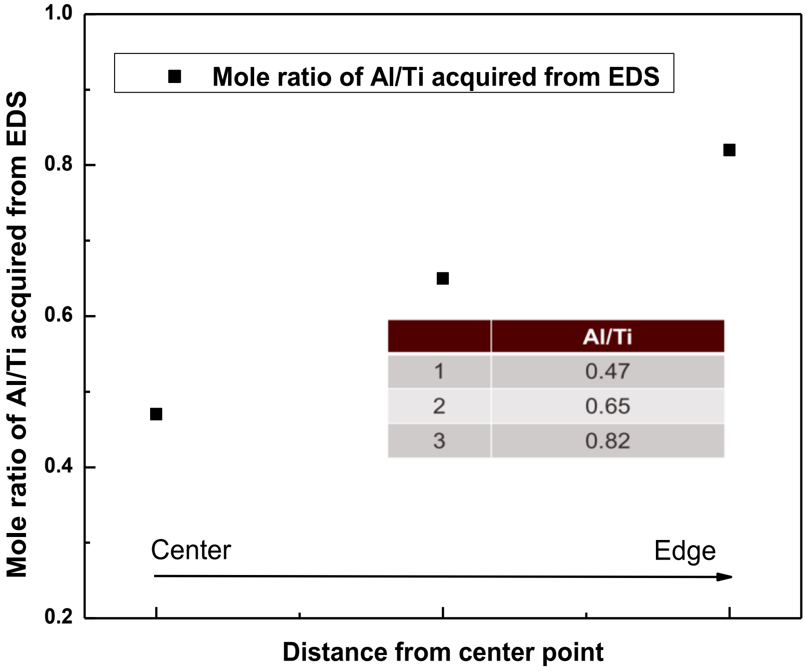

	Al/Ti
1	0.47
2	0.65
3	0.82

Figure 18 Al/Ti atomic ratios determined in regions a, b, and c from Figure 17 by quantitative EDS analysis of the 20 x 20 μm^2 areas.

Figure 16 shows the XRD patterns for the samples sintered at 1425°C,1450°C and 1500°C. After sintering at 1425°C, Ti_2AlC, Ti_3AlC_2 and TiAl coexist in the center of the fabricated samples. After sintering at 1450°C, only Ti_2AlC phase is noticeable in the XRD pattern collected from the center of the sintered discs. However, after sintering at 1500°C, only Ti_3AlC_2 can be detected in the center of the fabricated discs.

To further investigate phase compositions of the fabricated samples, FE-SEM images of the samples processed at 1450°C for 15 minutes in Figure 17 were collected from the center of the sample (area a in Figure 17), close to the perimeter of the discs (area c in Figure 17c) and in between those two areas (area b in Figure 17b). According to the results in Figure 17 there are two distinct regions with differed compositions and microstructures: (i) center of the discs contains only Ti_2AlC with a very small amount of secondary phases TiAl mostly located in the grain boundaries, (Figure 17a); and (ii) region close to the perimeter of the disk that contains substantial amount TiAl and TiC as a secondary phases, Figure 17c. Figure 17b shows diffused boundary between above mentioned regions a and c. In addition, average chemical composition of the areas a, b and c in Figure 17 were determined using analysis quantitative EDS analysis and results are shown in the Figure 18. Figure 18 shows that Al/Ti atomic ratio in the center is 0.47, i.e. very close to Ti:Al ratio of 2 that corresponds to Ti_2AlC. As we move towards perimeter, the Al/Ti ratio increases reaching the value of 0.82 at the perimeter of the disc.

With our best efforts, the TiAl impurity could not be removed completely even from the center of the sample sintered at 1450^oC for 15 minutes. Although XRD results in Figure 16 shows presence of only Ti_2AlC in the center of that sample, volume percent of the TiAl impurity (dark gray phase in Figure 17a) was estimated to be around 5.2vol.% from the FE-SEM images. In addition, grain sizes measurements from the FE-SEM images of the etched surfaces (not shown here) showed that the average grain length and thickness are about 6.9 µm and 4.5 µm, respectively.

Based on the results presented in Figure 16 and Figure 18, the following reaction mechanisms during PECS of the powder mixture with nominal composition of $Ti_2Al_{1.2}C_{0.85}$ can be proposed. At 1425^oC, all TiC and most of the Ti_xAl_y intermetallic were consumed via reactions 2.1-2.11, and final structure contains some unreacted TiAl together with Ti_2AlC and Ti_3AlC_2 that formed through reactions 2.9-2.11. Not here that the amount of ancillary phases in this case is much smaller than in the samples reaction sintered at 1350^oC, as the presence of the liquid TiAl phase promotes reaction 2.9 and 2.10 and/or leads to the better homogenization of the chemical composition within the sample.

With the increase of the temperature to 1450^oC, larger amount of Ti_xAl_y intermetallic are in the liquid state and they all get consumed in the center of the sample thorough the following reaction:

$$Ti_3AlC_2+TiAl=2Ti_2AlC \qquad 2.13$$

that was previously observed by as Yang et al. proposed [96]. However, large amount of unreacted TiAl and some amount of TiC phases can be observed at the perimeter of this sample. The later can be explained by the fact that some amount of the liquid Ti_xAl_y intermetallic squished from the center of the sample towards the perimeter, and further through the gap between the puncher and the die during pressure assisted reaction sintering. Note here, that small amounts of the intermetallic can be always observed around the puncher on the outside surface of the die set, after sintering in 1425-1500^oC temperature region. However, the best evidence supporting this scenario can be found in Figure 18 that clearly shows gradual increases in Al/Ti atomic ratio from the center towards perimeter of the sintered discs. In addition, PECS results in very non-uniform temperature destitution along diameter of the sample [93, 97] that can sometimes result in more than 200^oC difference between temperature in the center of the disc and at its perimeter. Since the temperature at the perimeter was most likely lower than the that of 1450^{o}C measured in the during sintering, Ti_2AlC, TiC and TiAl (s) coexist due to the incomplete reaction between TiAl and TiC.

XRD results in Figure 16 show after reaction sintering at 1500^{o}C the sample contains only Ti_3AlC_2 phase in the center. At that sintering temperature, the amount of the Ti_xAl_y intermetallic in the liquid form increases, while its viscosity further decreases when compared to the reaction sintering at 1450^{o}C. Therefore, larger amount of Ti_xAl_y intermetallics can be pushed from the center of the sample towards perimeter, and further into the gap between the punchers and die. As a result, smaller amount of TiAl remains in the center to form Ti_2AlC according to reaction 2.9. Thus, pure Ti_3AlC_2 forms through the reaction 2.10. Results of FE-SEM and EDS quantitative analysis (not shown here) showed that uniform phase composition in the center of the sample with Al/Ti corresponding 0.29 corresponding to the pure Ti_3AlC_2 phase. However, the ratio of Al/Ti increases to 0.73 at the perimeter, suggesting the presence of the larger amount of TiAl intermetallic in that region. In addition, some of Ti_2AlC that eventually formed in that sample at lower temperatures can also decomposed into Ti_3AlC_2 and liquid TiAl intermetallic at around 1500^{o}C according to the following reaction [98]:

$$Ti_2AlC=Ti_3AlC_2+TiAl\ (l) \qquad 2.14$$

To further confirm if decomposition of Ti_2AlC according to the reaction 2.14 takes place during at 1500^{o}C, high purity Ti_2AlC (with less than 3vol.% of impurities) process by in-house [35] was additionally PECSed at 1500^{o}C for extended period of time, i.e. 15mins, at the load of 50 MPa. Since large amount of Ti_3AlC_2 was found in XRD patterns and

FE-SEM images of the sintered samples, it can be concluded that Ti_2AlC does decompose to Ti_3AlC_2 during PECS according the 2.15 at 1500°C.

2.4.4 Mechanical Properties of PECSed Ti_2AlC

To ensure the phase purity of the samples, they were all cut from the center of PECSed Ti_2AlC discs for the mechanical testing. The density of PECSed Ti_2AlC sample was 4.06±0.5 g/cm^3 and the relative density of the samples were >98.0 %, determined according to ASTM C20-00 standard using alcohol immersion Archimedes' method described in more detail elsewhere [99].

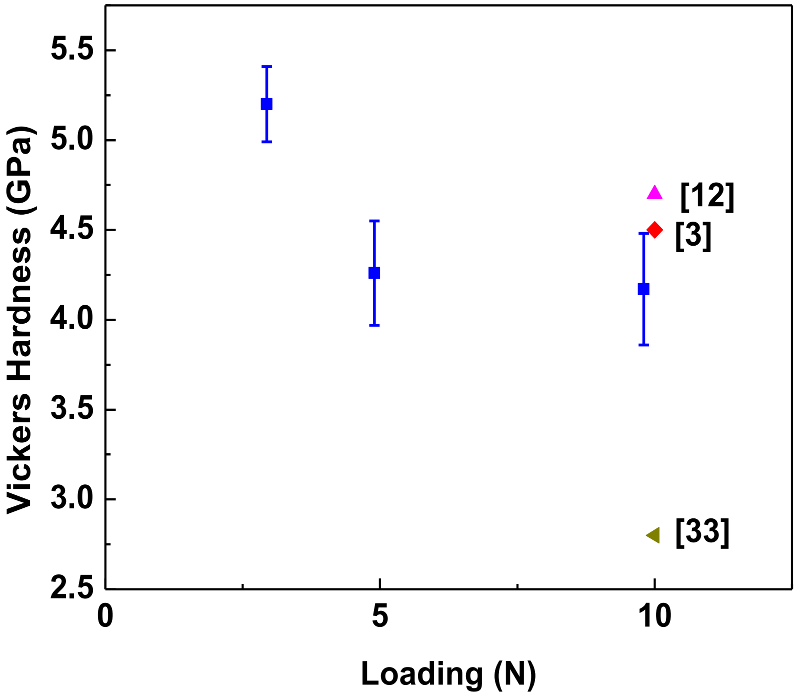

Figure 19 Vickers hardness as a function of indentation load.

Figure 19 shows the micro-Vickers hardness (H_v) of PECSed Ti_2AlC as a function of indentation load. Similar to other MAX phases [4, 11], Vickers hardness decreased with increasing indentation load and above a critical load, it reaches a constant value. At low indentation load, the high Vickers hardness (above 5 GPa) was due to the elastic recovery that led to a small indent after indentation. The H_v value of PECSed Ti_2AlC sample was 4.2±0.3 GPa at a load of 10 N. This value is in good agreement with the values reported previously to be 4.5 GPa[2] and 4.7 GPa [43].

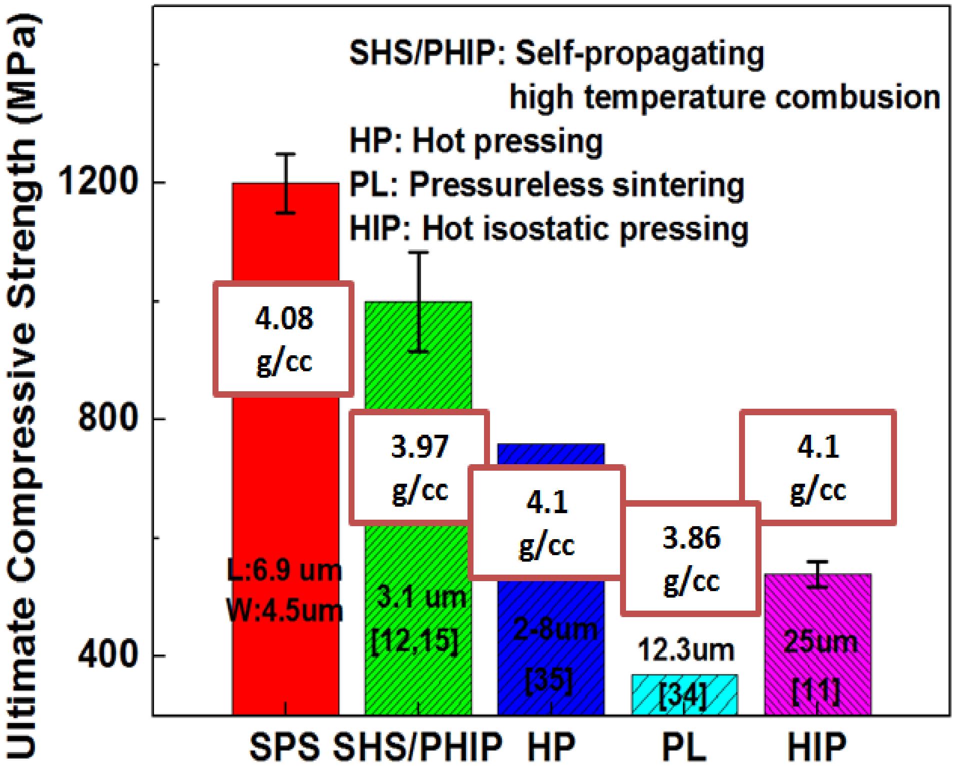

Figure 20 Comparison of room temperature compressive strength of Ti_2AlC samples sintered in various processing methods [35].

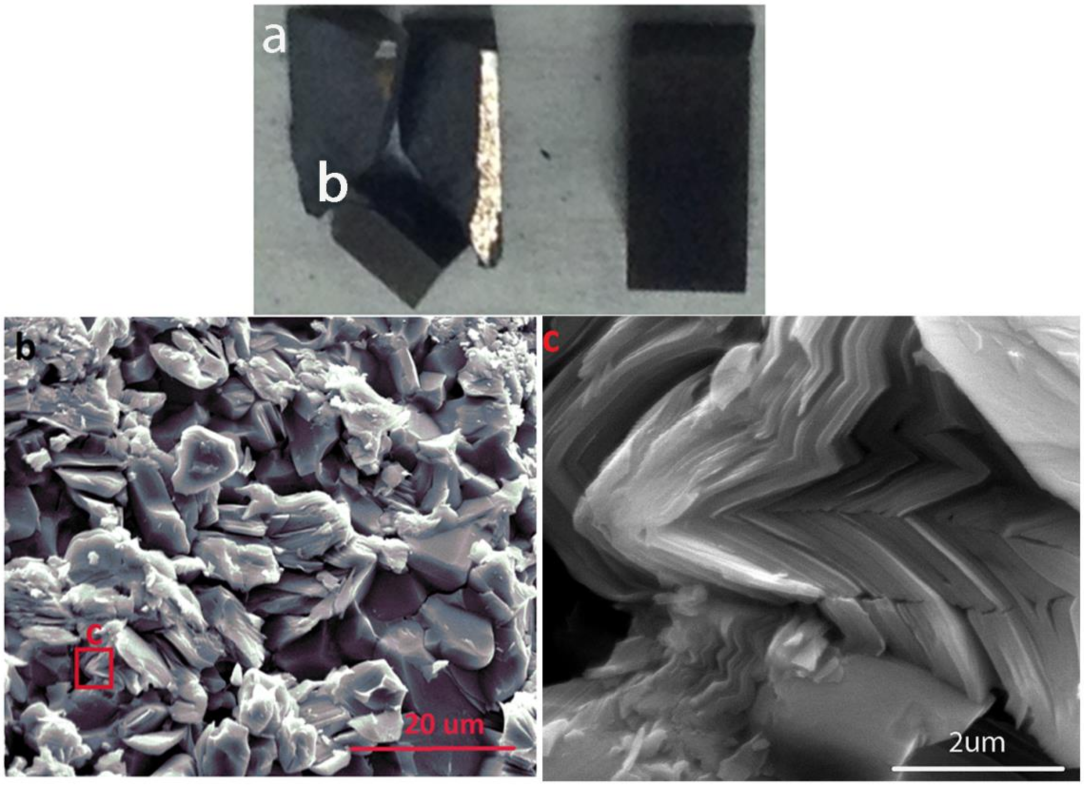

Figure 21 (a) Photo of the sample after testing in compression. (b) and (c) FE-SEM images of the fracture surfaces after testing in compression.

Figure 20 shows a comparison of the compressive strength of Ti_2AlC samples that were fabricated with different processing methods. The room temperature compressive strength of the samples fabricated in this study by PECSing powder mixture with the nominal composition of $Ti_2Al_{1.2}C_{0.85}$ at 1500^{o}C for 15 minutes is 1200±50 MPa. As it can be seen in Figure 20, this is the highest room temperature compressive strength ever reported for Ti_2AlC [36][50, 98, 100][43, 45][100]. None of the specimens fractured abruptly in the brittle manner by shattering in the large number of smaller pieces as it reached the maximum compressive strength, Figure 21. The high compressive strength of Ti_2AlC reported here can be mostly attributed to the following two factors: very small equal-axial grains, and higher relative density of the fabricated samples [35]. Figure 21 shows that regardless of the abrupt, brittle failure of the sample at the maximum compressive stress, the grains at the fracture are largely deformed by delamination and kinking, as it is typically observed in the MAX phases [11].

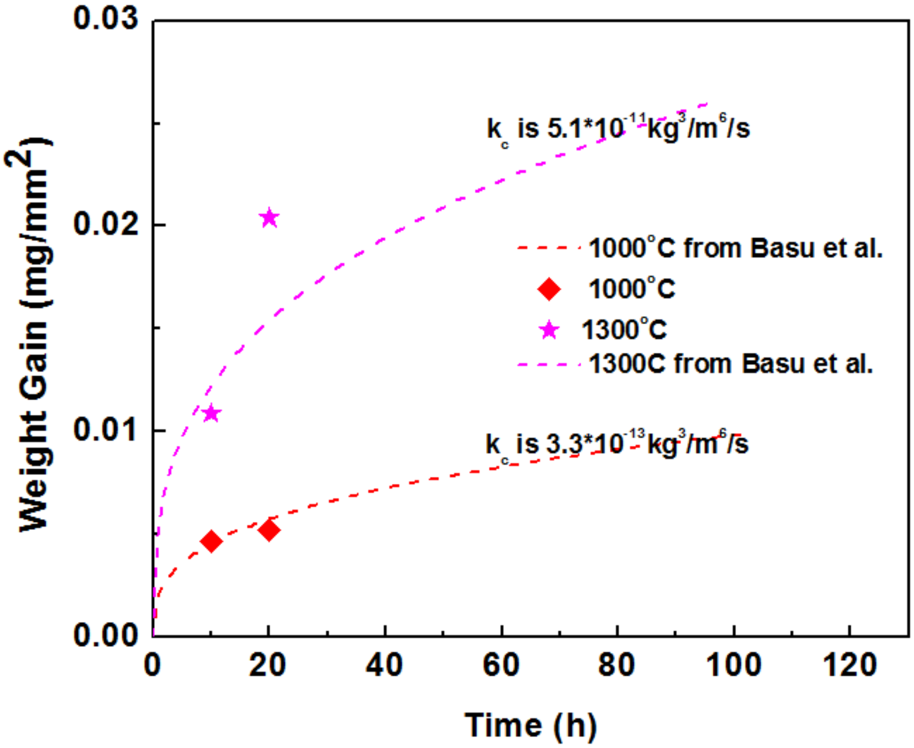

Figure 22 The weight gain per unit area as a function of time after oxidation testing of the high-purity Ti_2AlC samples at 1000°C and 1300°C in air. Dashed line represent results from previous studies [79].

2.4.5 Oxidation Resistance of PECSed Ti_2AlC at High Temperatures

Figure 22 shows the weight gain per unit area as a function of the oxidation time after oxidations at 1000°C and 1300°C in the ambient air. The results obtained using high-purity Ti_2AlC fabricated in this study are in good agreement with previously published data [79]. As Figure 23 shows, a typical stable and protective Al_2O_3 oxide layer forms during oxidation of high-purity Ti_2AlC samples fabricated in this study. As it was observed before in Ti_2AlC, oxide scale contains mixture of TiO_2 and Al_2O_3 mixture on the surface, and pure Al_2O_3 below it [79][65].

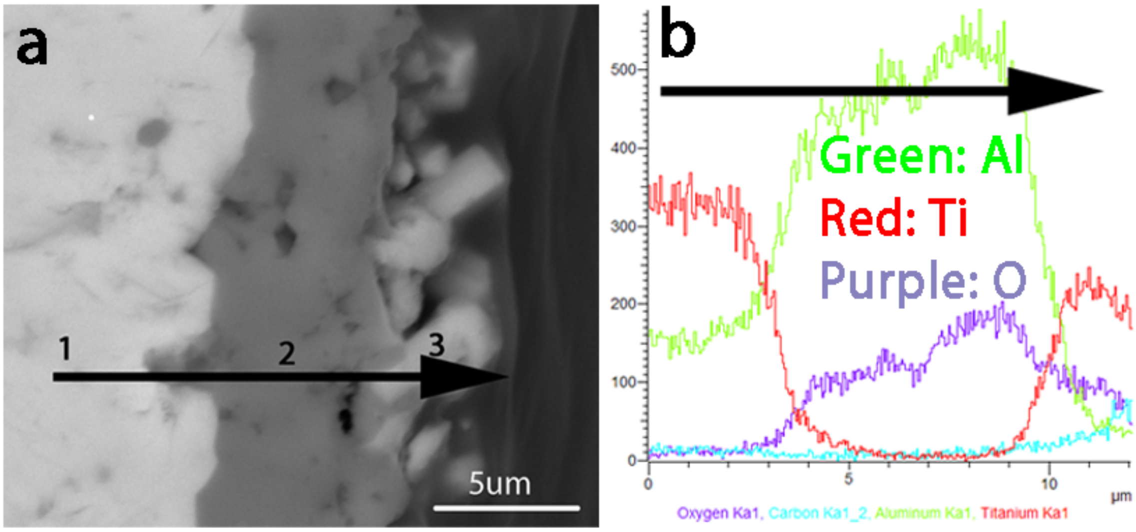

Figure 23 (a) FE-SEM image of the surface of Ti_2AlC after oxidation at $1300^{o}C$ for in ambient air for 10hrs; (b) EDS elemental analysis along the solid black line in (a).

2.5 Fabrication of $Ti_2(Al,Si)C$ Solid Solution

To further improve the mechanical properties of Ti_2AlC by solid solutions strengthening, a mixture of Ti:Al:Si:TiC powders with the 1.05:0.65:0.4:0.95 molar ratio was mixed and sintered to fabricate $Ti_2(Al_{1-x}Si_x)C$ solid solution at $1400^{o}C$ for 4hrs using pressure less sintering under ultra-high purity argon atmosphere. Not here that his fabrication of $Ti_2(Al_{1-x}Si_x)C$ is particularly challenging since Ti_2SiC end member is thermodynamically not stable and has never been synthesized in the past. XRD result of the reaction synthesized powders in Figure 24 shows only presence of Ti_3AlC_2 and

Ti_3SiC_2 in the fabricated samples. FE-SEM images together with EDS results in Figure 24 also suggests that structure consist of $Ti_3(Al_{0.97}Si_{0.03})C_2$ phases (points 1 and 3 in Figure 24) most likely mixture of $Ti_3SiC_2$and $TiSi_x$ (points 2 and 4)

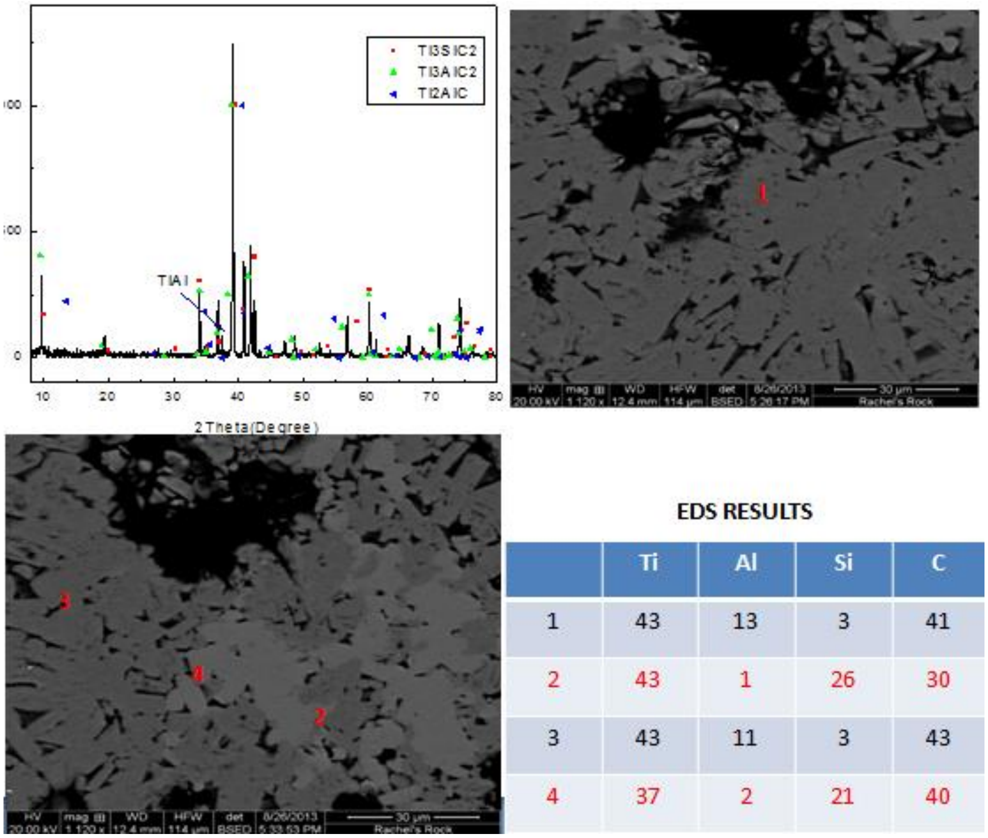

	Ti	Al	Si	C
1	43	13	3	41
2	43	1	26	30
3	43	11	3	43
4	37	2	21	40

Figure 24 (a) is XRD pattern of reaction sintered sample with nominal composition of $Ti_2Al_{0.65}Si_{0.4}C_{0.95}$, (b) and (c) are FE-SEM images in the back scattered modes, while (d) shows composition in spots 1-4 labeled in (b) and (c) detemind by EDS.

2.6 Conclusions

In this paper, a high-purity Ti_2AlC was synthesized using reactive PECS from a powder mixture with the nominal composition of $Ti_2Al_{1.2}C_{0.85}$ at 1450°C under a uniaxial pressure of 50 MPa for 15mins. The temperature window of fabricating Ti_2AlC

through the reactive PECS was found to be very narrow, i.e. 1450±25^{o}C. Below 1450^{o}C, Ti_3AlC_2 and Ti_2AlC initially formed due to the reaction between TiAl and TiC. At 1450^{o}C, a high-purity Ti_2AlC was fabricated due to the reaction between Ti_3AlC_2 and TiAl to form Ti_2AlC. At 1500^{o}C, Ti_3AlC_2 is formed as liquid TiAl intermetallic are pushed out from the die during reaction sintering and are formed due to the decomposition of Ti_2AlC. The mechanical properties and microstructure of the high-purity Ti_2AlC were characterized and compared with Ti_2AlC processed by other methods. Vickers hardness and compressive strength of the high-purity Ti_2AlC were 4.2 GPa and 1200 MPa, respectively. The compressive strength of high-purity Ti_2AlC has a record-high value when comparison the previously published data. The oxidation kinetics of the high-purity Ti_2AlC agrees well with the literature data due to formation of a continuous layer of alumina at the surface. Compared with other sintering methods, the reactive PECS is a rapid and energy efficient process, leading to a high-impurity Ti_2AlC with superior mechanical properties. The disadvantage of the reactive PECS is in compositional and microstructural variations that are usually observed in the samples. Therefore, it is difficult to scale up the reactive PECS process, to fabricate large Ti_2AlC samples with the high purity, uniform composition and microstructure.

3. MECHANICAL CHARACTERIZATION OF NEXTEL^{TM}610 AND NEXTEL^{TM}720 FIBERS REINFORCED Ti_2AlC COMPOSITES*[2]

3.1 Synopsis

Herein we report on the fabrication and mechanical properties of Ti_2AlC reinforced with of 20 vol% alumina fibers (Nextel^{TM} 610 or Nextel^{TM} 720). Ti_2AlC-Nextel^{TM} 720 and Ti_2AlC-Nextel^{TM} 610 composites were prepared via colloidal processing, followed by slip casting and pulse electric current sintering (PECS). Fabricated composites have higher elastic moduli and Vickers hardness when compared to the pure Ti_2AlC matrix for more than ~4.5% and ~35.8%, respectively. They also showed improvements in compressive strength and fracture toughness for Ti_2AlC-Nextel^{TM} 720 composites up to ~26.5% and ~21.1%, respectively. It was found that Ti_2AlC-Nextel^{TM} 720 composites have better mechanical properties at room temperature than Ti_2AlC-Nextel^{TM} 610 ones. Microstructural analysis after mechanical testing indicates that crack bridging, crack deflection and fiber pullout contribute to the observed toughening in the fabricated composites. Results of the high-temperature mechanical testing in compression suggests that above ~1000^{o}C, reinforcement with alumina fibers becomes less effective method for improving mechanical properties of Ti_2AlC.

---

*[2] Copyright Notice: "Dynamic Behavior of Materials, Static and Dynamic Thermo-Mechanical Behavior of Ti_2AlC MAX Phase and Fiber Reinforced Ti_2AlC Composites, Volume 1, 2015, pp 9-14, Parrikar PN, Gao H, Radovic M, Shukla A, (Original copyright notice as given in the publication in which the material was originally published), With permission of Springer"

3.2 Introduction

A novel family of ternary carbides and/or nitrides with nano-layered structure, commonly referred to as MAX phases nowadays, was first discovered in 1960s by Nowonty and his coworkers[4]. More than 70 members of this family share the same crystal structure and chemical formula of $M_{n+1}AX_n$, where M is an early transition metal, A is an A-group element and X is C and/or N [1]. It has been well established by now that the MAX phases have a unique set of properties, some of which are usually found in typical metals, rather than in other typical carbide or nitride ceramics [2, 16]. Therefore, they are sometimes referred to as metallic ceramic [101]. Like typical ceramic, the MAX phases have high elastic moduli, low coefficient of thermal expansion, and good thermodynamic stability at high temperatures [1, 9]. However, they show excellent electrical and thermal conductivity and can be easily machined [9, 16]. Some of the MAX phases were found to have good oxidation, creep and fatigue resistance [9, 42, 69, 102]. Their response under compressive and tensile stresses was also found to be quite distinct when compared to the typical metals or ceramics, as they show non-linear, hysteretic behavior even at room temperatures [15, 26], while above brittle-to-plastic transition (BPT) temperatures, then can be deformed to up to 25% even in tension [2, 20]. Unique properties of the MAX phases can be traced back to distinct combination of covalent, ionic and metallic bonds in their nano-layer structure, in which $M_{n+1}X_n$ layers are interleaved with hexagonal layers of pure A-group element layer [9]. In addition, their unusual mechanical behavior attributed to the fact that only basal plane dislocations can easily move, multiply, and arrange themselves either in dislocation walls or pile-ups during loading [2].

Among all MAX phases, Ti_2AlC is considered as the most promising candidate for structural application at high temperatures [7, 103]. Ti_2AlC has been regarded for light-weight MAX phase (density of 4.1 g/cm^3) [1], with excellent oxidation resistance [42], low thermal expansion coefficient [41], good resistance to creep [42], and self-healing capability at high temperatures [80]. The compressive strength of Ti_2AlC at room temperature was reported to vary between 390- 1200 MPa, depending on the grain size and amount of impurities [35, 36, 103]. With the fracture toughness was in a range of 6-9 MPa*m$^{1/2}$[36], Ti_2AlC is one of the toughest monolithic carbide ceramic. It was also reported that Ti_2AlC undergoes the brittle-to-ductile transition (BPT) at temperature between 900^{o}C and 1000^{o}C, above which, it can be deformed plastically for more than 25% [36, 43]. All these properties make Ti_2AlC a good candidate material for turbine blades, heating element, heat exchanger, and die tools, and other high-temperature applications [67].

To further improve the mechanical properties and extend the potential applications of Ti_2AlC, its reinforcement with other ceramics has been proposed in the past. And Alumina (Al_2O_3) is considered to be a good candidate for reinforcing phase [76, 104], as it is in thermodynamic equilibrium with Ti_2AlC and has almost identical coefficient of thermal expansion as Ti_2AlC. In addition, Al_2O_3 has high hardness and modulus, good strength and chemical stability. Zhang et al. synthesized Ti_2AlC-TiC-Al_2O_3 composites through a high energy mechanical milling and powder co-sintering, and demonstrated their high hardness (11 GPa) when compared to the pure Ti_2AlC [105]. However, compressive strengths of only 380–440 MPa were reported for those composites. Later on, Hashimoto et al. [100] also showed that addition of 5vol.% Al_2O_3 particle to Ti_2AlC resulted in improvement on Vickers hardness, but in the same time reduced fracture toughness and flexural strength.

Reinforcement with ceramic fibers, such as Al_2O_3 and SiC, seems to be more promising approach for improving mechanical properties of Ti_2AlC [76, 106-108]. Spencer et al. [106] showed that although SiC fibers could be an excellent choice for reinforcing Ti_2AlC, their application is very limited because of the severe chemical reaction between SiC fibers and Ti_2AlC during processing at 1300^{o}C as Al diffuses out of Ti_2AlC and reacts with SiC at the fiber/matrix interface. Later on, Gao et al. reinforced another MAX phase, namely Ti_3AlC_2 with SiC fibers and showed formation of the reaction phases at the fiber-matrix interface that can be partially controlled by addition of Ti foil between fibers and matrix [107, 108]. However, all those attempts resulted in very moderate improvements, if not decrease in the room temperature strengths of the composites when compared to the pure Ti_3AlC_2.

As a solution to the problem, Spencer et al. [76] showed in another study that Ti_2AlC can be reinforced by using less expensive and more accessible Al_2O_3 fibers as those fibers do not react with the matrix during densification of dry-mixed Al_2O_3 fiber and Ti_2AlC powder mixtures by hot-pressing (HPing) or hot-isostatic pressing (HIPing). However, a dry-mixing of fibers with MAX phase powder in this study resulted into the significant fiber entanglement and agglomeration when fiber content exceeded 5vol.%.

In order to disperse individual alumina fibers more uniformly within Ti_2AlC, colloidal processing was proposed to fabricate Ti_2AlC-alumina fiber composites[109]. Compared to the conventional dry mixing method, colloidal processing allows not only better and more uniform distribution of the fibers, but also easy fabrication of complex shapes and large size products and better tailoring the microstructure[110]. Jeon et al. [109] also showed alumina fiber pull out at the fracture surfaces of Ti_2AlC-alumina fiber composites fabricated by colloidal processing. The later suggests that alumina fiber could be used to enhance fracture toughness and strength of Ti_2AlC.

In this paper, we report on the room and high temperature mechanical properties of Ti_2AlC-alumian fiber composts reinforced with 20vol.% Nextel^{TM} 610 and Nextel^{TM} 720 fibers, that were fabricated using colloidal processing, followed by pulsed electric current sintering (PECS)[3]. Nextel^{TM} 610 fibers consisting of 99wt.% Al_2O_3 have high room-temperature tensile strength of >3.1 GPa and high elastic modulus of 380 GPa [111]. However, their tensile strength decreases monotonically with temperature, reaching only ~37% of the room temperature strength at 1200^{o}C [111]. Nextel^{TM}720 fibers show less significant decrease of tensile strength with temperature, i.e. its value of 2.1 GPa remains almost constant up to 1100^{o}C, and decreases gradually above that temperature for ~35% up to 1300^{o}C. However, Nextel^{TM} 720 fibers contains 15 wt.% of SiO_2 besides Al_2O_3 [111]. To evaluate the benefits of using both alumina fiber for reinforcement of Ti_2AlC composites, the elastic moduli, Vickers hardness, strength

---

[3] This method is commonly but inadequately referred to as spark plasma sintering (SPS)

under quasi-static loading and dynamic loading, and fracture toughness of Nextel^{TM} 720 fibers and 610 fibers reinforced Ti_2AlC composites were studied in this paper

3.3 Experiment Details

A high-purity Ti_2AlC powder was reaction sintered from the mixture of Ti (44µm, 99.5% purity, Alfa Aesar, MA, USA), Al (44µm, 99.5% purity, Alfa Aesar, MA, USA) and TiC (2-3µm, 99.5% purity, Alfa Aesar, MA, USA) powders with the following molar ratio Ti :Al: TiC=1.05:1.2:0.95. Reaction synthesis was carried out in the tube furnace at 1400^{o}C for 4hrs, under the constant flow of the ultra-high purity argon. Highly porous green bodies obtained in reaction synthesis were drill-milled into the powder that was subsequently sieved to obtained powder with particle sizes below 90 µm. X-ray diffraction (XRD) of the fabricated powder showed high purity of the powders with less than 3vol.% of impurities (mostly $TiAl_x$ and Al_2O_3). Nextel^{TM} 720 and Nextel^{TM} 610 with a diameter of 10-12 µm and an average length of 1/3' were supplied by 3M corporation (Maplewood, Minnesota, USA). Before using alumina fibers for slip casting, they were heated at 400^{o}C for 5mins to burn out the polymer coating on fiber surfaces (sizing) and then grinded to achieve fibers with an average length of 150 µm using mortar and pesto.

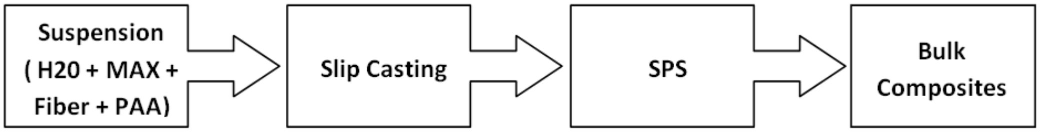

Figure 25 Flow chart of processing steps in fabrication of alumina fiber reinforced Ti_2AlC composites

The schematic of processing steps that we used to fabricate Ti_2AlC-Nextel^{TM} 610 and Ti_2AlC-Nextel^{TM} 720 composites is shown in Figure 25. First, the aqueous solution with PH=4 was prepared by adding 5 wt.% Poly-Acrylic-Acid and sodium hydroxide into the deionized water [109]. Then, chopped alumina fibers and Ti_2AlC powder were dispersed in to the aqueous solution to reach Al_2O_3:Ti_2AlC volume ratio of 20:80. After stirring 20 mins to get good suspension, the suspension was slip-casted into dry plaster molds (40 mm in diameter) and left to consolidate to the green bodies for minimum 24 hours. For densification, the green body was placed into a 40mm graphite die for PECS. The typical sintering curve at a constant load of 100 MPa is shown in Figure 26. It shows that the green sample expanded linearly with sintering temperature up to 900^{o}C. After reaching 900^{o}C, the sample starts to shrink significantly with sintering time as a result of densification, until it reaches a constant value when the densification is completed.

The density of all samples were measured according to ASTM C20-00 using alcohol immersion method and procedure that is described in more details elsewhere [26, 99]. The density of composites were calculated as: $\rho = \frac{m-m\prime}{v}$, where, ρ is density, m is the dry weight. m' is the immersed weight in alcohol, and v is the volume of the sample. Furthermore, the relative density of the processed samples with 20wt.% fibers were deeming from those measurements by adopting theoretical densities of 4.11 g/cm^3, 4.06 g/cm^3, and 3.97 g/cm^3 for Ti_2AlC, Nextel^{TM} 610 and Ti_2AlC-Nextel^{TM} 720, respectively [9, 111].

All processed compositions were characterized by X-ray diffraction (XRD, Mode D8Advance, Bruker AXS, Madison, WI) using Cu_{α} radiation, at a rate of 0.015 s/step and a step time of 0.02s in the 2θ range of 8 - 80°. Microstructure of sintered samples and fracture surfaces after mechanical testing were characterized using a field emission scanning electron microscope (FE-SEM; Quanta 600 FEG, FEI, Oregon, USA) equipped with energy dispersion spectroscopy (EDS; Oxford Instruments, UK). EDS was used to analyze the chemical composition of different phases in the processed composites. To characterize the microstructure, the samples were grinded by SiC sand papers down to 1000 grit and then polished using diamond suspensions down to 1μm. The fracture surfaces were coated with 4nm Pt layer before scanning electron microscopy.

Resonant ultrasound spectroscopy (RUS, Magnaflux Quasar Systems, NM) was used to quantify the elastic moduli through measuring resonance spectra using procedure described in more details elsewhere [40, 112]. The RUS specimen was electron-discharged-machine (EDM) cutted into 3.5x3.5x7 mm^3 samples with parallel surfaces. The sample was lightly held between drive transducer and receiving transducer. The drive transducer generated an elastic wave with constant amplitude and varying frequency (0 to 400 kHz), meanwhile, a resonant spectrum was recorded by receiving transducer. Quasar RuSpec (Magnaflux Quasar Systems, NM) software was used to determine the elastic moduli using from the frequencies of detected resonant peaks.

Vickers hardness measurements were carried out on the flat surfaces using Micro-hardness Tester LM 300AT (LECO, MI) at a load of 1N, 2N, 5N, and 10N with a dwelling time of 15s. The sample surfaces were grinded and polished before performing indentation test. The Vickers hardness was calculated as $H=2P/d^2$, where, P is indentation load and d is the average diagonal of the indent. At least twenty measurements were carried out for each samples at different locations.

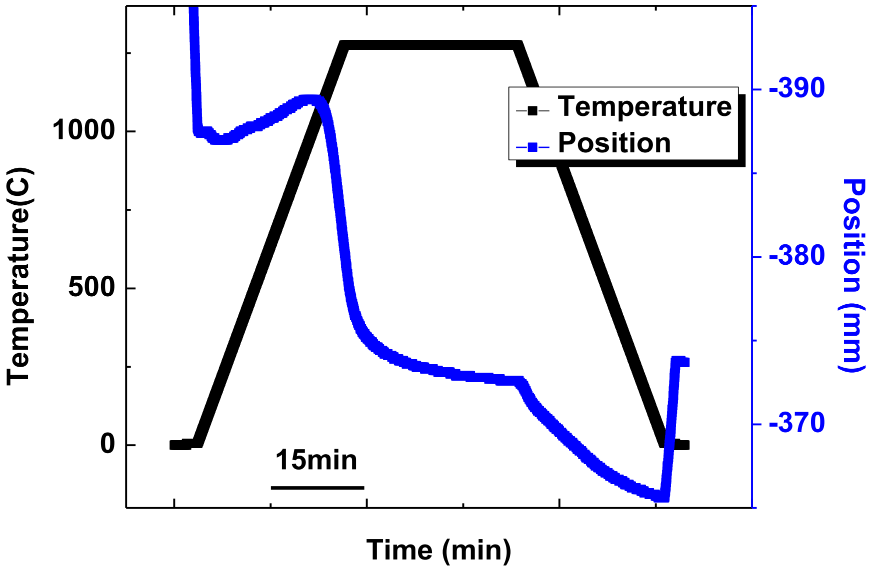

Figure 26 Typical sintering curve of PECSed composites showing change of temperature and position of punches with the sintering time.

The specimens for mechanical characterization were EDM-machined to cylinders with a diameter of 5mm and a height of 8mm. Then flat surfaces were gently ground using 1000 grit grand papers to shape edge and obtain parallelism with less than 1% error. Quasi-static compression test at room temperature and elevated temperatures was performed using 810 Materials Testing System (MTS, MN) under a displacement control mode with a strain rate of 10^{-4} mm/s. Two tungsten carbide spacers were inserted on both sides of specimen and high temperature extensometer (632.59, MTS, USA) was attached to the spacers to record the strain. To minimize the friction between sample surfaces and spacers, silicone and boron nitride lubricants were used at room and high temperatures, respectively.

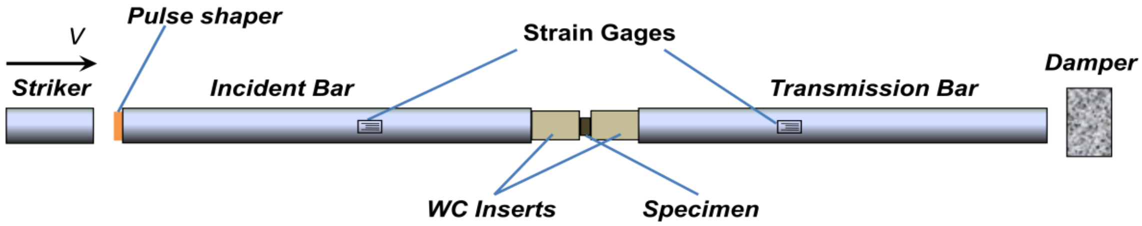

Figure 27 The set-up of Split Hopkinson Pressure Bar apparatus

Dynamic behavior of Ti_2AlC and its composites at room temperature was also studied using a Split Hopkinson Pressure Bar apparatus (SHPB). The setup of SHPB shown in Figure 27 [113] consists of striker bar, incident bar and transmission bar. To reduce the stress concentration and prevent indentation of specimen into bars, two tungsten carbide inserts were placed to modify the SPHB setup for ceramic testing [114]. Ti_2AlC sample was sandwiched-placed between two tungsten-carbide (WC) inserts. And the impedance of the WC inserts was matched to the bars, which does not disturb the stress wave profile. Molybdenum disulfide was also used to lubricate between the sample -inserts interface. As the striker bar hits the incident bar at a frequency of v, the incident pulse propagated along the incident bar and reached upon sample. One part of incident pulse reflected back into the incident reflected pulse. The rest was transmitted through the sample into the transmission bar, referred as transmitted wave. In this study, two strain gages were used to record the strain signals. With one-dimensional wave theory, the true stress and strain can be determined from the reflected and transmitted strain pulses, respectively, as

$$\sigma_s = E_b \frac{A_b}{A_s} \varepsilon_t(t) \qquad 3.1$$

$$\varepsilon_s = \frac{-2c_b}{L_s} \int_0^t \varepsilon_r(t)dt \qquad 3.2$$

where, σ_s and ε_s are stress and strain in the specimen, ε_r and ε_t are the time resolved strain values of reflected and transmitted pulses, c_b is the longitudinal bar wave speed, E_b is the Young's modulus of the bar material, A_b is the cross-sectional area of the bar, and A_s is the cross-sectional area of the specimen and L_s is the thickness of the specimen. The samples used in this study were a cylinder with a diameter of 3.5mm and a height of 6mm. All tests were performed at an average strain rate of $400s^{-1}$.

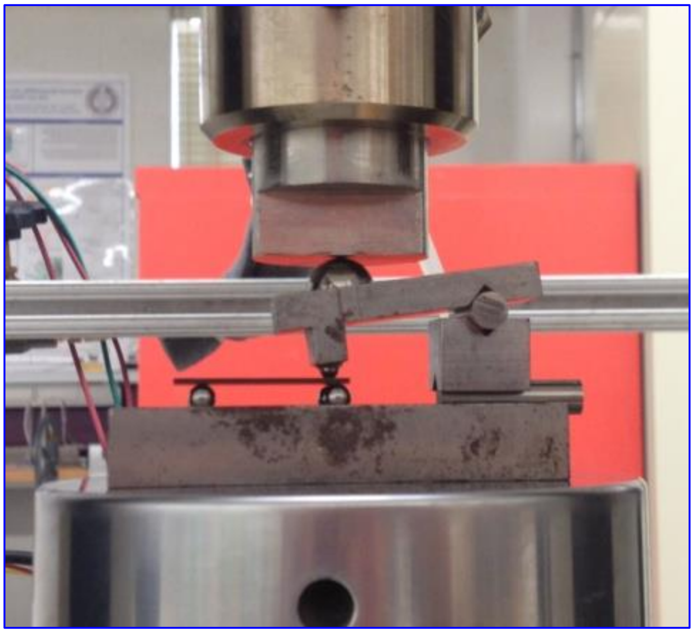

Figure 28 The set-up of double torsion

Double torsion was introduced to determine the fracture toughness of Ti_2AlC and fiber reinforced Ti_2AlC composites, Figure 28. The sample dimension for double torsion are as followed: width (S) is 20mm, length (L) is 30mm, and thickness (t) is 1mm. An initial notch with a length of 8mm was cut from one side by using the 0.5mm thick diamond saw. Then a sharp pre-crack was be induced at the notch tip by loading sample at a rate of 0.1mm/min and at a low load. Finally, the pre-cracked sample was fast fractured at a rate of 10mm/min and recorded the fracture load. The fracture toughness of all samples were calculated according to the following equations [115]:

$$K_{IC} = PS_m[\frac{3(1+v)}{St^4\delta}]^{1/2} \qquad 3.3$$

where, P is fracture load, S_m is moment arm (7 mm), S is specimen width, t is specimen thickness, v is Poisson's ratio and δ is thickness correction factor [116]. At least three of samples were tested for each compositions.

Microstructure of sintered samples and fracture surfaces were characterized with assistance of a field emission scanning electron microscope (FE-SEM; Quanta 600 FEG, FEI, Oregon, USA) equipped with energy dispersion analysis (EDA). EDA was used for analyzing the chemical composition and phases. To characterize the microstructure, the samples were grinded to 1000 grit by SiC sand paper and then polished to 1μm using diamond suspension. The fracture surface was coated with 4nm Pt layer to improve electron conductivity.

3.4 Results and Discussion

3.4.1 Characterization and Density Measurement

Table 4 shows PECSing conditions for Ti_2AlC, 20 vol.% Nextel^{TM} 720_f-Ti_2AlC and 20 vol.% Nextel^{TM} 610_f-Ti_2AlC composites together with the relative densities of the samples as determined by alcohol immersion method according to ASTM C20-00.

All samples were densified at 1275^{o}C for 30 mins at a constant load of 100MPa. The relative density of pure Ti_2AlC was about 98.0% sintered by PECSing, while the relative densities of 20 vol.% Nextel^{TM} 720$_f$-Ti_2AlC and Nextel^{TM} 610$_f$-Ti_2AlC were 99.2% and 98.5%, respectively. In the previous work on Ti_2AlC-alumina fiber composites, Joen et al.[76, 109] reported relative densities of only 93.9% for the pure Ti_2AlC and 84.4 % for 10 vol% alumina fiber- reinforced Ti_2AlC after pressureless sintering at 1400^{o}C for 4 hours. To obtain higher relative densities, Joen et al.[76, 109] had to use hot isostatic pressuring at 1400^{o}C for 4 hrs had reached the relative density of 96.2% for the pure Ti_2AlC and 97.6% for 5vol.% alumina fiber- reinforced Ti_2AlC, respectively. Results in Table 4 clearly show that comparable relative densities can be achieved in much shorter sintering time and at lower sintering temperature using PECS. The latter is particularly important to avoid reactions between alumina fibers and Ti_2AlC powder that was previously observed in the composites fabricated using hot isostatic pressing [76, 109].

Table 4 Processing conditions, density and relative density of PECSed samples.

Sample	Pressure (MPa)	Time and Temperature	Density (g/cm^3)	Relative density
Ti_2AlC	100	1275℃ for 30min	4.03±0.04	98.0%
20 vol% Nextel^{TM} 720$_f$-Ti_2AlC	100	1275℃ for 30min	3.94±0.05	99.2%
20 vol% Nextel^{TM} 610$_f$-Ti_2AlC	100	1275℃ for 30min	4.00±0.05	98.5%

Figure 29 shows the XRD patterns of as sintered Ti_2AlC samples, 20vol.% Nextel^{TM} 720$_f$-Ti_2AlC and 20vol.% Nextel^{TM} 610$_f$-Ti_2AlC composites. There are Ti_2AlC, Ti_3AlC_2 and Al_2O_3 phases to be identified in both composites patterns. Ti_3AlC_2 phase is the ancillary phase formed during Ti_2AlC process.

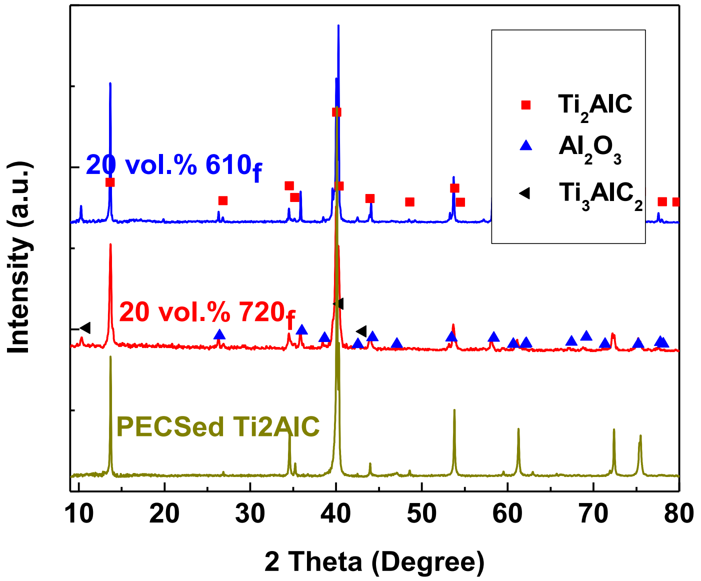

Figure 29 XRD patterns of Ti_2AlC, 20vol.% Nextel^{TM} 720$_f$ and Nextel^{TM} 610$_f$ reinforced Ti_2AlC composites.

The SEM images and EDS elemental maps of 20vol.% Nextel^{TM} 720$_f$-Ti_2AlC and 20vol.% Nextel^{TM} 610$_f$-Ti_2AlC composites are shown in Figure 30 and Figure 31. Figure 30 demonstrates that both Nextel^{TM} 720 and 610 fibers were evenly dispersed throughout the Ti_2AlC matrix, up to 20vol.%. There is a very little fiber entanglement and agglomeration, any 2-4 alumina fibers sintered to each other can observed only sporadically in the microstructure (circled in Figure).When compared to microstructure of 5vol.% alumina fiber-Ti_2AlC composites prepared by dry mixing and HIPing [109], results shown here clearly demonstrate that colloidal processing method can be used not only to uniform disperse alumina fiber reinforced Ti_2AlC composites, but also to do that with much higher fiber content of 20vol.%. The homogeneous microstructure is expected to play an important role improving mechanical properties of these composites, which is the key objective of this study.

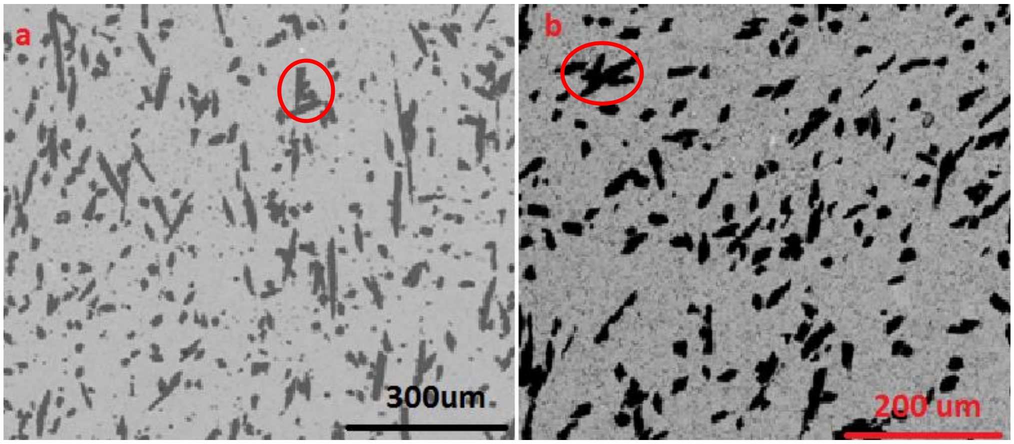

Figure 30 Back scattered electron SEM images of (a) 20vol.% Nextel^{TM} 720$_f$-Ti_2AlC and (b) 20vol.% Nextel^{TM} 610$_f$-Ti_2AlC composites. Circled areas show several alumina fibers sintered to each other.

It is worth noting here that SEM microscopy results together with EDS elemental maps shown in Figure 31 suggest that most of the Si (probably in origin form of SiO_2) still remains in Nextel^{TM} 720, but the Si element on the surfaces of Nextel^{TM} 720 diffused into matrix and reacted with Ti_2AlC. Joen et al. showed in the previous study [109] that if those composites were pressureless sintered or HIPing at 1400°C for 4 hours, almost all SiO_2 from Nextel^{TM} 720 fibers reacted with Ti_2AlC following reaction path described by Spencer et al. [76]. EDS elemental maps for Al, and Si in Figure 31, respectively, clearly show that all Al and majority of Si can be detected within the Nextel^{TM} 720 fibers after PECSing. Note here, that the area of high Si concentration is slightly smaller that of Al concentration, suggesting that some Si diffuses into the Ti_2AlC matrix and possibly reacted with it. In addition, some spots with the high Si concentration can be detected in the matrix-fiber interfaces that are most likely indicative of the Si rich reaction phase, such as $TiSi_2$ [76]. The fact that the majority of Si still remains within the Nextel^{TM} 720 fibers in not surprising because fully dense composite samples in this study are sintered at lower temperatures for shorter times when compared to the previous work [109].

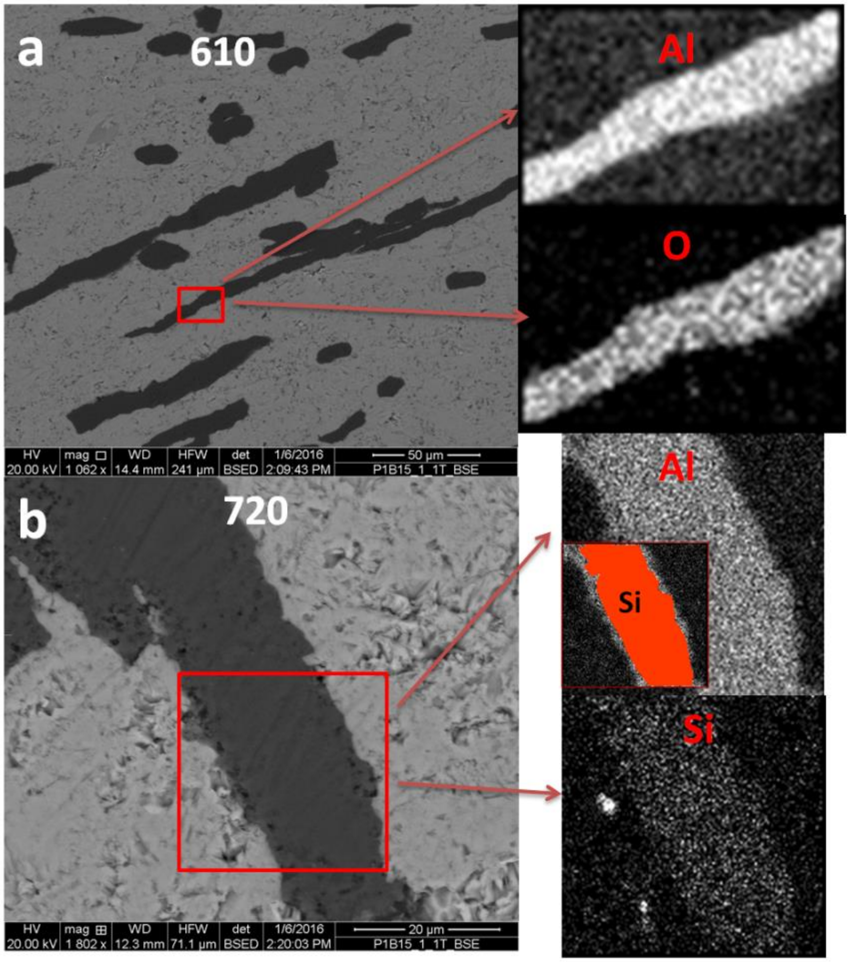

Figure 31 High magnification SEM images and EDS elemental mapping of (a) 20vol.% Nextel^{TM} 610- Ti_2AlC reinforced composite for Al and O and (b) 20vol.% Nextel^{TM} 720- Ti_2AlC reinforced composite for Al and Si. The insert in (b) is the combo of Al and Si element.

Table 5 Room temperature elastic moduli of Ti_2AlC, Nextel^{TM} 720_f-Ti_2AlC, and Nextel^{TM} 610_f-Ti_2AlC determined using RUS.

	Bulk modulus (GPa)	Shear modulus (GPa)	Young's modulus (GPa)	Poison ratio	Error (%)
Ti_2AlC	137.8	116.0	271.7	0.171	0.36
20% 720_f	146.6	119.0	280.9	0.181	0.47
20% 610_f	149.0	120.1	284.1	0.182	0.48

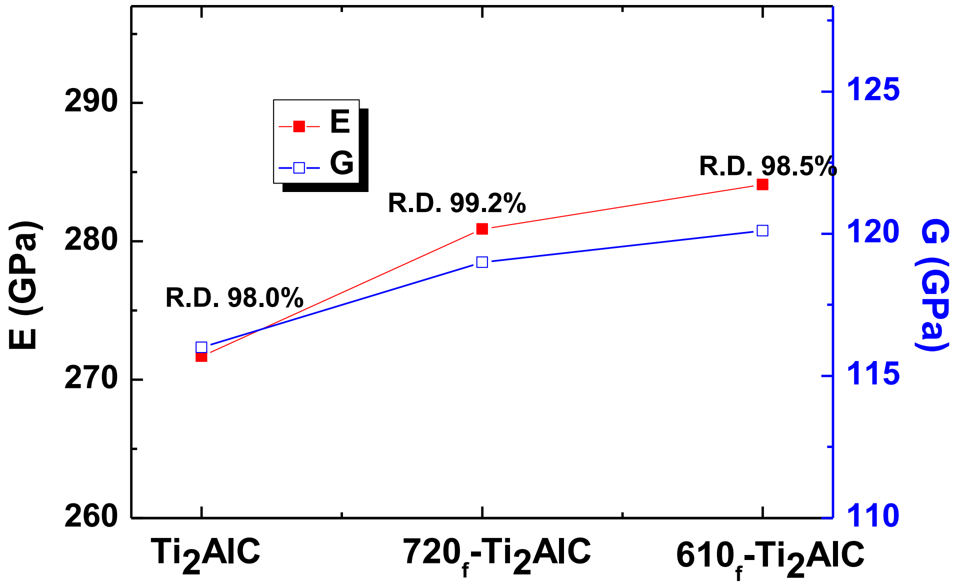

Figure 32 Elastic moduli of Ti_2AlC, Nextel^{TM} 720_f-Ti_2AlC and Nextel^{TM} 610_f-Ti_2AlC measured through RUS and relative density (R.D.) of samples are also provided on the plot.

3.4.2 Elastic Moduli

Table 5 and Figure 32 show the elastic moduli, namely bulk (B), shear (G), Young's (E) modulus, and Poison ratio (υ) of pure Ti_2AlC, 20vol.% Nextel^{TM} 720_f-Ti_2AlC and 20vol.% Nextel^{TM} 610_f-Ti_2AlC. Note that elastic moduli of Ti_2AlC reported here are in good agreement with the previous published data [40]. With addition of

20vol.% Nextel^{TM} 720 fibers, all elastic moduli slightly increase when compared to the pure Ti_2AlC, e.g. Young's modulus increases from 271.1 GPa for pure Ti_2AlC to 280.9 GPa for 20vol.% Nextel^{TM} 720_f-Ti_2AlC. However, this increase in the elastic moduli rather attributed to the higher relative density of 20vol% Nextel^{TM} 720_f- Ti_2AlC composites when compared to the pure Ti_2AlC, than to the addition of Nextel^{TM} 720 fibers because their elastic modulus of 260 GPa[111] is lower than that of Ti_2AlC. On the other hand, higher elastic moduli of 20vol.% Nextel^{TM} 610_f-Ti_2AlC can be attributed to the addition of alumina fibers because their elastic modulus of 380 GPa [111] is significantly higher than that of the pure Ti_2AlC and because those composites have lower relative density than the pure Ti_2AlC sintered in this study.

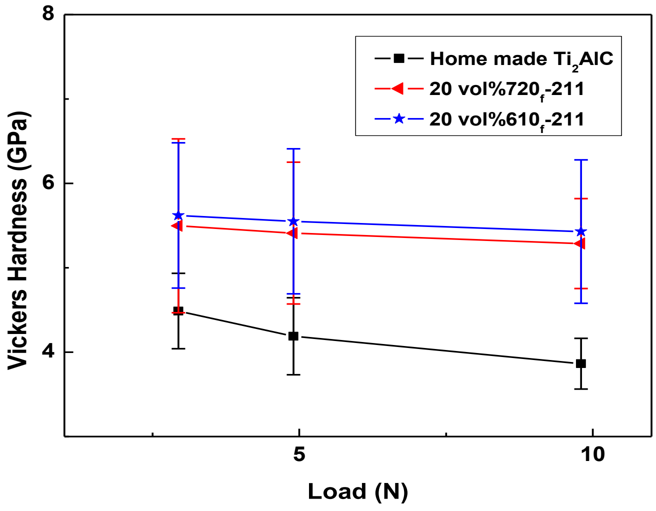

Figure 33 Vickers hardness as a function of load for Ti_2AlC, 20vol.% Nextel^{TM} 720_f-Ti_2AlC, and 20vol.% Nextel^{TM} 610_f-Ti_2AlC composites. Error bars represent standard deviations from at least 20 measurements.

Table 6 Average room-temperature compressive strengths of Ti_2AlC, 20vol.% Nextel^{TM} 720_f-Ti_2AlC, and 20vol.% Nextel^{TM} 610_f-Ti_2AlC composites at quasi-static loading conditions.

	Strength (MPa)	Increase relative to the pure Ti_2AlC
Ti_2AlC	1020±30	
20 vol% 720_f	1290±20	26.5%
20 vol% 610_f	1170±70	14.7%

3.4.3 Vickers Hardness

Although addition of both Nextel^{TM} 720 and Nextel^{TM} 610 fibers to Ti_2AlC results in almost negligible change in elastic moduli (less than 5%), it causes significant increase of hardness, Figure 33. Average Vickers hardness obtained from at least twenty measurements on each sample is plotted in Figure 33 as a function of indentation load. Figure 33 shows that at any indentation load, 20vol.% Nextel^{TM} 720_f-Ti_2AlC, and 20vol.% Nextel^{TM} 610_f-Ti_2AlC composites have higher hardness for ~35.8% than the pure Ti_2AlC. According to the previous study [109], reinforcement of Ti_2AlC with 5 vol% Nextel^{TM} 720 increased the Vickers hardness by 20%. The latter is not only in good agreement with our results, but also suggest that hardness of Ti_2AlC can easily tailored by varying amount of the reinforcement phase. Figure 33 also shows that Vickers hardness for all samples decreases slightly with increasing indentation load, until it reaches minimum value at around at 10N. Also note here, that the Vickers hardness of Ti_2AlC of 3.9±0.3 GPa at 10N is in excellent agreement with previously reported one of 4 GPa at the same loading conditions [40].

3.4.4 Quasi-static and Dynamic Compression Testing at Room Temperature

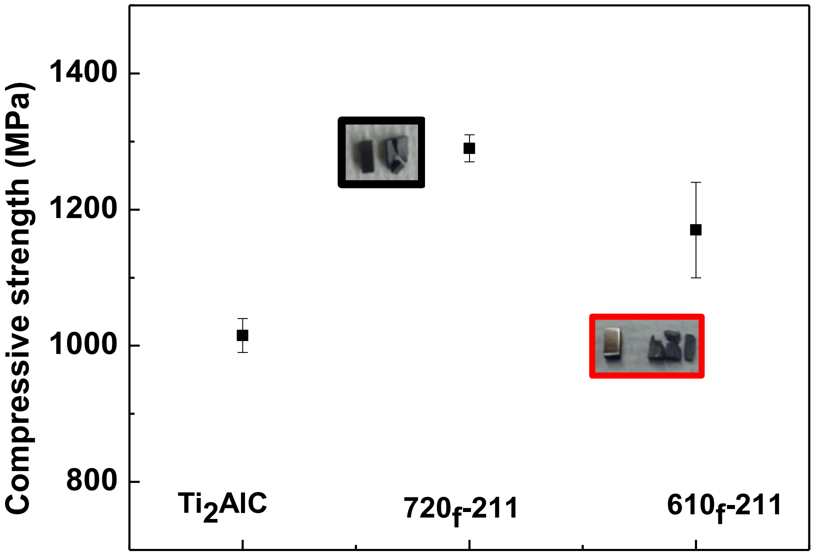

Figure 34 Average Compressive strengths of Ti_2AlC, 20vol.% Nextel^{TM} 720_f-Ti_2AlC, and 20vol.% Nextel^{TM} 610_f-Ti_2AlC composites. Inserts show photographs of selected, but typical samples after testing (Black is 20vol.% Nextel^{TM} 720_f-Ti_2AlC and red is 20vol.% Nextel^{TM} 610_f-Ti_2AlC composites).

The average values of ultimate compressive strengths of Ti_2AlC, 20vol.% Nextel^{TM} 720_f-Ti_2AlC, and 20 vol.% Nextel^{TM} 610_f-Ti_2AlC composites at room temperature are provided in Figure 34 and Table 6. The compressive strength of Ti_2AlC is 1020± 30 MPa reported here, is among highest compressive strengths of Ti_2AlC ever reported [35][36, 41] mostly because samples fabricated for this study had very small grains (average length of 5.5 μm and thickness of 4.8 μm) due to suppressed grain growth in PECSing. More importantly, results in Figure 34 and Table 6 clearly show that that strength can be additionally improved for 26.5% and 14.7% by addition of 20vol.%

Nextel^{TM} 720$_f$ and 20vol.% Nextel^{TM} 610$_f$, respectively. The strength of the 20vol.% Nextel^{TM} 720$_f$-Ti_2AlC composites is higher than that of 20vol.% Nextel^{TM} 610$_f$-Ti_2AlC ones, can be attributed to the significantly higher strength of Nextel^{TM} 720 fibers (see introduction of this paper).

As it was discussed before [35], the price one has to pay for refining the grain size in Ti_2AlC to increase its strengths with its higher brittleness. Inserts in Figure 34 show that the pure fine-grained Ti_2AlC samples tested in this study, rather shatter in the large number of pieces like typical brittle ceramics, than fail gracefully by cracking in the direction 45^o relative to the applied compressive stress like typical coarse grained MAX phases. Unfortunately, addition of Nextel^{TM} 610 and Nextel^{TM} 720 fibers (see inserts in Figure 34) seems to contribute moderately to the more graceful failure of Ti_2AlC. The stress-strain curves (not shown here) obtained in compression, also suggests more pseudo-ductile behavior of the composite samples with higher strains to failure when compared to the pure Ti_2AlC. Nevertheless, SEM images of fracture surfaces after testing in compression in Figure 35, clearly show deformation of individual Ti_2AlC grains in all samples, including the pure Ti_2AlC, not only by delamination but also by kinking. The later was considered to be the main reason for high fracture toughness, excellent damage tolerance and pseudo-ductile failure of the MAX phases when compared to other, typically brittle carbides and nitrides [2]. In addition, SEM images of the fracture surfaces in 20vol.% Nextel^{TM} 720$_f$-Ti_2AlC and 20vol.% Nextel^{TM} 610$_f$-Ti_2AlC show alumina fiber pull-outs, crack-propagation along fiber/matrix interface and cut-through the fiber can be observed.

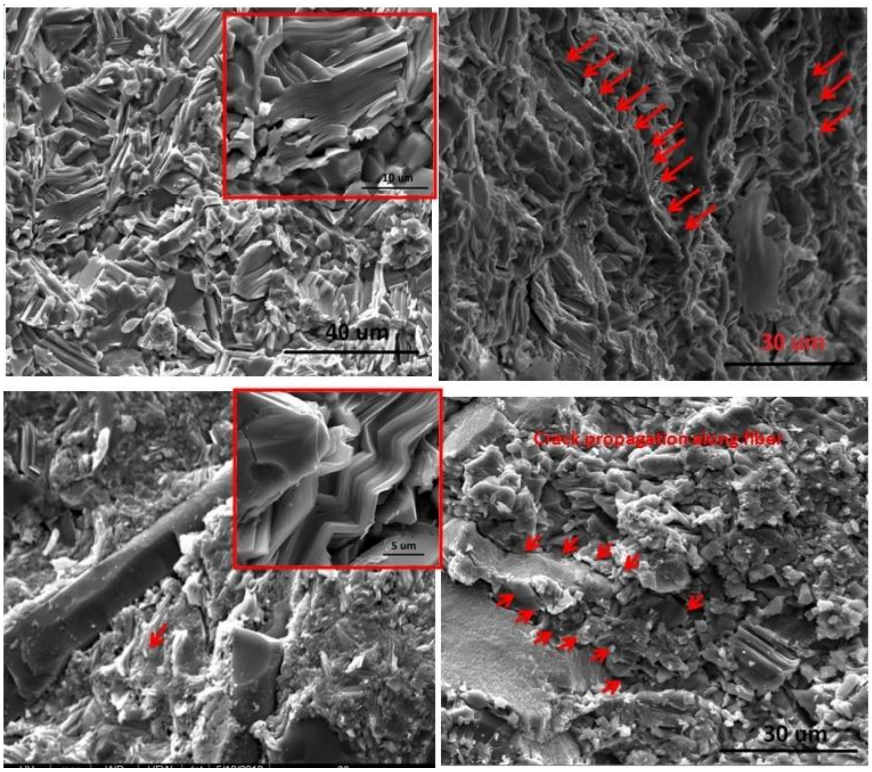

Figure 35 SEM images on the fracture surface of (a) Ti$_2$AlC, (b) 20vol.% Nextel^{TM} 720$_f$-Ti$_2$AlC and (c-d) 20vol.% Nextel^{TM} 610$_f$-Ti$_2$AlC composites after quasi-static mechanical testing in compression.

Figure 36 shows true stress vs. strain curves obtained in SHPB testing of Ti$_2$AlC, 20vol.% Nextel^{TM} 720$_f$-Ti$_2$AlC, and 20vol.% Nextel^{TM} 610$_f$-Ti$_2$AlC composites, while Figure 37 compares their average compressive strengths obtained in quasi-static and dynamic loading conditions. As in the case of the quasi-static testing, addition of 20vol.% of the Nextel^{TM} 720 and Nextel^{TM} 610$_f$ fibers result in the higher compressive strengths of the composites in dynamic testing conditions for 26.4% and 16.9%, respectively, when compared to the pure Ti$_2$AlC. In addition, selected but typical photograph of the sample after SHPB testing (insert in Figure 36) also illustrates their brittle failure since samples shattered in the large number of pieces during dynamic testing. The SEM images and fracture surfaces of the pure Ti_2AlC and alumina fibers reinforced composites after dynamic testing in Figure 38 also reveals the presence of the fiber pull outs (Figure 38 c and d). However, as it was discussed in more details in our previous work [81], Ti_2AlC fails mostly by delamination of individual grains in the dynamic loading conditions, and no evidence of kinking of individual grains can be observed on the fracture surfaces. Nevertheless, results shown here clearly demonstrate that reinforcement with alumina fibers can be used as an effective method of strengthening Ti_2AlC not only for static loading, but also for dynamic loading conditions. The latter cannot be overemphasized as the MAX phases are considered to be good candidate materials for armors and ballistic protection.

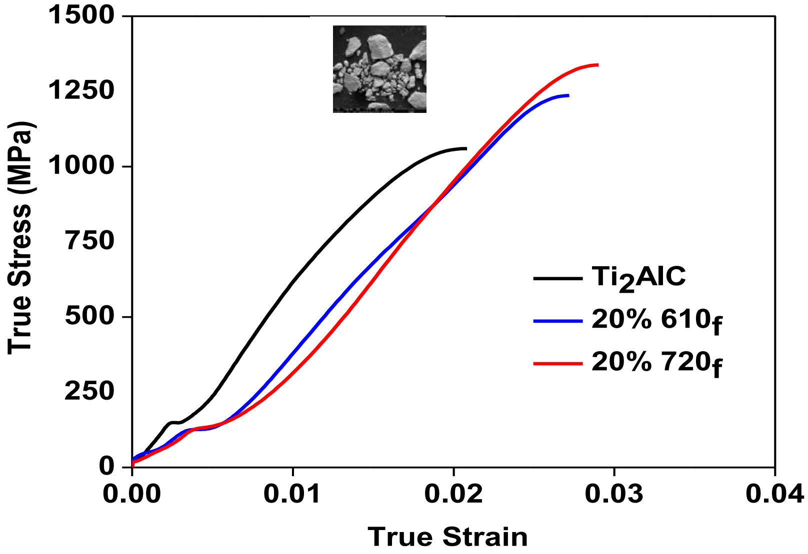

Figure 36 The true stress - strain curves of Ti_2AlC, 20vol.% Nextel^{TM} 720_f-Ti_2AlC, and 20vol.% Nextel^{TM} 610_f-Ti_2AlC composites obtained in SHPB testing. Insert shows 20vol.% Nextel^{TM} 720_f-Ti_2AlC.

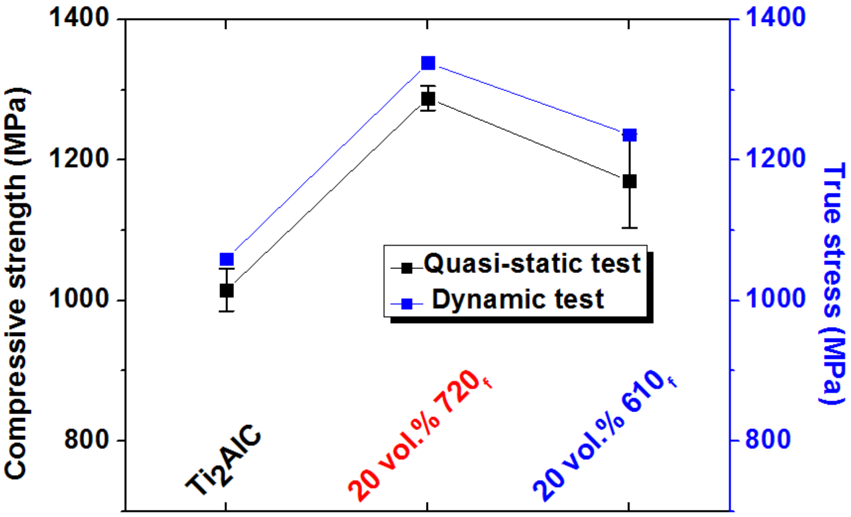

Figure 37 Comparison of average compressive strength in quasi-static and true stress in dynamic testing of Ti$_2$AlC, 20vol.% Nextel^{TM} 720$_f$-Ti$_2$AlC, and 20vol.% Nextel^{TM} 610$_f$-Ti$_2$AlC in compression. Error bars represent standard deviations from more than 3 tests.

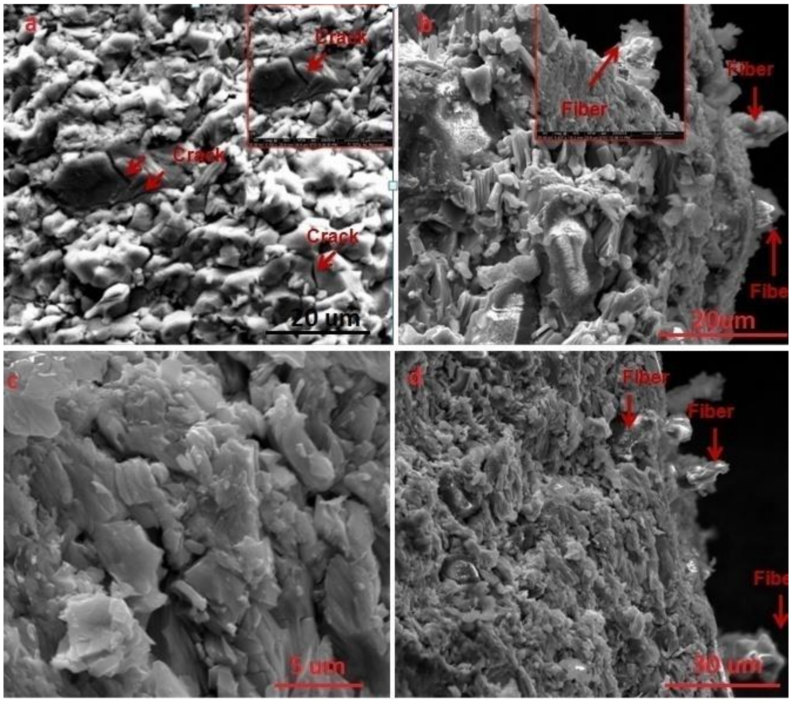

Figure 38 SEM images on the fracture surface of (a) Ti$_2$AlC, (b) 20vol.% Nextel^{TM} 720$_f$-Ti$_2$AlC, and (c,d) 20vol.% Nextel^{TM} 610$_f$-Ti$_2$AlC composites after dynamic mechanical testing in compression

3.4.5 Fracture Toughness Test

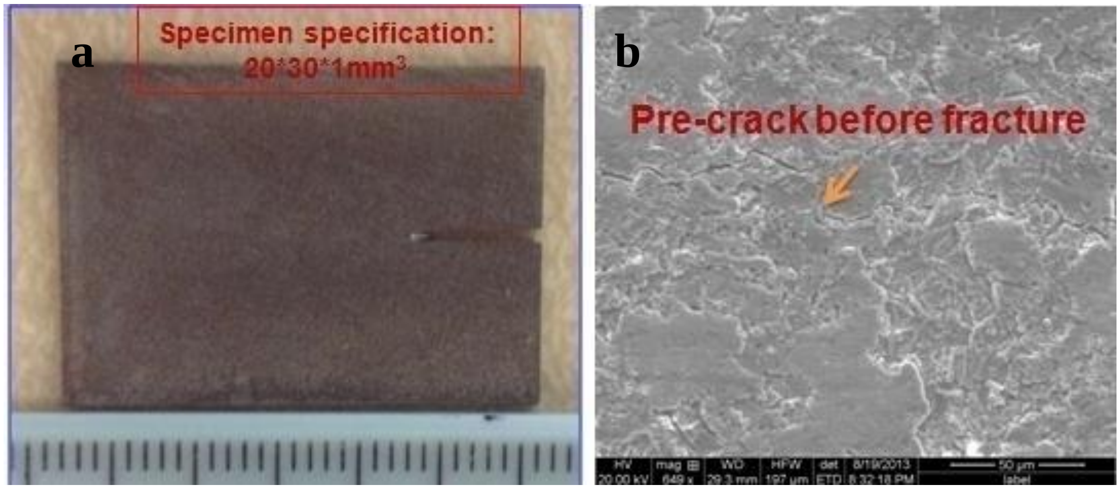

Figure 39 (a) Specimen for double torsion testing and (b) SEM image of the tensile surface of the Ti_2AlC specimen with introduced pre-crack at the tip of notch during preloading.

A double torsion specimen (Figure 39) was slowly preloaded to initiate a sharp pre-crack at the tip of the notch (Figure 39 b). As it can be seen in Figure 39 b, the crack initiated from the notch tip propagated predominantly along the grain boundary. After pre-cracking, the samples were loaded until failure and fracture toughness provided in Figure 40 was calculated from the maximum force P. The fracture toughness of 7.68 ± 0.4 MPa*$m^{1/2}$ for Ti_2AlC (Figure 40) determined using double torsion method is in good agreement with previously published values [36]. More importantly, Figure 40 shows reinforcement of Ti_2AlC with 20vol% Nextel^{TM} 720 and 20vol% Nextel^{TM} 610 fibers improves fracture toughness by 21.1% and 15.9%, respectively. Closer look at the fracture surfaces after double torsion (Figure 41) reveals that there were kinking and delaminations in all pure Ti_2AlC and both fiber reinforced composites, which is the main reason that MAX phase possesses a higher fracture toughness than ceramic. Compared with pure Ti_2AlC, besides kinking and delamination, there were also some fiber-pull-outs and crack-cut-through-fiber to be observed on composites reinforced with alumina fibers. These fiber-pull-out and crack-cut-through-fiber would need more energy to overcome, which improved the fracture toughness of Ti_2AlC as shown in Nextel^{TM} 720_f and Nextel^{TM} 610_f reinforced composites.

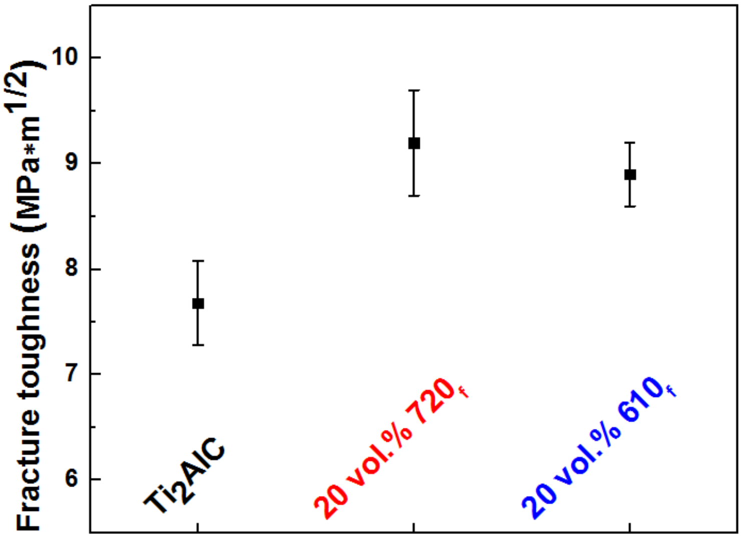

Figure 40 Fracture toughness of Ti_2AlC, and 20vol.% Nextel^{TM} 720_f-Ti_2AlC, and 20vol.% Nextel^{TM} 610_f-Ti_2AlC composites. Error bars represent standard deviations from at least 3 or 4 tests.

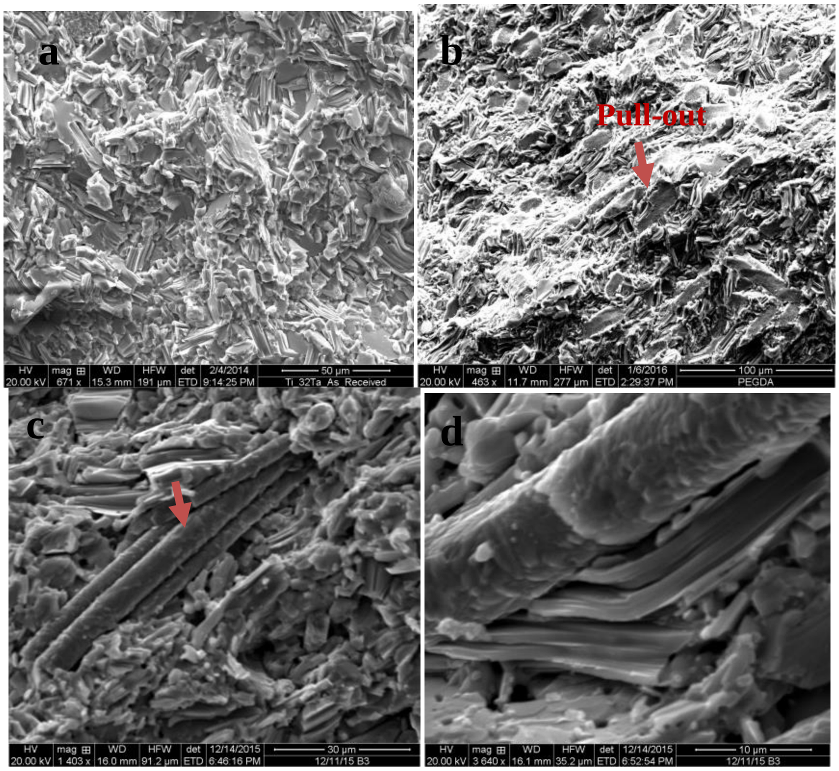

Figure 41 SEM images on fracture surfaces of (a) Ti$_2$AlC, (b) 20vol.% Nextel^{TM} 720$_f$-Ti$_2$AlC and (c and d) 20vol.% Nextel^{TM} 610$_f$- Ti$_2$AlC, respectively.

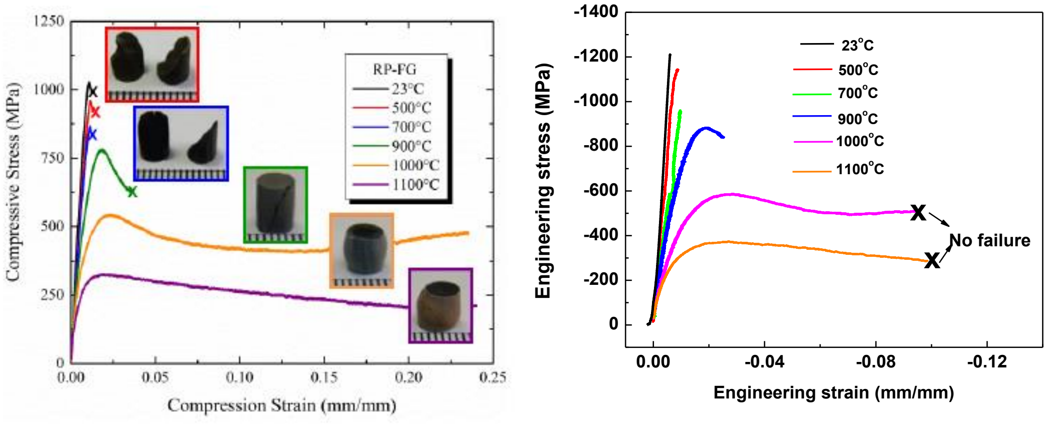

Figure 42 Typical stress-strain curves of (a) Ti$_2$AlC and (b) 20vol.% Nextel^{TM} 610$_f$-Ti$_2$AlC obtained in compression at different temperatures. Note that in both cases tests at 1000^{o}C and 1100^{o}C were aborted before failure of the specimens..

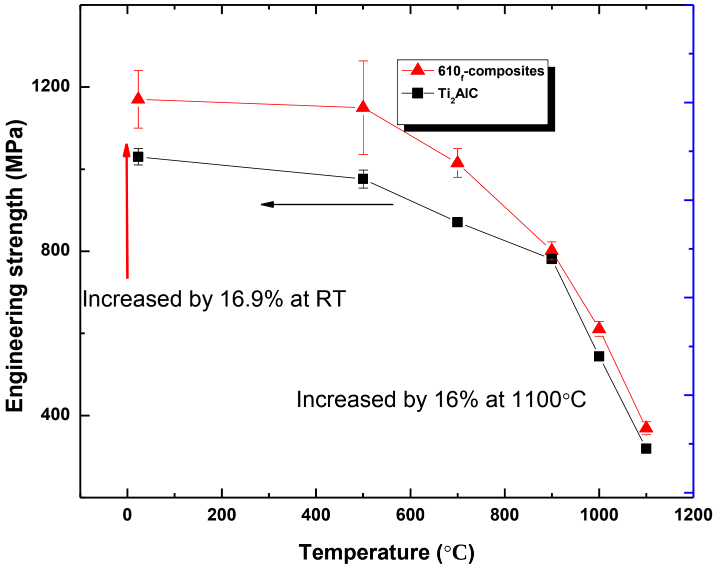

Figure 43 Compressive strength of Ti_2AlC and Nextel™ 610 fiber reinforced composites at elevated temperature; Note that strains to failure at 1000°C and 1100°C are larger than plotted here because those tests were aborted before total failure of the samples. Error bars represents standard deviation from 3 tests.

3.4.6 Mechanical Properties at Elevated Temperatures in Compression

To study effect of Al_2O_3 fiber reinforcement on the mechanical properties of Ti_2AlC at elevated temperatures, 20vol.% Nextel™ 610_f-Ti_2AlC composite and pure T_2AlC were tested in compression at temperatures ranging from the room temperatures to 1100°C. Although 20vol.% Nextel™ 610_f -Ti_2AlC composites show lower room temperature compressive strengths than 20vol.% Nextel™ 720_f -Ti_2AlC (Figure 34 and Table 5), they were chosen for testing at high temperature because Nextel™ 720_f were expected to degrade after long term exposure to high temperatures by diffusion of Si form the fibers and reaction with Ti_2AlC matrix, as it is discussed in more details elsewhere [76, 109]. The typical stress-strain curves of 20vol.% Nextel^{TM} 610$_f$ -Ti_2AlC composite are shown in Figure 42. Note here that all tests at 1000°C and 1100°C were aborted before failure to prevent eventual damage of the high-temperature extensometer. Stress-strain curves in Figure 42 illustrate that like all other MAX phases [20, 43], both pure Ti_2AlC and 20vol.% Nextel^{TM} 610$_f$ -Ti_2AlC behave more or less as brittle solids below BPT temperature of around 900°C with the very little plastic deformation (less than 4%) before failure. However, above BPT temperature, they show pseudo-ductile behavior with strains to failure exceeding 18%.When peak compressive stresses and strain to failure are plotted as a function of temperature in Figure 43, it is clear that in the increase in strain to failure above BPT temperature is accompanied by significant decrease in compressive strengths. More importantly, results in Figure 43 show that strengths of 20vol% Nextel^{TM} 610$_f$ -Ti_2AlC composites starts to decline more significantly below BPT temperature when compared to the pure Ti_2AlC. The later observation can be attributed to more significant decrease in the strength of Nextel^{TM} 610 fibers below BPT temperature when compared to Ti_2AlC, i.e. the strengths of Nextel^{TM} 610 at 700 °C is only ~75% of that at room temperature [117] while the strengths of Ti_2AlC at the same temperature is still ~84% of room temperature strength. However, above BPT temperature decline of the strength with the temperature is more noticeable in Ti_2AlC than in Nextel^{TM} 610; i.e. strengths of Nextel^{TM} 610 and Ti_2AlC are 60% and 31% of corresponding strengths at room temperatures, respectively. Therefore, compressive strengths of 20vol.% Nextel^{TM} 610$_f$ -Ti_2AlC composites decreases initially more significantly with temperature than that of the pure Ti_2AlC, reaching almost identical values at 900^{o}C. However, above BPT temperature, decrease in compressive strength with the temperature is less pronounced for 20vol.% Nextel^{TM} 610$_f$ -Ti_2AlC than for Ti_2AlC. As a results, improvements in compression strength of Ti_2AlC strengths by addition of 20vol.% Nextel^{TM} 610$_f$ fibers, drops from ~16.9% at room temperature to only ~8% at BPT temperature of 900^{o}C and then it increases again to ~16% at 1100^{o}C. This finding is encouraging because it suggest that alumina fibers can be used for strengthening Ti_2AlC even above BPT temperature. SEM images of the polished cross-sectional surfaces (Figure 44) in reveal numerous microcracks that deflect at the fiber-matrix interfaces, some fiber poll puts and also some cracks passing through the fibers. The former two mechanisms clearly contributes to the higher strength of 20vol.% Nextel^{TM} 610$_f$ -Ti_2AlC above 900^{o}C.

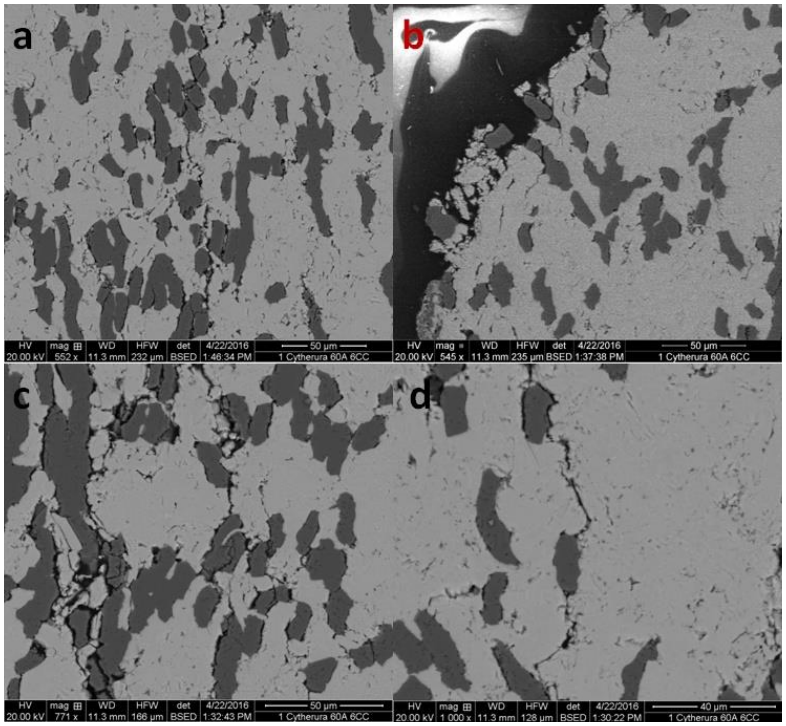

Figure 44 SEM images of the polished cross sectional surface of 20vol.% Nextel^{TM} 610$_f$ -Ti_2AlC composites testing at 1100^{o}C.

3.5 Conclusion

In this study, 20vol.% Nextel^{TM} 720$_f$-Ti$_2$AlC and 20vol.% Nextel^{TM} 610$_f$-Ti$_2$AlC composites were successfully fabricated through colloidal processing and densified by pulse electric current sintering (PECS), with the evenly dispersed Nextel^{TM} 720$_f$ and Nextel^{TM} 610$_f$ in the Ti$_2$AlC matrix, without any fiber entanglement or agglomeration. No reaction between alumina fibers and Ti$_2$AlC has been observed in all fabricated samples. Addition of Nextel^{TM} 720$_f$ and Nextel^{TM} 610$_f$ short fibers (~150 μm in length) into the Ti$_2$AlC matrix results in minor increase of stiffness (i.e. Young's modulus increases for less than 5%). However, fabricated composites where found he have improved harness for more than 35.8% when compared to the pure Ti$_2$AlC. Room temperature compressive strengths of 20vol.% Nextel^{TM} 720$_f$-Ti$_2$AlC and 20vol.% Nextel^{TM} 610$_f$-Ti$_2$AlC composites were found to be higher than that of Ti$_2$AlC for more than 26.5% and 14.7%, and 26.4% and 16.9% in both quasi-static and dynamic conditions, respectively. In addition, the room temperature fracture toughness was improved for 21.1% and 15.9% in both 20vol.% Nextel^{TM} 720$_f$-Ti$_2$AlC and 20vol.% Nextel^{TM} 610$_f$-Ti$_2$AlC composites, respectively. Improved mechanical properties can be attributed to the crack deflections at the finer-interface matrix and some moderate fiber pull outs. It was also found that attrition of 20vol.% Nextel^{TM} 610 to the Ti$_2$AlC improves not only compressive strength below brittle to plastic transition temperature of 900^{o}C, but also above it, up to 1100^{o}C. In summary, results of this study implies strongly that alumina fibers can be used to improve mechanical properties of the Ti$_2$AlC at both room and high temperatures. The latter is particularly important since Ti$_2$AlC is consider as a potentially good structural material for high temperature applications because its excellent oxidation resistance.

4. STRUCTURAL, PHYSICAL AND MECHANICAL PROPERTIES OF $Ti_3(Al_{1-x}Si_x)C_2$ SOLID SOLUTION WITH X=0-1

4.1 Synopsis

A series of high-purity $Ti_3(Al_{1-x}Si_x)C_2$ solid solutions with 0<x<1 were reaction sintered from Ti, Si, Al and TiC powders using Pulsed Electric Current Sintering (PESC)[4]. With increasing amount of Si in this MAX phase, the a-lattice parameter remains constant at approximately 3.07 Å, while the c-lattice parameter decreases linearly from 18.58 Å to 17.63 Å. The specific heat capacity of $Ti_3Al_{0.6}Si_{0.4}C_2$ solid solution was found to be comparable to that of end members, namely Ti_3AlC_2 and Ti_3SiC_2. However, coefficient of thermal expansion (*CTE*) of $Ti_3Al_{0.6}Si_{0.4}C_2$ solid solution is lower than that of the end members, while both Young's and shear moduli increase with increasing amount of Si. Vickers hardness (H_v) results demonstrate significant hardening effect in $Ti_3(Al_{1-x}Si_x)C_2$ solid solutions regardless of the grain size , i.e. it changes from 4.1±0.14 GPa of Ti_3AlC_2 and 4.2±0.37 GPa of Ti_3SiC_2, up to 5.6±0.2 GPa for $Ti_3(Al_{0.4}Si_{0.6})C_2$. At room temperature, the strengthening effect was found to be marginal for fine grained (FG-) structure, as the compressive strength of $Ti_3Al_{0.6}Si_{0.4}C_2$ and $Ti_3Al_{0.4}Si_{0.6}C_2$ is higher for only 7.3% when compared with the end members. However, significant strengthening effect was observed in coarse grained (CG-) structures as the room temperature compressive strength of solid solutions exceed those of two end members for more than 25.8%. Nevertheless, above brittle-to-plastic

---

[4] This method is commonly but inadequately referred to as spark plasma sintering (SPS)

transition temperature, the solid solution strengthening effect diminishes and the strength of Ti_3SiC_2 is higher than that of Ti_3AlC_2 and solid solutions. Finally, it was found that $Ti_3Al_{0.6}Si_{0.4}C_2$ forms protective alumina oxide layer at 1200^oC, rather than silica that is commonly found on oxidized surfaces of Ti_3SiC_2.

4.2 Introduction

The MAX phases are the family of more than 70 ternary carbides or nitrides with layered nanolaminated structure having P63/mmc hexagonal crystal structure and common chemical formula $M_{n+1}AX_n$ phases, where M is transition metal, A is A-group element and X is carbon or nitrogen, and n =1-3 [1, 2, 9]. The MAX phases are sometimes referred to as "metallic ceramic" since they have the unique combination of properties that place them in the middle ground between the typical ceramic and metals [9, 16]. On one hand, MAX phases, like other typical ceramics, have high stiffness, chemical and oxidation resistances, high hardness, low coefficient of thermal expansion and good thermodynamic stability up to high temperatures [9]. However, they have good thermal and electrical conductivity, good thermal shock resistance and can be even easily machined like typical metals [2, 9, 16, 38, 70]. Their properties are even more remarkable when one considers that they can be compressed to stresses over 1 GPa, showing fully reproducible stress-strain hysteresis loops while dissipating 25% of the mechanical energy [15, 26]. At higher temperatures, however, MAX phases undergo a brittle-to-plastic transition (BTP) [21] and can be plastically deformed for more than 25% before failure even under tension [15, 21, 26]. Finally, they can be fabricated inexpensively using a variety of reaction sintering methods [9].

Numerous studies suggested in the past that substitution on M, A, or X site in $M_{n+1}AX_n$ can improve physical, chemical and mechanical properties of MAX phases. Thus, MAX phase solid-solutions hold potential for tailoring properties of this class of materials for different applications [6, 44, 77, 89, 118-121] by substitution (alloying) on (1) M site; (2) A site; and/or (3) X site[38]. The elements used for substitution are generally neighboring elements in the periodic table of elements with similar atomic radii and electronic structure. Until now, approximately 100 different solid solutions have been fabricated and characterized. Some examples of the most studied ones include $(Cr_{1-x}V_x)_2AlC$[122], $(Ti,Nb)_2AlC$[41], $Cr_2(Al_{1-x}Si_x)C$[123], $(Ti_{0.5}V_{0.5})_3AlC_2$[6], $Ti_3(Al_{0.75}Si_{0.25})C_2$[40, 124, 125], $Ti_3Al_xSn_{1-x}C_2$[86], $Ti_3Ge_xSi_{1-x}C_2$[126, 127], $Ti_2Al(C_{0.5}N_{0.5})$[36, 46] and $Ti_3Al(C_{0.5}N_{0.5})_2$ [17]. A number of theoretical studies have also addressed phase stability, electronic, elastic, thermal and optical properties of different MAX phase solid solutions [128-131]. Most recently, we have shown, using cluster expansion method, that the number $(M_x,M'_{1-x})_2AX$ phase solid solutions can be significantly extended even to those compositions having M' alloying elements that otherwise does not end member MAX phase [132]. Previous studies also showed that while some solid solutions such as $Ti_3(Al_{0.75}Si_{0.25})C_2$[40, 124, 125], $Ti_3Al_xSn_{1-x}C_2$[86, 133] and $Ti_2Al(C_{0.5}N_{0.5})$[36, 46] showed the improved mechanical properties due to solid solution hardening effect, the others, such as $Cr_2(Al_{1-x}Si_x)C$ [123], $Ti_3Ge_xSi_{1-x}C_2$[126, 127], $(Ti,Nb)_2AlC$[41, 90], show the opposite effect, i.e. solid solution softening. The reason for observed hardening effect in some MAX phase solid solutions, and softening in the others, are not completely clear at this moment [86, 125, 127, 134].

Because Ti_3SiC_2 and Ti_3AlC_2 are the most studied and the best characterized members of MAX phases, it is not surprising that $Ti_3(Al_{1-x}Si_x)C_2$ are the most characterized solid solutions to date[40, 125, 129, 134, 135]. $Ti_3(Al_{1-x}Si_x)C_2$ solid solutions are expected to have a good combination of properties that are important for their application as a high-temperature structural materials. It is suggested that $Ti_3(Al_{1-x}Si_x)C_2$ solid solutions like Ti_3AlC_2 could provide good oxidation resistance due to formation of the pure alumina protective oxide layer [135, 136], maybe also possess better mechanical properties like Ti_3SiC_2 [40, 125]. However, Lee et al. and Nguyen et al. showed that oxidation of $Ti_3(Al_{0.5}Si_{0.5})C_2$ and $Ti_3(Al_{0.7}Si_{0.3})C_2$ in the 900-1200^oC temperature range results in formation of mixed oxide layers consisting of rutile-TiO_2, Al_2O_3 and amorphous SiO_2 [135, 137]. Correspondingly, like in the case of other MAX solid solutions, there is no strong agreement on solid solution hardening and strengthening effects in $Ti_3(Al_{1-x}Si_x)C_2$. For example, Zhou et al. demonstrated that as x increases from x=0 to x=0.25 in $Ti_3(Al_{1-x}Si_x)C_2$, the Vickers hardness and room temperature compressive strength increased up to 26% and 29%, respectively [125]. In addition, first principle studies by Son at al. [138] also showed significant hardening effect in $Ti_3(Al_{1-x}Si_x)C_2$ solid solution due to chemical hardening caused by strong Si-Al interactions in A layer. However, on the other paper, it indicated there was no hardening effect, which the Vickers hardness decreased linearly from Ti_3SiC_2 to Ti_3AlC_2 [129]. It is worth noting here that all previous experimental and theoretical studies on $Ti_3(Al_{1-}$

${}_{x}\text{Si}_{x})\text{C}_{2}$ agree that lattice parameters and elastic moduli of $\text{Ti}_3(\text{Al}_{1-x}\text{Si}_x)\text{C}_2$ solid solutions lie in between the two end members [129-131].

In this study, a series of high-purity $\text{Ti}_3(\text{Al}_{1-x}\text{Si}_x)\text{C}_2$ (x= 0, 0.2, 0.4, 0.6, 0.8 and 1.0) were reaction sintered from Ti, Al, Si, and TiC powder mixtures. A systematic experimental study of structure, lattice parameters, thermal expansion coefficients, heat capacities and elastic properties are carried out to determine the effects amount of Si in $\text{Ti}_3(\text{Al}_{1-x}\text{Si}_x)\text{C}_2$ on structural and physical properties. In addition, hardening and strengthening effects in $\text{Ti}_3(\text{Al}_{1-x}\text{Si}_x)\text{C}_2$ are studied and discussed in more detail. Finally, oxidation of $\text{Ti}_3(\text{Al}_{1-x}\text{Si}_x)\text{C}_2$ solid solutions at 1200°C is compared to that of the end members.

4.3 Experimental Details

Table 7 The optimized compositions and sintering conditions for $\text{Ti}_3(\text{Al}_{1-x}\text{Si}_x)\text{C}_2$ through PECS, where x =0-1.

x	Nominal composition of the powder mixture	Sintering conditions
0	Ti:Al:C=3:1.2:1.8	1510°C for 15min
0.2	Ti:Al:Si:C=3:0.96:0.24:1.8	1550°C for 15min
0.4	Ti:Al:Si:C=3:0.72:0.45:1.9	1560°C for 15min
0.6	Ti:Al:Si:C=3:0.45:0.73:1.9	1560°C for 15min
0.8	Ti:Al:Si:C=3:0.24:0.96:1.9	1580°C for 15min
1.0	Ti:Si:C=3: 1.2:1.85	1600°C for 15min

Commercial Ti (44µm average particle size, 99.5% purity), Si (44µm average particle size, 99.5% purity), Al (44µm average particle size, 99.5% purity) and TiC powders (2–3µm average particle size, 99.5% purity), (all purchased from Alfa Aesar, MA, USA), were used as starting raw materials to synthesize $\text{Ti}_2(\text{Al}_{1-x}\text{Si}_x)\text{C}_2$ MAX phase solid solutions, with x =0, 0.2, 0.4, 0.6, 0.8 and 1.0, respectively. A series of different powder mixtures were reaction sintered using pulsed electric current sintering (PECS)[5]. The nominal compositions of Ti:Al:TiC powder mixture and sintering conditions in Table 7 were optimized to fabricate the bulk samples with small amount of impurities (second phases) and comparable grain sizes. The powder mixtures were mixed homogeneously by ball-milling in a glass jar using zirconia beads for 24hrs at a speed of 300rpm. Ball-milled powder mixtures were poured into a cylindrical graphite die with an inner diameter of 20mm and reaction sintered using PECS in the 1500–1600°C temperature range with a heating rate of 50°C /min, and the holding time of 15min. Before heating, the PECS chamber was evacuated to 10^{-6} torr and after that sintering was carried out under constant flow of ultra-high purity argon (99.999%). A constant loading of 50 MPa was applied throughout the sintering process while the cooling rate was 200°C/min. The density and relative density of sintered of sintered $Ti_3(Al_{1-x}Si_x)C_2$ solid solutions were determined to ASTM C20-00 standard using alcohol immersion Archimedes' method described in more detail elsewhere [26, 99].

The surfaces of all samples was polished to characterize their microstructure and composition. The phase identification of samples sintered at different temperatures was conducted using X-ray diffraction (Mode D8 Advance, Bruker AXS, Madison, WI) using a Cu_α radiation, at a rate of 0.015s/step and a step time of 0.2s. The microstructure of all samples and fracture surfaces after mechanical testing were characterized using a field emission scanning electron microscope (FE-SEM; Quanta 600 FEG, FEI, Oregon) equipped with energy dispersion analysis (EDA). The later was used to analyze chemical

---

[5] This method is commonly but inaccurately referred to as Spark Plasma Sintering (SPS).

composition of the phases. The surfaces of samples were prepared for FE-SEM microstructural analysis by grinding them with SiC sand paper (up to 1000 grit) and polishing with diamond suspension (up to 1μm). To expose the grains and determine the grain size, the polished surfaces were also etched for 10-15 seconds using a solution of $2H_2O:1HNO_3:1HF$. The grain size of more than 50 grains in each sample was measured from SEM images using the ImageJ software.

The specific heat capacity at the constant pressure were determined from differential scanning calorimetry (DSC Q 20, TA Instrument, New Castle, DE) results obtained in the -50°C and 300°C temperature range, following the procedure described in ASTM E 1269 standard. All tests were carried out under dry nitrogen with the flow of 50ml/min throughout. Each sample was heated and cooled twice with the rate of 10°C/min and dwelling time of 4minutes at -50°C and 300°C. Prior to the testing, the heat flows of an empty alumina specimen holder and a synthetic sapphire standard (TA Instruments, New Castle, DE) were also separately measured. Then, the specific heat capacity of $Ti_2(Al_{1-x}Si_x)C_2$ was calculated as $C_{sp} = C_{st} \cdot \frac{D_{sp} \cdot W_{st}}{D_{st} \cdot W_{sp}}$ where, C_{sp} and C_{st} are the specific heat capacity of the $Ti_2(Al_{1-x}Si_x)C_2$ specimens and sapphire standard, respectively. D_{sp} and D_{st} indicate the vertical displacement between the sample or sapphire standard and the empty specimen holder, and W_{st} and W_{sp} represent the weight of sapphire standard and sample, respectively.

Coefficients of thermal expansion (CTEs) of solid solutions and end members were determined using Thermo-mechanical Analyzer (TMA Q 400, TA Instrument, New Castle, DE) according to ASTM E 831 standard. All specimens were EDM-machined into disks with a diameter of 5mm and a thickness of 8mm. A constant load of 0.1 N was applied through the probes to ensure a perfect contact between the probe and sample surfaces. All samples were tested in two heating-cooling cycles at a rate of 5^{o}C/min between 25^{o}C and 600^{o}C, and a dwelling time of 5minutes at the initial and final temperatures. The coefficient of thermal expansion was calculated from the following equation:$CTE = \frac{\Delta L * k}{L * \Delta T}$, where, α is the coefficient of thermal expansion, ΔL is the change of specimen length, ΔT is the temperature difference over which the change in specimen length was measured and k is calibration coefficient.

Elastic modulus were determined at room temperature using Resonant Ultrasound Spectroscopy (RUS, Magnaflux Quasar Systems, NM) following procedures described in more detail elsewhere [40, 99, 112]. All RUS samples were machined into parallelepipeds with sharp edges and a parallelism within 1% error. The samples were supported by three sapphire transducers -one transmitting a sinusoidal continuous-wave signal with a constant amplitude but varying frequencies in the range of 0 to 400 kHz and the other two ones detecting the oscillation response directly from the sample. Young's and shear moduli were determined from the corresponding resonance spectrum for the sample of known weight, geometry and dimensions using Quasar RuSpec software (Magnaflux Quasar Systems, NM). Quasar RuSpec software was able to iteratively minimize error between the measured and calculated resonant peaks by changing the c_{11} and c_{44} constants until the acceptable error (<0.3%) between measured and calculated frequencies of renounce peaks was obtained.

The Vickers hardness of all samples was determined using Micro-hardness Tester LM 300AT (LECO, MI) at indentation loads of 5N and 10N. Vickers hardness was calculated as $H=2P/d^2$, where P is indentation load, d is the average length of indent's diagonals. At least twenty runs were made at each indentation load, the data reported here are the statistic average of those measurements.

The ultimate compressive strength of samples was determined using 810 Materials Testing System (MTS 810, MN) at different temperatures ranging from room temperatures to 1100°C. Cylindrical specimens with a diameter of 5mm and a height of 8mm were machined from the center of reaction sintered discs using electron-discharge-machining. Both flat surfaces on the specimens were gently grinded to shape edge and a obtain parallelism with <1% using 1000 grit grand papers. The sample was sandwiched between two SiC spacers and a high precision, high temperature extensometer (632.59E-77, MTS, USA) was attached to the spacers to record the strain. The uniaxial compressive tests are under the displacement control mode with a strain rate of 10^{-4}s.

4.4 Results and Discussion

4.4.1 Structural Characterization of $Ti_3(Al_{1-x}Si_x)C_2$ Solid Solutions

A series of reaction sintering experiments, followed by XRD analysis were carried out to optimize nominal composition of powder mixtures and sintering conditions and ultimately fabricate XRD phase-pure samples of $Ti_3(Al_{1-x}Si_x)C_2$ with x =0, 0.2, 0.4, 0.6, 0.8 and 1.0. Since melting points of Al (660°C) and Si (1414°C) and their evaporation rates are different at different sintering conditions, Ti:Al:Si:C ratio in the initial powder mixtures and sintering conditions has to be carefully adjusted to obtain XRD phase pure $Ti_3(Al_{1-x}Si_x)C_2$ with the minimal amount of secondary phases (mostly binary intermetallic and TiC) that could be (i) in thermodynamic equilibrium with the MAX phases if final chemistry of the product deviates from the stoichiometry of the MAX phase; or (ii) result of incomplete reaction during sintering. In addition, graphite die in PCES creates carbon rich environment during sintering, and thus amount of carbon in the initial powered mixtures was adjusted to substoichiometric to avoid formation of TiC. The optimized nominal compositions of the initial powders and sintering conditions are summarized in Table 7. As it can be seen in the above Table, the sintering temperature has to be gradually elevated from 1510^{o}C for Ti_3AlC_2 to 1600^{o}C for Ti_3SiC_2 with increasing Si content in solid solutions to promote liquid assisted reaction sintering. In addition, about extra 10-20% Al and Si was added to initial powder mixture to compensate their evaporation during sintering process and amount of the molten metal and intermetallic compounds that squeezes out through the gap between punch and die during initial stages of sintering process [34, 58, 60].

Figure 45 shows the XRD patterns of $Ti_3(Al_{1-x}Si_x)C_2$ MAX phase solid solutions obtained using optimized nominal compositions of initial powders and sintering condition in Table 7. As it can see from XRD results in Figure 45, all sintered samples are pure and contain mainly $Ti_3(Al_{1-x}Si_x)C_2$ MAX phase. However, a small amount of TiC phase is present in samples when x is above 0.4. Further analysis of XRD patterns indicated that amount of TiC was always below 3.6 wt%. Figure 45 also shows a shift of some XRD peaks with increasing Si content; the most obvious one is that of (002) peak which shifts from 9.3° to 9.9° with increasing Si content, indicating the Si was successfully partially substitute Al sites in MAX phase.

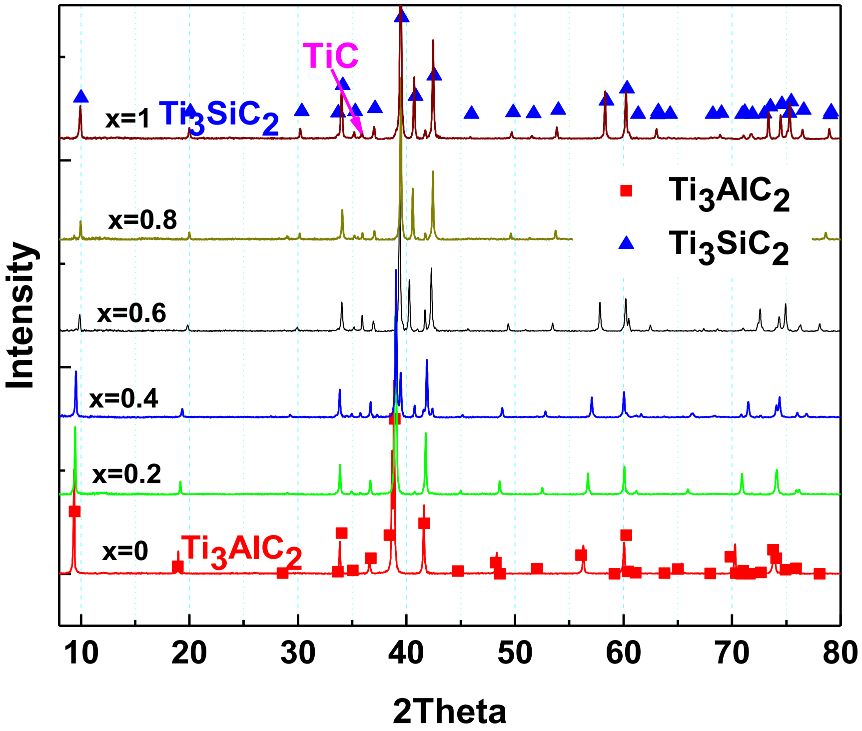

Figure 45 XRD patterns of $Ti_3(Al_{1-x}Si_x)C_2$ after PECS, where x =0, 0.2, 0.4, 0.6, 0.8 and 1.0, respectively. Triangles and squares denote peak positions for Ti_3SiC_2 and Ti_3AlC_2.

The a- and c- lattice parameters retrieved from these XRD patterns using Jade software (Christchurch, New Zealand) are plotted in Figure 46 as a function of x in $Ti_3(Al_{1-x}Si_x)C_2$. It shows no changes in the a-lattice parameter with increasing Si content (Ti_3AlC_2: 0.3072nm; Ti_3SiC_2: 0.3065nm). However, the c-lattice parameter decreased linear from 1.86nm to 1.78nm with increasing amount of Si in solid solutions as the radius of Si is less than that of Al atom. The lattice parameters of Ti_3AlC_2 and Ti_3SiC_2

reported here (Ti_3AlC_2: a=0.3072nm, c=1.854nm; Ti_3SiC_2: a=0.3065, c=1.767nm) are in good agreement with previously reported experimental values (Ti_3AlC_2: a=0.3073nm, c=1.858nm [48]; Ti_3SiC_2: a=0.3066, c=1.763nm [139]). However, although the experimental values of a- and c- lattice parameters reported here for solid solutions are slightly below those obtained in previous ab initio calculations [128, 130], their changes with Si content follow the same trend as predicted in those studies. Son et al. [128] suggested that the observed trend can be explained to be result of the charge density of A element and consequently stronger ionic and covalent character of M-A bonds with increasing Si content on the A sites.

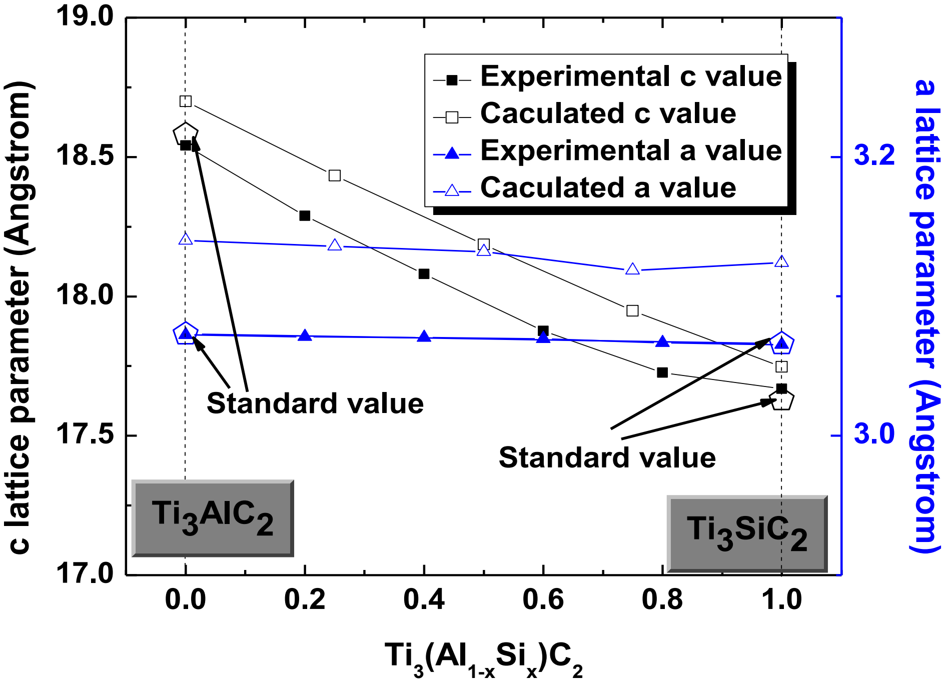

Figure 46 The c-lattice and a-lattice parameters as a function of Si content, which are obtained from XRD patterns in this study and first principle calculation in the previous work, respectively.

Selected , but typical SEM image of $Ti_3(Al_{0.2}Si_{0.8})C_2$ obtained in back scattered mode is shown in Figure 47, together with Ti, Al and Si EDS elemental maps. Although the XRD results in Figure 45 show no presence of other phases but $Ti_3(Al_{0.2}Si_{0.8})C_2$. Figure 47 suggests (see darker gray phases in Figure 47a) that sample contains a small amount of secondary phases. Analysis of SEM back-scattered images and EDS results for all sintered samples (not shown here) revealed that main secondary phases were TiC, $TiSi_x$ and/or $TiAl_x$ intermetallic, and that their total amount was very small, i.e. always below 5%. Therefore, it is not surprising those secondary phases could not be detected in XRD patterns.

Table 8 Heat treatment conditions for grain growth in ultra-purity argon flow.

Sample	Condition
X=0	1350^{o}C for 24hr
X=0.4	1350^{o}C for 24hr
X=0.6	1400^{o}C for 28hr
X=1	1450^{o}C for 24hr

Surfaces polished for SEM were further etched to expose grains and measure their length and width, and those results are summarized in Figure 48. All as-sintered $Ti_3(Al_{1-x}Si_x)C_2$ solid solutions have similar grain size, i.e. around 6.6 μm in length and 2.2 μm in width, except $Ti_3Al_{0.8}Si_{0.2}C_2$. In the case of $Ti_3Al_{0.8}Si_{0.2}C_2$, the grains were12.7±8.8 μm long and 3.7±1.3 μm wide due to the promoted grain growth at higher sintering temperature ~1550^{o}C. Numerous attempts to optimize sintering conditions and fabricate $Ti_3Al_{0.8}Si_{0.2}C_2$ samples with high purity but grain size of approximately 7 x 3 µm^2 were unsuccessful for the reasons that are not clear at this moment. In addition, selected $Ti_3(Al_{1-x}Si_x)C_2$ samples were also heat-treated to promote grain growth and make samples with the larger grain sizes for mechanical testing. The heat-treatment conditions and the grain size distribution for coarse grained samples are listed in Table 8 and summarized in Figure 48b, respectively. After heat-treatment, grains in all heat treated samples were measured to be around 25 µm in length and 8 µm in width.

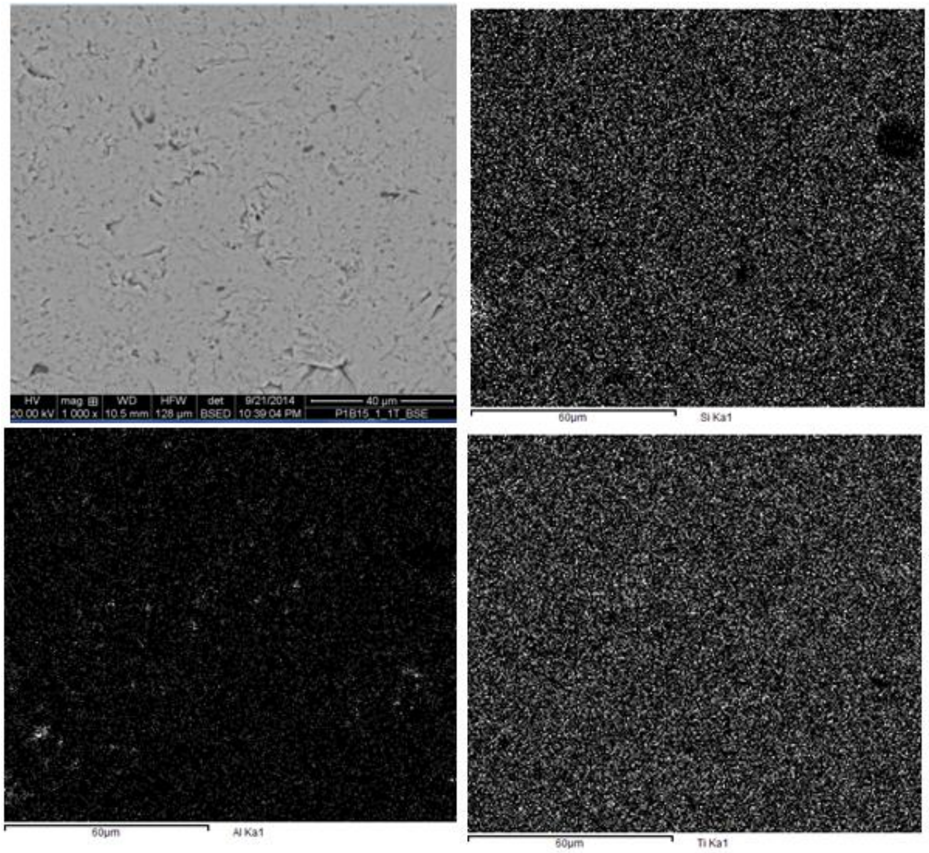

Figure 47 Typical SEM image under back scattered mode (a) of $Ti_3(Al_{0.2}Si_{08})C_2$ and the elemental mapping results (b-d).

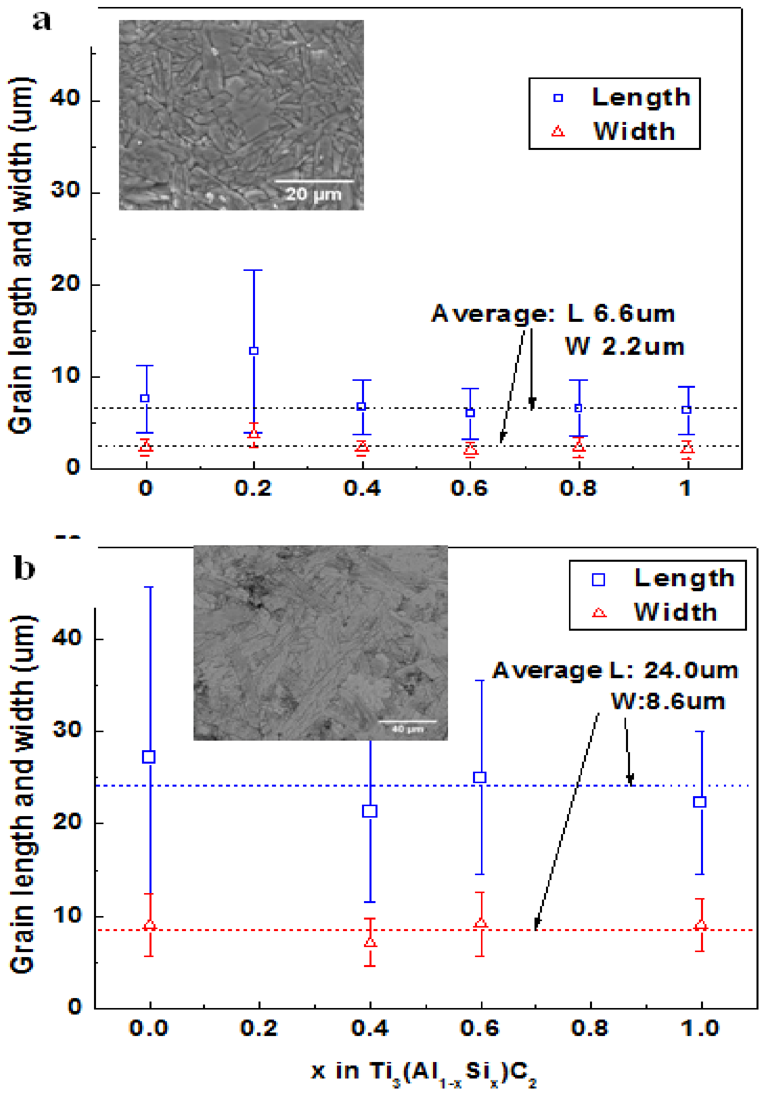

Figure 48 Average grain size (length and width) of (a) as-sintered samples; (b) after additional thermal treatment to promote grain grows. Error bars represent standard deviation. Inserts are typical SEM micrographs of etched surfaces that were used for grain size.

The density and relative density of $Ti_3(Al_{1-x}Si_x)C_2$ samples increases from 4.20±0.03 g/cm^3 to 4.50±0.02 g/cm^3 as the amount of Si element on the A-site increased in solid solutions, showing in Figure 49. The previous result demonstrated that the theoretical densities are 4.25g/cm^3 for Ti_3AlC_2[48] and 4.53 g/cm^3 for Ti_3SiC_2[48], which is in good agreement with our experiment results and show that the relative densities are all above 98%, even up to 99%. Thus, results presented here indicate that PECS is a powerful tool to reaction sinter not only XRD pure, but also almost fully densified MAX phase solid solution in a short time (less than 15 minutes per sample) and relatively lower temperature.

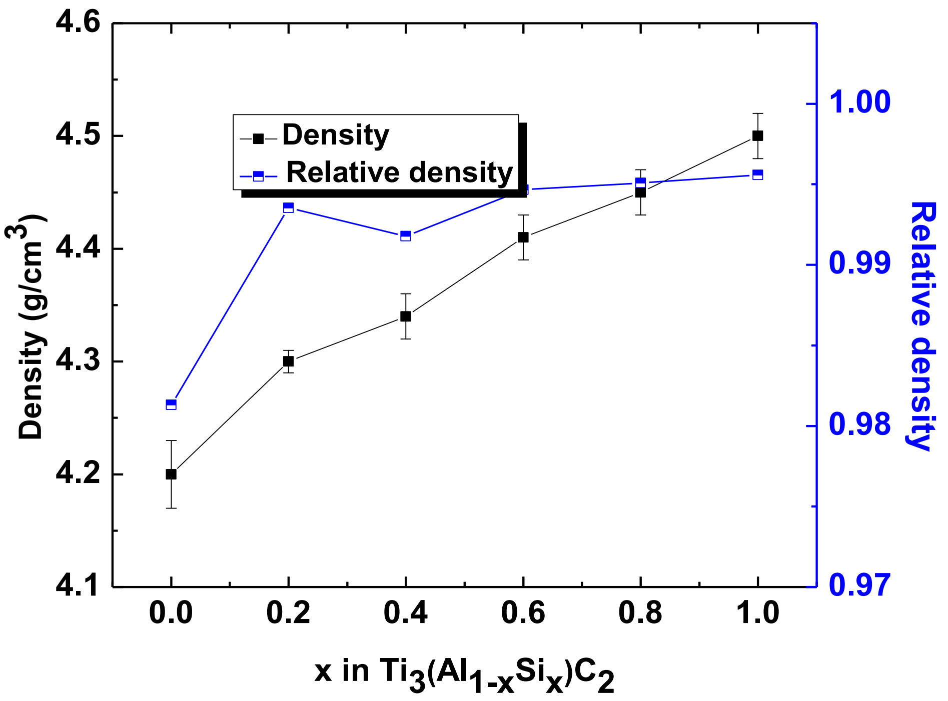

Figure 49 The density and relative density of $Ti_3(Al_{1-x}Si_x)C_2$ MAX phase solid solutions.

4.4.2 Thermal Properties of $Ti_3(Al_{1-x}Si_x)C_2$ Solid Solutions

The heat flow measured using DSC and calculated specific heat capacity at constant pressure (c_p) are plotted in Figure 50 as a function of temperature for $Ti_3(Al_{0.6}Si_{0.4})C_2$ solid solution and the end members. The results in Figure 50 show that heat capacity of the solid solution and two end members are almost identical, and that they increase monotonically with increasing temperature from of 0.5 at -50°C to 0.7 J/(g*K) at 300 °C.

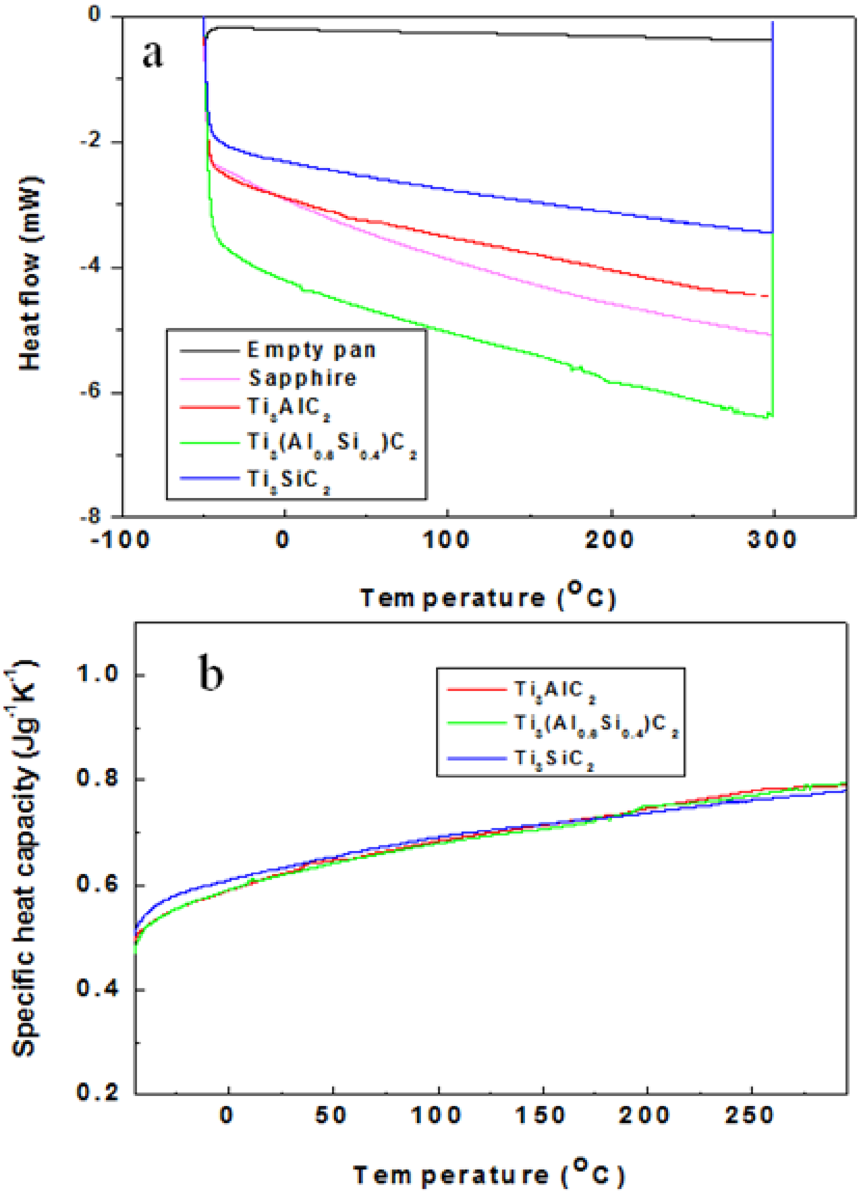

Figure 50 The heat flow (a) and specific heat capacity (b) of as a function of temperature for selected $Ti_3(Al_{1-x}Si_x)C_2$ samples.

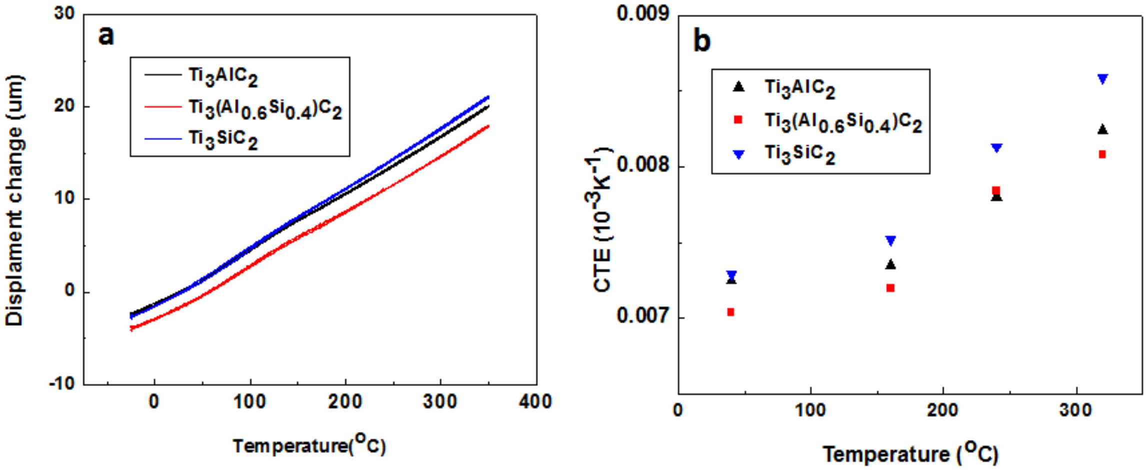

Figure 51 (a) Displacement vs. temperature obtained using TMA in the temperature range of -25 and 350°C and (b) the coefficient of thermal expansion of $Ti_3(Al_{1-x}Si_x)C_2$ and the end members as a function of temperature.

Coefficients of thermal expansion (CTE) at room temperatures were determined form TMA results to be 7.54 x $10^{-6} \pm 0.5 K^{-1}$, 7.66 x $10^{-6} \pm 0.46 K^{-1}$and 7.88 x $10^{-6} \pm 0.59$ K^{-1} for $Ti_3(Al_{0.6}Si_{0.4})C_2$, Ti_3AlC_2 and Ti_3SiC_2, Figure 51. The CTEs of end members are previously reported as ~7-9 x $10^{-6}K^{-1}$[140] for Ti_3SiC_2 and 7 x$10^{-6}K^{-1}$ for Ti_3AlC_2 [7], which fit well with our experimental results. Figure 51 also shows that CTEs of all tested compositions increase slightly with temperature and that their values for solid solution is lower than those of end members at all temperatures. The latter is in good agreement with the first principle calculations [141]. As it was discussed in our previous work [141], the additional valence electron from Si occupies more stable and stronger Ti $_d$–Si $_p$ and Ti $_d$–Al $_p$ covalent bonding states, strengthening a weak inter-planar cohesions between Ti and Al(Si) atomic planes. Then the CTE value of solid solutions would decrease slightly compared with two end members. Those results suggest that CTE decreases slightly with Si substitution, most likely due to stronger Si-Al interactions/bonding in solid solution, than Si-Si or Al-Al in end members.

4.4.3 Elastic Moduli of $Ti_3(Al_{1-x}Si_x)C_2$ Solid Solutions

Figure 52a shows changes of the room temperature Young's (*E*) and shear (*G*) moduli with Si content as determined by Resonant Ultrasound spectroscopy (RUS). E increases linearly from 300 GPa for Ti_3AlC_2 to 325 GPa for Ti_3SiC_2 with increasing amount of as Si on the A site, which is in good agreement with modeling results claimed by Son et al. [128] and Zeng et al. [130]. Shear modulus was also found to increase linearly from 128 GPa to 140 GPa with increasing amount of Si on the A sub-lattice. Results of previous Density Functional Theory also suggested that the observed increase in the elastic moduli with increasing amount of Si on A sub-lattice can be explained by charge density increase near the A element and stronger M-A bonding [128][130].

However, at high temperature, E decreased slightly down with increasing temperature for all solid solutions and end members, without showing any deviation from the monotonic decreasing trend at BTP temperature around 900^oC, like in Figure 52b. It was observed that it is difficult to measure E when the temperature is over 900^oC due to noise at high temperature. Compared with DFT calculation on two end members [138], our experimental results are in good agreement with modeling results that E decreases linearly with temperature increase.

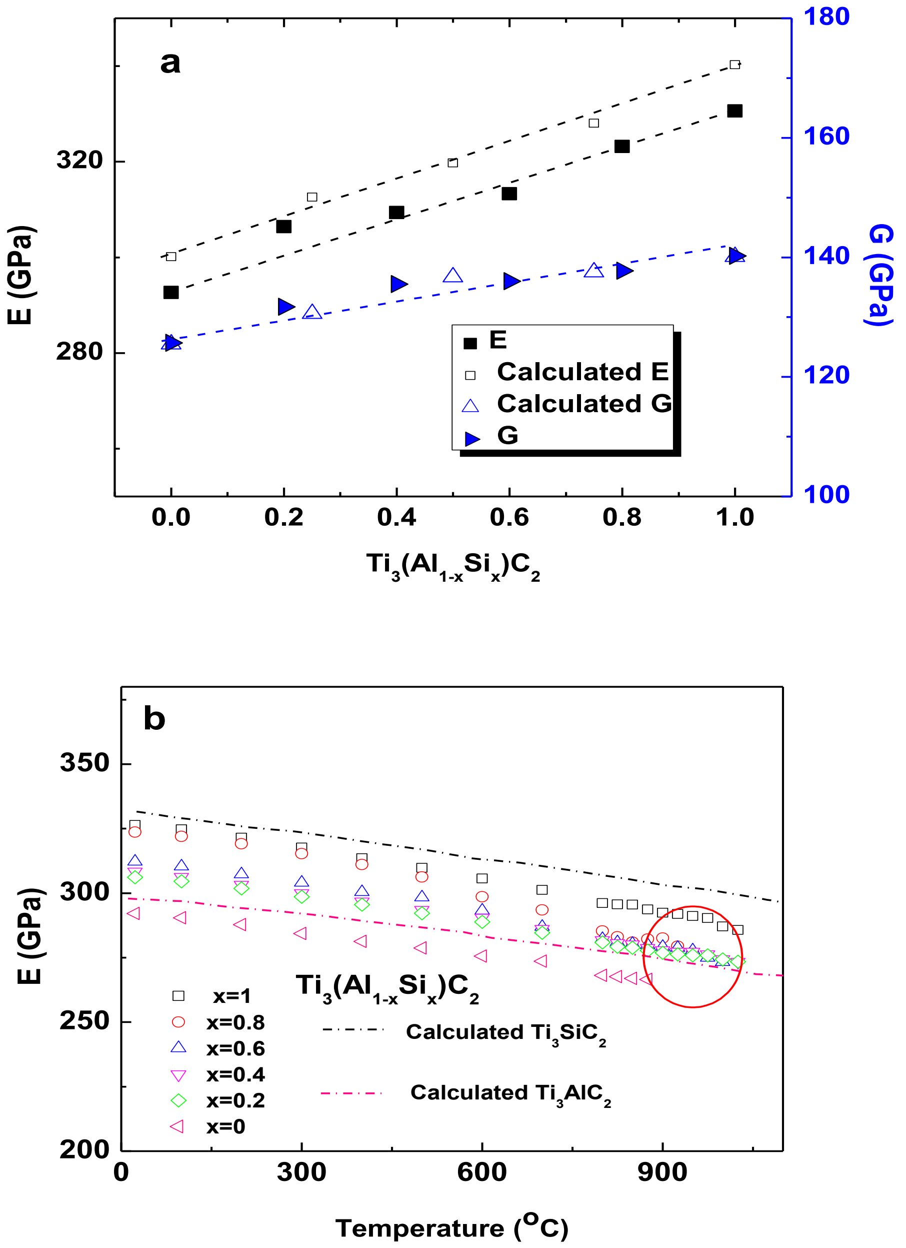

Figure 52 (a) The Young's modulus of $Ti_3(Al_{1-x}Si_x)C_2$ solid solutions as a function of Si content at room temperature, where calculated values are derived from DFT [128]; (b) The Young's modulus of $Ti_3(Al_{1-x}Si_x)C_2$ solid solutions as a function of temperature, where the dash line is the Young's modulus of two end members that are calculated from DFT [124].

4.4.4 Vickers Hardness of $Ti_3(Al_{1-x}Si_x)C_2$ Solid Solutions

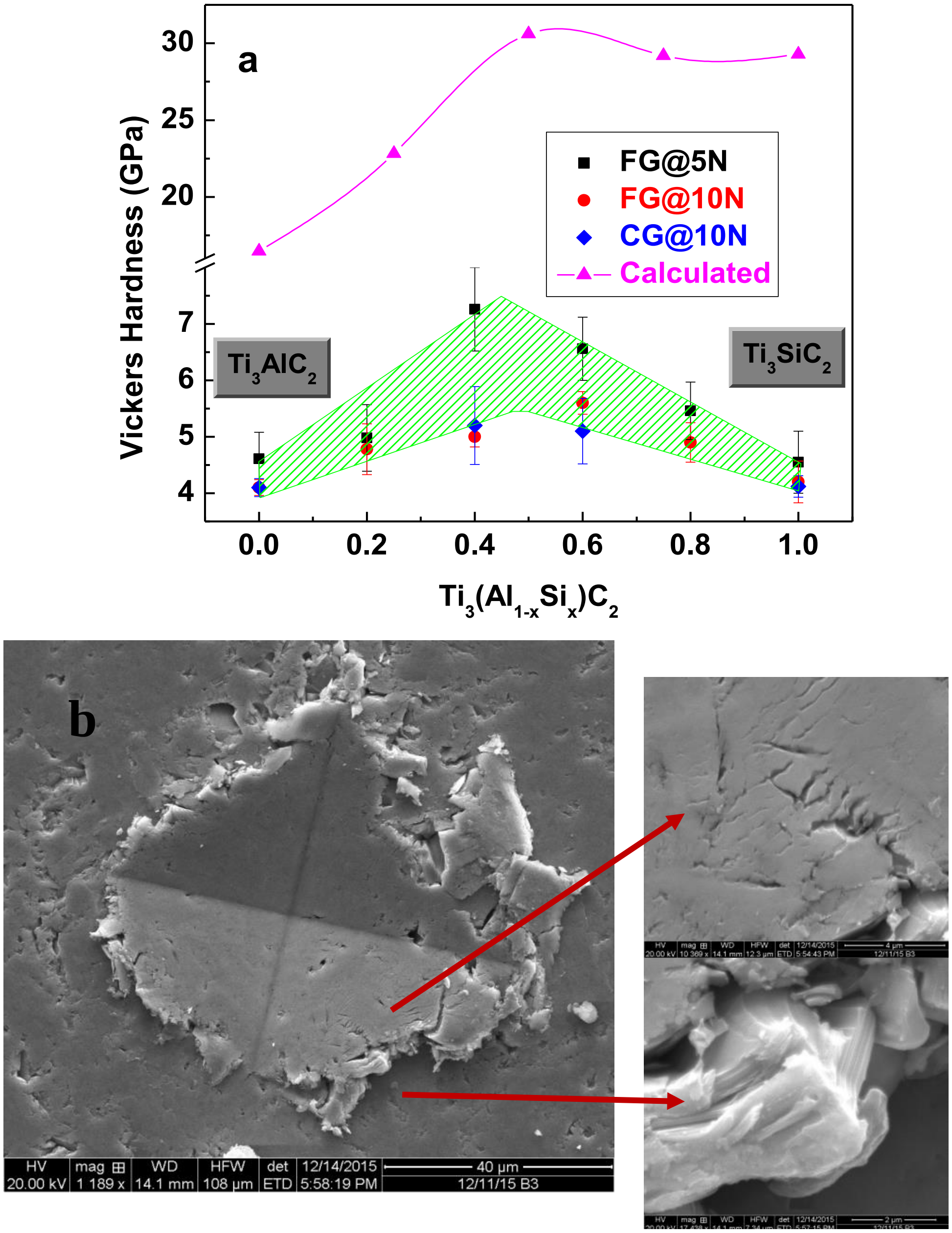

Figure 53 (a) Average Vickers hardness values for FG- and CG- $Ti_3(Al_{1-x}Si_x)C_2$ samples as a function of Si content. Error bars indicate standard deviation from at least 20 measurements. (b) Selected but typical SEM image of the indent in $Ti_3Al_{0.6}Si_{0.4}C_2$ after testing using 10N load.

The Vickers hardness of as-sintered fine-grained (FG) and post heat-treated coarse-grained (CG) samples obtained using indentation loads of 5N and 10N are plotted in Figure 53a as a function of Si content. Vickers hardness increases from 4.2 GPa for Ti_3AlC_2 at the load of 10N, then it reaches value of 5.2 GPa for $Ti_3Al_{0.4}Si0_{.6}C_2$, and at in the end it decreases again to 4.3 GPa for Ti_3SiC_2. As it can be also seen in Figure 53a, both FG- and CG- $Ti_3(Al_{1-x}Si_x)C_2$ solid solutions have almost identical hardness values at all compositions. From the results in Figure 53a the maximum hardness can be located at composition of around x=0.5 at both indentation loads of 5N and 10N, suggesting ideal solid solution hardening behavior.

Figure 53b shows selected but typical the SEM image of the indentation after Vickers testing. As it is typical for MAX phases, a significant deformation by kinking and delamination can be observed around indent (Figure 53b) [142], instead of corner cracks that usually form during indentation in a typical brittle ceramics. This unusual behavior of MAX phases is attributed to the fact that they deform by easy dislocation glide in the basal planes, and by grain backing and kink bend formation during indentation testing [142]. The later, together with the fact that Vickers hardness shows maximum values at x=0.5, suggests that substitution of Al with Si on the A sub-lattice affects dislocation dynamics and results in the ideal solid solution hardening.

According to Density Functional Theory, the intrinsic hardness values are also derived from the cleavage energy between M and A layer under mode I condition Figure 53a, suggesting a solid solution hardening effect in $Ti_3(Al_{1-x}Si_x)C_2$ system. This hardness derived from cleavage is overestimated than Vickers hardness because Vickers hardness is micro hardness and involves several grain instead of M-A layers [131]. It reveals that with addition of Si, Si element contributes more to hardness increasement due to more number of electron. As x is over 0.5, the hardness decreased even though the number of Si increased, that is because Ti-Si bond is becoming weaker and weaker as Si increased [128]. In conclusion, the experimental Vickers hardness and the modeling results share the similar trend that there is a significant solid solution hardening effect regardless of grain size. The hardening effect of $Ti_3(Al_{1-x}Si_x)C_2$ is related to kinking, delimanation, electron number and M-A bond strength .

4.4.5 Mechanical Properties of $Ti_3(Al_{1-x}Si_x)C_2$ Compression

The average compressive strengths of $Ti_3(Al_{1-x}Si_x)C_2$ solid solutions and its end members determined from 3 or 4 tests are plotted in Figure 54, as a function of Si content and grain size. For comparison, compressive strengths of end members reported before are also plotted in the same figure [34, 48, 59, 143, 144]. As it has been already very well established in the case of other MAX phases [33, 35], compressive strength of $Ti_3(Al_{1-x}Si_x)C_2$ solid solutions is a strong function of grain size, with FG samples showing significantly higher compressive strength than the CG ones in Figure 54. Results in Figure 54 also show very mild solid strengthening effect in fine grain samples, with the maximum strength for FG- $Ti_3(Al_{0.6}Si_{0.4})C_2$ that is only 7.3% or 8.8 % higher that of end members. However, Figure 54 also indicates that compressive strength of CG samples is a strong function of Si content as the strengths of CG-$Ti_3(Al_{0.6}Si_{0.4})C_2$ and $Ti_3(Al_{0.4}Si_{0.6})C_2$ solid solutions are improved for more than 25.8% relative to the end members. Figure 55 shows selected but typical photographs of samples after testing in compression and FE-SEM images of fracture surfaces for FG and CG samples. While FG samples shattered in the large number of pieces at the maximum compressive stresses, like typical brittle ceramics, the CG samples show more graceful failure as they fractured by propagation of the major crack in the direction of maximum shear. The SEM images of fracture surfaces in Figure 55 also reveal predominantly brittle failure by delamination in FG samples with very little kinking and grain pull-outs. However, significant deformation of individual grains by kinking can be observed on SEM images of fracture surfaces in CG structures.

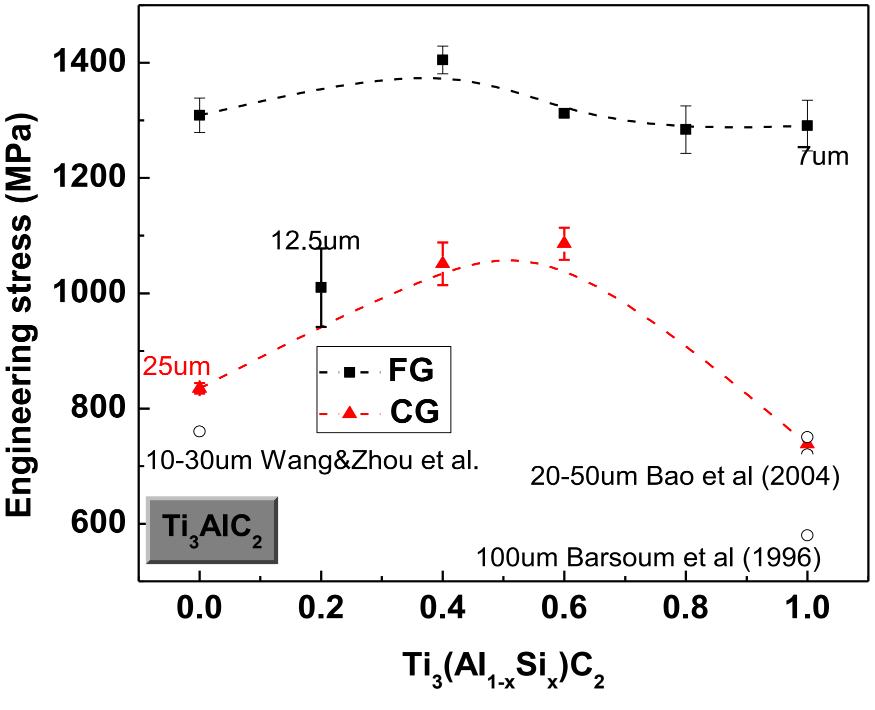

Figure 54 Compressive strength of FG and CG $Ti_3(Al_{1-x}Si_x)C_2$ solid solutions and the end members as a function of Si content. For comparison, compressive strengths of end members from literature are also plotted in this figure. Error bars denote standard deviation from 3-4 tests.

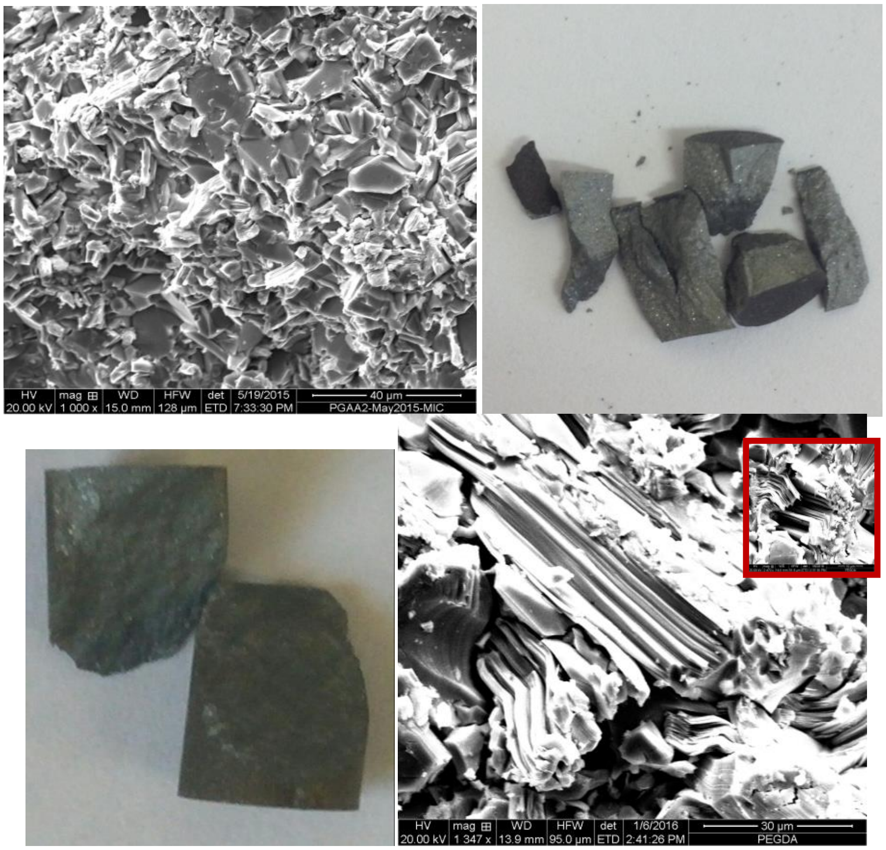

Figure 55 Photographs of the samples after testing in compression and SEM images on the fracture surfaces for (a) FG-Ti_3SiC_2 and (b) CG-$Ti_3Al_{0.6}Al_{0.4}C_2$ solid solution.

When results presented here are put in conjecture with the previous results reporting on the effect of grain size on mechanical properties of MAX phases [2, 33, 59], one can conclude that solid solution can be effectively used to strengthen MAX phases only if they have relatively coarse grained structure. As it was discussed by Benitez et al. [35], very fine grained MAX phases behave more like a typical brittle solids in compression since (i) bucking and kinking of individual grains is difficult, if not impossible; and (ii) they contain more grain boundaries that are effective barriers for dislocation glide in basal planes. Therefore, only moderate solid solution strengthening can be observed in FG structures by alloying on the A site. However, deformation of individual grains by dislocation glide in basal planes and formation of low angle kink boundaries (i.e. dislocation walls) is much easier in CG structures [35], resulting in much stronger solid solutions strengthening effect. The importance of this finding cannot be overemphasized, as it implies that one has to test and compares strengths of samples with the same grin sizes but different composition to make valid conclusion on the solid solution strengthening in the particular MAX solid solutions system.

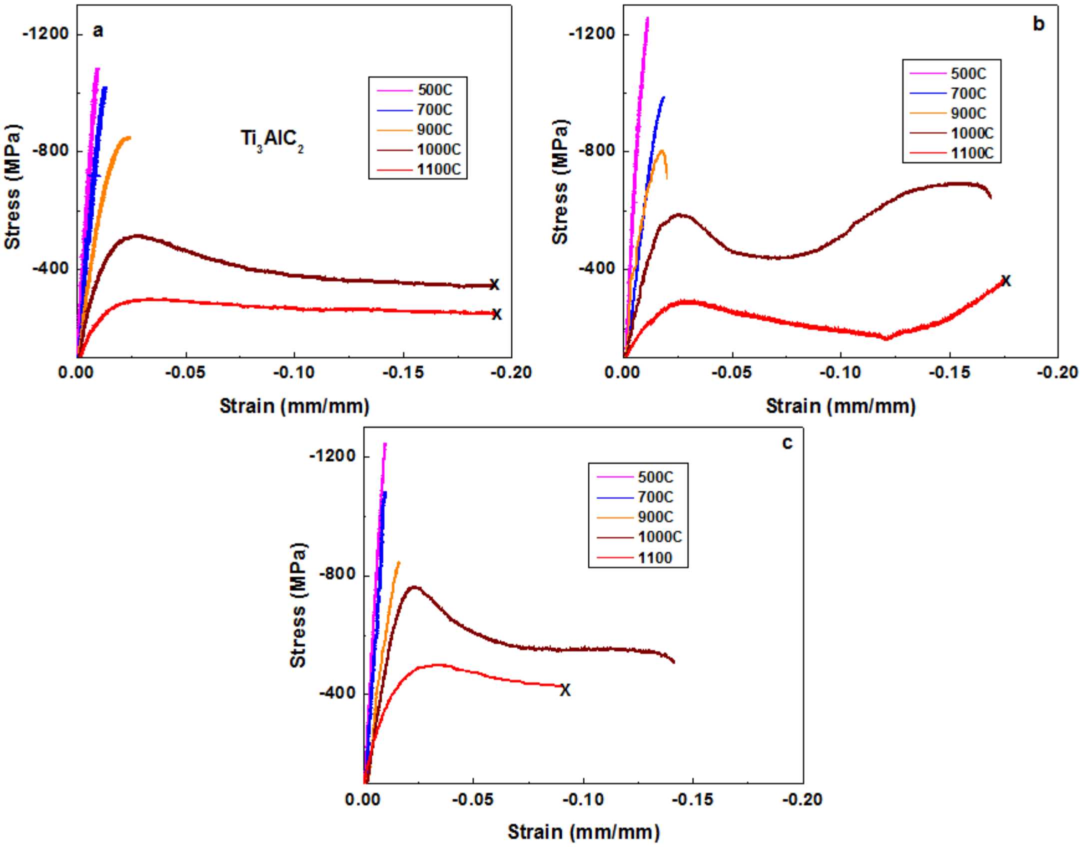

Figure 56 Typical stress-strain curves of $Ti_3(Al_{1-x}Si_x)C_2$ solid solutions at high temperatures, where (a) x=0; (b)x=0.4 and (c) x=1.

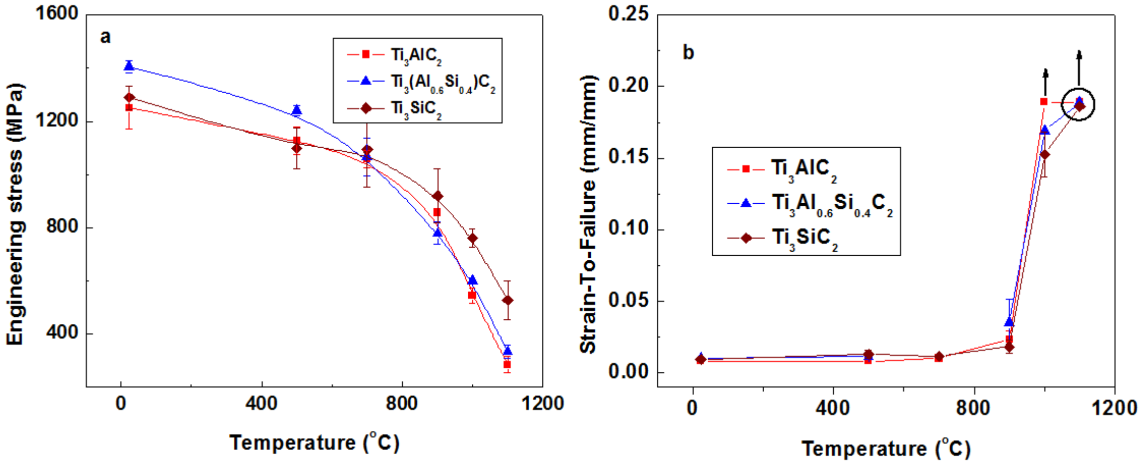

Figure 57 (a) Compressive strength and (b) strain-to-failure of FG of $Ti_3(Al_{1-x}Si_x)C_2$ samples with x =0, 0.4 and 1 as a function of temperature. Error bars show standard deviations calculated from 3 tests. Vertical arrows in (b) denote maximum strains measured that samples are not broken.

Figure 56 shows typical stress-strain curves of high-purity FG $Ti_3(Al_{1-x}Si_x)C_2$ solid solutions obtained in compression in 25°C - 1100°C temperature range. All samples show the BTPT between 700°C and 900°C, below which they fail in the brittle manner. Above BTPT, they filed gracefully with large strains to failure. To further analyze mechanical behavior $Ti_3(Al_{1-x}Si_x)C_2$ solid solutions, the average ultimate compressive strengths and strains to failure were plotted as a function of temperature for x=0, 0.4 and 1 in Figure 57. Figure 57a clearly demonstrates that below 700°C, FG Ti_3AlC_2 and Ti_3SiC_2 with the almost identical grain sizes also have almost identical compressive strength, while $Ti_3Al_{0.6}Si_{0.4}C_2$ solid solution with the same grain size shows slightly higher (~7-8% up 500°C) when compared to the end members. More importantly, Figure 57a shows that:

(i) Compression strength of Al-containing MAX phases, namely Ti_3AlC_2 and $Ti_3Al_{0.6}Si_{0.4}C_2$, decrease more rapidly above BTPT with increasing temperature when compared to Ti_3SiC_2;

(ii) Solid solution strengthening completely diminishes above BTPT temperature, although compressive strength of $Ti_3Al_{0.6}Si_{0.4}C_2$ solid solution is ~17.5% still higher than that of Ti_3AlC_2 at 1100 ^oC, and but still far below that of Ti_3SiC_2;

(iii) Decrease in compressive strength with temperature at around BTPT temperature is more graduately in the solid solution than it the end members.

In the same time, Figure 57b indicate that average strain to failure increase significantly above temperatures between 800 and 900^oC for all compositions, showing slightly lower strains to failure above that temperatures in the samples containing larger amount of Si on A sub-lattice. For example, at 1000^oC, Ti_3AlC_2 deformed up to 19% without failure, $Ti_3Al_{0.6}Si_{0.4}C_2$ failed at 18% and Ti_3SiC_2 failed at 16% stain. In summary, results presented in Figure 57 suggest that around and above BTPT, presence of Al in the A sub-lattice results in easier plastic deformation of individual grains (larger ductility), significant softening, and consequently more pounced decrease in compressive strength. The latter, also leads to the observed gradual weakening of the solid solution strengthening at and around BTPT that was observed in $Ti_3Al_{0.6}Si_{0.4}C_{2.}$ Although the reason for observed effects of Al on the mechanical behavior of $Ti_3Al_{1-x}Si_xC_2$ phases is not completely clear at this point, it should be noted here that both mechanisms proposed to explain BTPT in the MAX phases, namely grain boundary sliding and de-cohesion [2] and activation of secondary slip systems [39] would be most likely unaffected by substitution of Si by Al on the A sub-lattice. Therefore, it can be hypothesized that possible more pronounced softening of Ti-Al bonds in and higher mobility of Al promotes deformation by easier basal plane dislocation glide and formation of dislocation walls and low angle kink boundaries.

4.4.6 Oxidation of $Ti_3(Al_{1-x}Si_x)C_2$ MAX Phase Solid Solutions

To study the oxidation resistance of $Ti_3(Al_{1-x}Si_x)C_2$ solid solutions at elevated temperatures, Ti_3AlC_2, $Ti_3(Al_{0.6}Si_{0.4})C_2$, and Ti_3SiC_2 are selected as candidates to oxidize at 1200°C for 1-100hrs. As discussed before, the oxidation layers are resulted from inward diffusion of oxygen and the simultaneous outward diffusion of titanium, where Al_2O_3 has excellent oxidation resistance and TiO_2 indicates poor oxidation. In this work, we are mainly focusing on the thickness of oxidation layer to represent oxidation resistance and the oxidation kinetics is better described as cubic or nearly cubic according to the previous literatures [42]. Selected but typical FE-SEM images in Figure 58a-c, together with EDS elemental line scans clearly oxidize layer formed Ti_3AlC_2 and $Ti_3(Al_{0.6}Si_{0.4})C_2$ consist of almost pure alumina and have almost identical thickness, while on Ti_3SiC_2, oxides forming very thick oxide layer at the same oxidation time that contains both TiO_2 and SiO_2. A protective nature of alumina layer that forms during oxidation Ti_3AlC_2 and $Ti_3(Al_{0.6}Si_{0.4})C_2$ can be even better illustrated in Figure 58. As it can been seen in that figure, oxidation kinetics of $Ti_3(Al_{0.6}Si_{0.4})C_2$ is almost identical to that of Ti_3AlC_2, and significantly slower than oxidation kinetics of Ti_3SiC_2. Note here, that oxidation kinetic reported here are in good agreement with previously published results [42][145, 146][147]. Results presented here further confirm that $Ti_3(Al_{0.6}Si_{0.4})C_2$

would most likely rather form pure alumina oxide layer than mixed TiO_2, SiO_2 and Al_2O_3 oxide layers, thus providing an excellent oxidation resistance when compared with Ti_3SiC_2 as it was previously postulated elsewhere [125, 136].

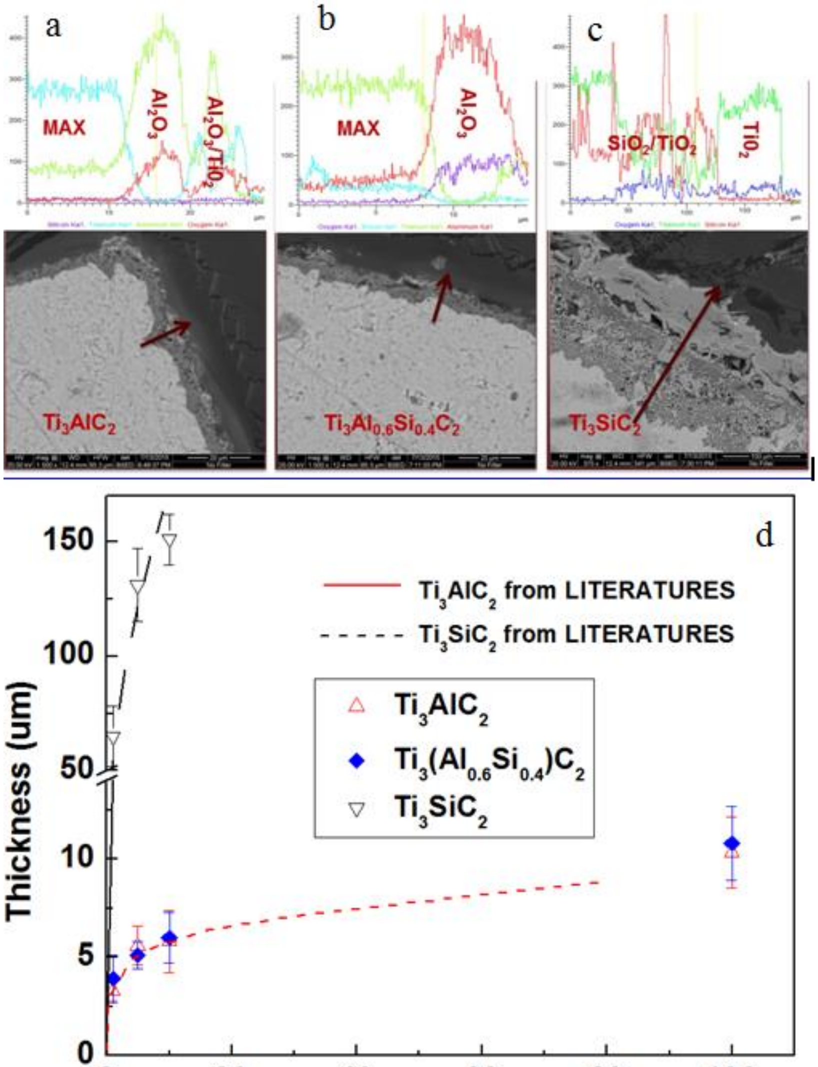

Figure 58 (a), (b) and (c) Backscattered electron FE-SEM images of oxide layers formed after oxidation of Ti_3AlC_2, $Ti_3(Al_{0.6}Si_{0.4})C_2$, and Ti_3SiC_2 respectively, at 1200°C for 10 hours. (d) Thickness of the oxide layer vs. oxidation time at 1200°C. For comparisons, the dash line are previous experimental data for Ti_3AlC_2 from Zhou et al[145, 146] and Ti_3SiC_2 from Barsoum et al[147]

4.5 Conclusion

A series of high-purity $Ti_3(Al_{1-x}Si_x)C_2$ MAX phase solid solutions with x=0, 0.2, 0.4, 0.6, 0.8, and 1 were reaction sintered from Ti, TiC, Al and Si powder mixtures using plus electric current sintering (PECS) in the temperature range of 1500-1600^{o}C. X-ray diffraction results reveled not only the high purity of all processed samples, but also that that the c- lattice parameter decreases linearly with increasing amount of Si on the A sub-lattice while a-lattice parameter reminds almost constant. The elastic moduli of $Ti_3(Al_{1-x}Si_x)C_2$ were found to increase monotonically as x goes from 0 to 1. The specific heat capacity seems to be unaffected by the alloying on the A- site in this MAX phase solid solution system. However, coefficient of thermal expansion (CTE) of $Ti_3Al_{0.6}Si_{0.4}C_2$ solid solution is lower than that of end members, due to stronger Si-Al interactions in A layer.

Regardless of the grain size, $Ti_3(Al_{1-x}Si_x)C_2$ shows ideal solid solution hardening behavior as compositions around x=0.5 have the highest Vickers hardness. However, the solid solution strengthening effect is a strong function of the grain size at room temperature, i.e. it is very mild in the fine grain structures with the maximum strength of solid solutions that is only up to 7.3% higher than that of end members. On the other hand, coarse grained solid solutions shows improved compressive strength for more than 25.8% relative to the end members. However, effects of solid solutions strengthening diminish at around brittle-to-ductile transition temperatures, resulting in lower compressive strength of solid solutions when compared to Ti_3SiC_2, but slightly higher to that of Ti_3AlC_2. Finally, $Ti_3(Al_{1-x}Si_x)C_2$ solid solutions possess excellent oxidation resistance as Ti_3AlC_2 due to the formation of continuous alumina layer on the surface. Results presented here suggest that alloying on the A sub-lattice can be used to strengthen $Ti_3(Al_{1-x}Si_x)C_2$ MAX phases with some limitations; i.e. it is most effective only below brittle-to-plastic transition temperature for coarse grained microstructures. Although $Ti_3(Al_{1-x}Si_x)C_2$ forms protective alumina oxide scale above brittle-to-plastic transition temperature, solid solution strengthening effect above that temperature completely diminishes and their strength is significantly lower than that of the pure Ti_3SiC_2.

5. SUMMARY

This Ph.D. dissertation reports on processing and physical and mechanical properties of Ti_2AlC, alumina fiber-reinforced Ti_2AlC composites and $Ti_3Al_{1-x}Si_xC_2$ MAX phase solid solutions, where x =0-1. The key findings are summarized as followed:

Chapter 2 summarizes results on reaction synthesis of Ti_2AlC from mixture of Ti, Al and TiC powders with the composition of Ti:Al:TiC=1.05:11.05:0.95 by pulse electric current sintering (PECS). It was found that below 900°C, a series of $TiAl_x$ alloys form as a result of reaction between liquid Al and Ti. With increasing temperature, amount of $TiAl_3$, $TiAl_2$ and Ti_3Al decreases as it reacts with Ti to form TiAl. The first MAX phases, namely Ti_2AlC and Ti_3AlC_2 form at 1000°C and 1100°C, respectively as a result of reaction between TiC and TiAl. It was also found that the amount of Ti_2AlC in the final product increases with temperature, up to 1410°C. Regardless of the sintering temperature and conditions, Ti_3AlC_2 was always found as an ancillary impurity phase in the fabricated samples.

After testing powder mixtures with different Ti:Al:C ratios to improve the purity of PECSed Ti_2AlC samples, a powder mixture with non-stoichiometric ratio of Ti:Al:C=2:1.2:0.85 was found to be an optimal and high-purity Ti_2AlC was synthesized from that powder mixture at 1450°C for 15mins. At 1500°C, Ti_2AlC was decomposed into Ti_3AlC_2 because Ti_3AlC_2 was much more thermodynamically stable as a result of more pronounced loss of Al during synthesis.SEM analysis on high-purity Ti_2AlC sample indicated that there are two distinct regains with different morphology: (a)

Ti_2AlC in the middle of the sample and (c) Ti_2AlC+TiC+TiAl around perimeter. The high-purity Ti_2AlC with only 5.2 vol.% TiAl impurity was successfully obtained in the center of PECSed samples with a grain size of 6.9 µm in length and 4.5 µm in thickness. There are two possible reasons for the two microstructural difference from the center to the edge along the diameter of the reaction sintered Ti_2AlC samples: i) temperature gradient; and ii) stress distribution that leads to the extrusion of the liquid phase trough the gap between punch and die. However, since the temperature at the edge was most likely lower than the temperature at the center (1450°C), Ti_2AlC, TiC and TiAl (s) coexist due to the incomplete reaction between TiAl and TiC.

The Vickers hardness fabricated high-purity of Ti_2AlC samples is 4.2±0.3 GPa at the indentation load of 10 N. Fabricated samples have room temperature compressive strengths are of 1200±50 MPa, which is the highest strength of Ti_2AlC ever reported in the literature. This high strength is attributed to the very fine grained structures obtained in PECSing due to suppressed grain growth. Fabricated samples also show good oxidation resistance as they form protective, continuous layer of Al_2O_3 during exposure to high temperatures (1000-1300°C) in ambient air.

Attempts to further improve mechanical properties of Ti_2AlC by substitution of Al with Si were unsuccessful because $Ti_2(Al_{1-x}Si_x)C$ solid solution cannot be sintered from Ti-Al-Si-TiC using PECS as they are thermodynamically unstable. Because mechanical properties Ti_2AlC cannot be improved by substitution of Al with Si, they were reinforced by addition of Nextel^{TM} 720 and Nextel^{TM} 610 alumina fibers. 20vol.% of Nextel^{TM} 720-Ti_2AlC and 20vol.% of Nextel^{TM} 610-Ti_2AlC composites were uniform distribution of short fibers were successfully fabricated using colloidal processing and densification through PECS. Results presented in Chapter 3 provide more details on fabrication of alumina fiber reinforced Ti_2AlC composites and their mechanical properties. Addition of Nextel^{TM} 720_f and Nextel^{TM} 610_f short fibers (~150 μm in length) into the Ti_2AlC matrix results in minor increase of stiffness (i.e. Young's modulus increases for less than 4.5%). However, fabricated composites where found he have improved hardness for more than 35.8% when compared to the pure Ti_2AlC. Room temperature compressive strengths of 20vol.% Nextel^{TM} 720_f-Ti_2AlC and 20 vol.% Nextel^{TM} 610_f-Ti_2AlC, composites were found to be higher than that of Ti_2AlC for more than 26.5% and 14.7%, and 26.4% and 16.9% in both quasi-static and dynamic conditions, respectively. In addition, the room temperature fracture toughness was improved for 21.1% and 15.9% in both 20vol.% Nextel^{TM} 720_f-Ti_2AlC and 20vol.% Nextel^{TM} 610_f-Ti_2AlC composites, respectively. Improved mechanical properties can be attributed to the crack deflections at the fiber-matrix interface and some moderate fiber pull outs.

Finally, Chapter 4 presents results on fabrication and mechanical properties of $Ti_3(Al_{1-x}Si_x)C_2$ solid solutions with x=0-1. In the attempt to evaluate effect of solid solution strengthening in one of the most studied MAX phase, a series of high-purity $Ti_3(Al_{1-x}Si_x)C_2$ solid solutions are successfully fabricated from Ti, Al, Si and TiC powders using PECSing. With Si substitution on Al sites, c-lattice parameter decreased linearly while a-lattice parameter almost remained constant. At room temperature, Young's modulus increased linearly with the amount of Si substitution on Al sites in

Ti_3AlC_2, from 290 GPa for Ti_3AlC_2 to 320 GPa for Ti_3SiC_2. Those experimental finding were also confirmed by ab initio modeling using Density Functional Theory (DFT). With increasing temperature, Young's modulus of all $Ti_3(Al_{1-x}Si_x)C_2$ solid solutions decreased slightly, without showing any deviation from the monotonic decreasing trend at BTPT around 900^{o}C. It was also found that coefficient of thermal expansion of $Ti_3(Al_{0.6}Si_{0.4})C_2$ was lower than that of two end members. Lower thermal expansions in solid solutions can be explained by stronger Si-Al interactions/bonding, than Si-Si or Al-Al ones in the end members. Regardless of grain size, a significant hardening is observed in both FG- and CG-$Ti_3(Al_{1-x}Si_x)C_2$ solid solutions, showing a maximum value at x =0.5. At the same trend has been observed in for calculated intrinsic hardness derived from the cleavage energy using DFT calculations. At room temperature, the strengthening effect was found to be marginal for fine grained (FG) structures, as the compressive strength of $Ti_3Al_{0.6}Si_{0.4}C_2$ and $Ti_3Al_{0.4}Si_{0.6}C_2$ is higher for only 7.3% when compared to the end members. However, significant strengthening effect was observed in CG structures as the room temperature compressive strength of solid solutions excides those of end members for more than 25.8%. Nevertheless, above brittle-to-plastic transition temperature, the solid solution strengthening effect diminishes and the strength of Ti_3SiC_2 is higher than that of Ti_3AlC_2 and solid solutions. Finally, it was found that $Ti_3Al_{0.6}Si_{0.4}C_2$ like pure Ti_3AlC_2 forms protective alumina oxide layer at 1200^{o}C, rather than silica that is commonly found on oxidized surfaces of Ti_3SiC_2.

Based on the results presented in this dissertation work, future work on improving mechanical properties of the MAX phases with the great potential for structural applications in extreme environments, such as Ti_2AlC, Ti_3AlC_2, Cr_2AlC, etc., should target following:

- *Improve mechanical properties of Ti_2AlC by alloying on M site instead of A site*. As mechanical properties of the MAX phases are governed mostly by cleavage of M-A bonds and dislocation dynamics in those planes, one can alter their mechanical properties not only by solid solutions on the A site, but also on the M site. As number of elements that can occupy M site in the MAX phases is significantly larger than that occupying A site, it is reasonable to assume that solid solutions on M site would provide even more possibilities of solid solutions strengthening of the MAX phases.
- *Evaluate effects of size and amount of alumina fibers in alumina fiber reinforced MAX phase composites*. Results presented here suggest that mechanical properties can be further improved by increasing amount of the fibers. In addition, since improved mechanical properties of Ti_2AlC reinforced by alumina fibers can be partially attributed to the observed fiber pull out mechanism, it is reasonable to expect that those properties can be further improved by using longer reinforcement fibers or by better control of the fiber-matrix interfaces.
- *Explore combination of strengthening mechanisms in the MAX phases*. For example, mechanical properties of the MAX phases can be further improved by both solid solution on M and A site, or perhaps by combination of solid solution strengthening, dispersion strengthening and/or ceramic fiber reinforcement.

- *Determine effects of solid solution strengthening and fiber reinforcement on the creep and fatigue of MAX phases*. If MAX phases are going to be used as structural materials for extreme environments (high temperatures, oxidizing/reducing environments), better understanding of creep and fatigue properties of strengthened MAX phases is needed.

REFERENCES

[1] Barsoum MW. The $M_{n+1}AX_n$ phases: A new class of solids: thermodynamically stable nanolaminates. Progress in Solid State Chemistry. 2000;28:201-81.

[2] Barsoum MW, Radovic M. Elastic and mechanical properties of the MAX phases. Annual Review of Materials Research. 2011;41:195-227.

[3] Barsoum MW, El-Raghy T. The MAX phases: Unique new carbide and nitride materials. American Scientist. 2001;89:334-43.

[4] Jeitschko W, Nowotny H, Benesovsky F. Kohlenst off haltige ternäre Verbindungen (H-Phase). Monatshefte für Chemie und verwandte Teile anderer Wissenschaften. 1963;94:672-6.

[5] Lane NJ, Naguib M, Lu J, Hultman L, Barsoum MW. Structure of a new bulk Ti5Al2C3 MAX phase produced by the topotactic transformation of Ti_2AlC. Journal of the European Ceramic Society. 2012;32:3485-91.

[6] Naguib M, Bentzel GW, Shah J, Halim J, Caspi EN, Lu J, et al. New solid solution MAX phases: (Ti0.5,V0.5)3AlC_2, (Nb0.5,V0.5)2AlC, (Nb0.5,V0.5)4AlC3 and (Nb0.8,Zr0.2)2AlC. Materials Research Letters. 2014;2:233-40.

[7] Barsoum MW. Physical properties of the MAX phases. In: Editors-in-Chief: KHJB, Robert WC, Merton CF, Bernard I, Edward JK, Subhash M, et al., editors. Encyclopedia of Materials: Science and Technology (Second Edition). Oxford: Elsevier; 2006. p. 1-11.

[8] Farber L. Transmission electron microscopy study of a low-angle boundary in plastically deformed Ti3SiC2. Philosophical magazine letters. 1999;79:163-70.

[9] Barsoum MW. MAX phases properties of machinable ternary carbides and nitrides introduction. Oxford: Blackwell Science Publ; 2013.

[10] Farber L, Barsoum MW, Zavaliangos A, El-Raghy T, Levin I. Dislocations and stacking faults in Ti3SiC2. Journal of the American Ceramic Society. 1998;81:1677-81.

[11] Barsoum M, Farber L, El-Raghy T. Dislocations, kink bands, and room-temperature plasticity of Ti3SiC2. Metallurgical and Materials Transactions A. 1999;30:1727-38.

[12] Joulain A, Thilly L, Rabier J. Revisiting the defect structure of MAX phases: the case of Ti4AlN3. Philosophical Magazine. 2008;88:1307-20.

[13] Barsoum M, El-Raghy T. Room-temperature ductile carbides. Metallurgical and Materials Transactions A. 1999;30:363-9.

[14] Orowan E. A type of plastic deformation new in metals. Nature. 1942;149:643-4.

[15] Barsoum M, Zhen T, Kalidindi S, Radovic M, Murugaiah A. Fully reversible, dislocation-based compressive deformation of Ti3SiC2 to 1 GPa. Nature Materials. 2003;2:107-11.

[16] Radovic M, Barsoum MW. MAX phases: bridging the gap between metals and ceramics. American Ceramics Society Bulletin. 2013;92:20-7.

[17] Zhou AG, Barsoum MW. Kinking nonlinear elastic deformation of Ti3AlC2, Ti2AlC, Ti3Al(C0.5,N0.5)2 and Ti2Al(C0.5,N0.5). Journal of Alloys and Compounds. 2010;498:62-70.

[18] Barsoum MW, Zhen T, Zhou A, Basu S, Kalidindi SR. Microscale modeling of kinking nonlinear elastic solids. Physical Review B. 2005;71:134101.

[19] Callister WD, Rethwisch D. Materials science and engineering: an introduction. New York: John Wiley & Sons; 2007.

[20] Radovic M, Barsoum MW. Mechanical properties of the MAX phases. Encyclopedia of Materials: Science and Technology. 2004:1-16.

[21] Radovic M, Barsoum M, El-Raghy T, Wiederhorn S, Luecke W. Effect of temperature, strain rate and grain size on the mechanical response of Ti3SiC2 in tension. Acta Materialia. 2002;50:1297-306.

[22] Zhen T, Barsoum M, Kalidindi S. Effects of temperature, strain rate and grain size on the compressive properties of Ti3SiC2. Acta Materialia. 2005;53:4163-71.

[23] Attenburrow G, Bassett D. Compliances and failure modes of oriented chain-extended polyethylene. Journal of Materials Science. 1979;14:2679-87.

[24] Zaukelies D. Observation of slip in nylon 66 and 610 and its interpretation in terms of a new model. Journal of Applied Physics. 1962;33:2797-803.

[25] Kalidindi S, Zhen T, Barsoum M. Macroscale constitutive modeling of kinking nonlinear elastic solids. Materials Science and Engineering: A. 2006;418:95-8.

[26] Benitez R, Kan W, Gao H, O'Neal M, Proust G, Radovic M. Room temperature stress-strain hysteresis in Ti2AlC revisited. Acta Materialia. 2016;105:294–305.

[27] Frank F, Stroh A. On the theory of kinking. Proceedings of the Physical Society Section B. 1952;65:811.

[28] Fraczkiewicz M, Zhou A, Barsoum M. Mechanical damping in porous Ti3SiC2. Acta Materialia. 2006;54:5261-70.

[29] Hull D, Bacon DJ. Introduction to dislocations: Pergamon Press Oxford; 1984.

[30] Zhou A, Basu S, Barsoum M. Kinking nonlinear elasticity, damping and microyielding of hexagonal close-packed metals. Acta Materialia. 2008;56:60-7.

[31] Barsoum M, Basu S. Kinking nonlinear elastic solids. Encyclopedia of materials: Science and Technology. 2010:1-22.

[32] Zhou A, Brown D, Vogel S, Yeheskel O, Barsoum M. On the kinking nonlinear elastic deformation of cobalt. Materials Science and Engineering: A. 2010;527:4664-73.

[33] El-Raghy T, Barsoum MW, Zavaliangos A, Kalidindi SR. Processing and mechanical properties of Ti3SiC2: II, Effect of grain size and deformation temperature. Journal of the American Ceramic Society. 1999;82:2855-60.

[34] Wang XH, Zhou YC. Microstructure and properties of Ti3AlC2 prepared by the solid–liquid reaction synthesis and simultaneous in-situ hot pressing process. Acta Materialia. 2002;50:3143-51.

[35] Benitez R, Gao H, O’Neal M, Lovelace P, Proust G, Radovic M. Effects of microstructure on the mechanical properties of Ti2AlC in compression. Acta Materialia. 2016;In review.

[36] Barsoum MW, El-Raghy T, Ali M. Processing and characterization of Ti2AlC, Ti2AlN, and Ti2AlC0.5N0.5. Metallurgical and Materials Transactions A. 2000;31:1857-65.

[37] Wan D, Meng F, Zhou Y, Bao Y, Chen J. Effect of grain size, notch width, and testing temperature on the fracture toughness of Ti3Si(Al)C2 and Ti3AlC2 using the chevron-notched beam (CNB) method. Journal of the European Ceramic Society. 2008;28:663-9.

[38] Barsoum MW. The Mn+1AXn phases and their properties. Ceramics Science and Technology: Wiley-VCH Verlag GmbH & Co. KGaA; 2010. p. 299-347.

[39] Guitton A, Joulain A, Thilly L, Tromas C. Evidence of dislocation cross-slip in MAX phase deformed at high temperature. Scientific Reports. 2014;4.

[40] Radovic M, Barsoum M, Ganguly A, Zhen T, Finkel P, Kalidindi S, et al. On the elastic properties and mechanical damping of Ti3SiC2, Ti3GeC2, Ti3Si0. 5Al0. 5C2 and Ti2AlC in the 300-1573 K temperature range. Acta Materialia. 2006;54:2757-67.

[41] Barsoum MW, Salama I, El-Raghy T, Golczewski J, Seifert HJ, Aldinger F, et al. Thermal and electrical properties of Nb2AlC, (Ti,Nb)2AlC and Ti2AlC. Metallurgical and Materials Transactions A. 2002;33:2775-9.

[42] Tallman DJ, Anasori B, Barsoum MW. A critical review of the oxidation of Ti2AlC, Ti3AlC2 and Cr2AlC in air. Materials Research Letters. 2013;1:115-25.

[43] Bai Y, He X, Wang R, Sun Y, Zhu C, Wang S, et al. High temperature physical and mechanical properties of large-scale Ti2AlC bulk synthesized by self-propagating high temperature combustion synthesis with pseudo hot isostatic pressing. Journal of the European Ceramic Society. 2013;33:2435-45.

[44] Mei B, Zhou W, Zhu J, Hong X. Synthesis of high-purity Ti2AlC by spark plasma sintering (SPS) of the elemental powders. Journal of Materials Science. 2004;39:1471-2.

[45] Bai Y, He X, Zhu C, Chen G. Microstructures, electrical, thermal, and mechanical properties of bulk Ti2AlC synthesized by self-propagating high-temperature combustion synthesis with pseudo hot isostatic pressing. Journal of the American Ceramic Society. 2012;95:358-64.

[46] Yu W, Gauthier-Brunet V, Cabioc'h T, Dubois S. Synthesis and microstructural characterization of substoichiometric Ti2Al(CxNy) solid solutions and related Ti2AlCx and Ti2AlN end-members. Journal of the American Ceramic Society. 2014;97:2308-13.

[47] Pietzka MA, Schuster JC. Summary of constitutional data on the Aluminum-Carbon-Titanium system. Journal of Phase Equilibria. 1994;15:392-400.

[48] Tzenov NV, Barsoum MW. Synthesis and characterization of Ti3AlC2. Journal of the American Ceramic Society. 2000;83:825-32.

[49] Zhou A, Wang C-A, Hunag Y. Synthesis and mechanical properties of Ti3AlC2 by spark plasma sintering. Journal of Materials Science. 2003;38:3111-5.

[50] Wang XH, Zhou YC. Solid-liquid reaction synthesis and simultaneous densification of polycrystalline Ti2AlC. Zeitschrift für Metallkunde. 2002;93:66-71.

[51] Pang WK, Low IM, O’Connor BH, Sun ZM, Prince KE. Oxidation characteristics of Ti3AlC2 over the temperature range 500–900°C. Materials Chemistry and Physics. 2009;117:384-9.

[52] Song GM, Pei YT, Sloof WG, Li SB, De Hosson JTM, van der Zwaag S. Oxidation-induced crack healing in Ti3AlC2 ceramics. Scripta Materialia. 2008;58:13-6.

[53] Lu X, Zhou Y. Pressureless sintering and properties of Ti3AlC2. International Journal of Applied Ceramic Technology. 2010;7:744-51.

[54] Zhou A, Wang C-a, Huang Y. A possible mechanism on synthesis of Ti3AlC2. Materials Science and Engineering: A. 2003;352:333-9.

[55] Zou Y, Sun Z, Tada S, Hashimoto H. Synthesis reactions for Ti3AlC2 through pulse discharge sintering Ti/Al4C3/TiC powder mixture. Scripta Materialia. 2006;55:767-70.

[56] Han J-H, Hwang S-S, Lee D, Park S-W. Synthesis and mechanical properties of Ti3AlC2 by hot pressing TiCx/Al powder mixture. Journal of the European Ceramic Society. 2008;28:979-88.

[57] Zhou W, Mei B, Zhu J. Fabrication of high-purity ternary carbide Ti3AlC2 by spark plasma sintering (SPS) technique. Ceramics International. 2007;33:1399-402.

[58] Ge Z, Chen K, Guo J, Zhou H, Ferreira JMF. Combustion synthesis of ternary carbide Ti3AlC2 in Ti–Al–C system. Journal of the European Ceramic Society. 2003;23:567-74.

[59] Barsoum MW, El-Raghy T. Synthesis and characterization of a remarkable ceramic: Ti3SiC2. Journal of the American Ceramic Society. 1996;79:1953-6.

[60] Zhang ZF, Sun ZM, Hashimoto H. Rapid synthesis of ternary carbide Ti3SiC2 through pulse-discharge sintering technique from Ti/Si/TiC powders. Metallurgical and Materials Transactions A. 2002;33:3321-8.

[61] Pampuch R, Lis J, Stobierski L, Tymkiewicz M. Solid combustion synthesis of Ti3SiC2. Journal of the European Ceramic Society. 1989;5:283-7.

[62] Zhou Y, Sun Z. Crystallographic relations between Ti3SiC2 and TiC. Material Research Innovations. 2000;3:286-91.

[63] Tokita M. Development of large-size ceramic/metal bulk FGM fabricated by spark plasma sintering. Materials Science Forum. 1999;308-311:83-8.

[64] Finkel P, Barsoum MW, El-Raghy T. Low temperature dependencies of the elastic properties of Ti4AlN3,Ti3Al1.1C1.8, and Ti3SiC2. Journal of Applied Physics. 2000;87:1701-3.

[65] Wang XH, Zhou YC. High-temperature oxidation behavior of Ti2AlC in air. Oxidation of Metals. 2003;59:303-20.

[66] Tian W, Sun Z, Du Y, Hashimoto H. Synthesis reactions of Cr2AlC from Cr-Al4C3-C by pulse discharge sintering. Materials Letters. 2008;62:3852-5.

[67] Wang XH, Zhou YC. Layered machinable and electrically conductive Ti2AlC and Ti3AlC2 ceramics: a Review. Journal of Materials Science &Technology. 2010;26:385-416.

[68] Radovic M, Barsoum MW, El-Raghy T, Wiederhorn SM. Tensile creep of coarse-grained Ti3SiC2 in the 1000-1200 degrees C temperature range. Journal of Alloys and Compounds. 2003;361:299-312.

[69] Zhen T, Barsoum MW, Kalidindi SR, Radovic M, Sun ZM, El-Raghy T. Compressive creep of fine and coarse-grained T3SiC2 in air in the 1100-1300 degrees C temperature range. Acta Materialia. 2005;53:4963-73.

[70] Sun ZM. Progress in research and development on MAX phases: a family of layered ternary compounds. International Materials Reviews. 2011;56:143-66.

[71] Panigrahi BB, Chu M-C, Kim Y-I, Cho S-J, Gracio JJ. Reaction synthesis and pressureless sintering of Cr2AlC powder. Journal of the American Ceramic Society. 2010;93:1530-3.

[72] Yang SL, Sun ZM, Hashimoto H. Formation of Ti3SiC2 from Ti-Si-TiC powders by pulse discharge sintering (PDS) technique. Materials Research Innovations. 2003;7:225-30.

[73] Zhou WB, Mei BC, Zhu JQ, Hong XL. Rapid synthesis of Ti2AlC by spark plasma sintering technique. Materials Letters. 2005;59:131-4.

[74] Wang P, Mei B, Hong X, Zhu J, Zhou W. Fabrication of Ti2AlC by spark plasma sintering from elemental powders and thermodynamics analysis of Ti-Al-C system. Journal of Wuhan University of Technology-Materials Science Edition. 2007;22:325-8.

[75] Zhang MX, Chang YA. Phase diagrams of Ti-AL-C, Ti-Y-O, Nb-Y-O, and Nb-Al-O at 1100 °C. Journal of Phase Equilibria. 1994;15:470-2.

[76] Spencer CB, Córdoba JM, Obando N, Sakulich A, Radovic M, Odén M, et al. Phase evaluation in Al2O3 fiber-reinforced Ti2AlC during sintering in the 1300°C–1500°C temperature range. Journal of the American Ceramic Society. 2011;94:3327-34.

[77] Ingason AS, Mockute A, Dahlqvist M, Magnus F, Olafsson S, Arnalds UB, et al. Magnetic self-organized atomic laminate from first principles and thin film synthesis. Physical Review Letters. 2013;110:195502.

[78] Lin S, Tong P, Wang BS, Huang YN, Lu WJ, Shao DF, et al. Magnetic and electrical/thermal transport properties of Mn-doped Mn+1AXn phase compounds Cr2−xMnxGaC (0 ≤ x ≤ 1). Journal of Applied Physics. 2013;113:-.

[79] Basu S, Obando N, Gowdy A, Karaman I, Radovic M. Long-term oxidation of Ti2AlC in air and water vapor at 1000–1300° C temperature range. Journal of the Electrochemical Society. 2011;159:C90-C6.

[80] Yang H, Pei Y, Rao J, De Hosson JTM. Self-healing performance of Ti2AlC ceramic. Journal of Materials Chemistry. 2012;22:8304-13.

[81] Parrikar PN, Benitez R, Gao H, Radovic M, Shukla A. Mechanical response of fine grained Ti2AlC under extreme thermo-mechanical loading conditions. Materials Science and Engineering: A. 2016;658:176-84.

[82] Tallman DJ, Naguib M, Anasori B, Barsoum MW. Tensile creep of Ti2AlC in air in the temperature range 1000–1150° C. Scripta Materialia. 2012;66:805-8.

[83] Barsoum M, El-Raghy T. A progress report on Ti3SiC2, Ti3GeC2, and the H-phases, M2BX. Journal of Materials Synthesis and Processing. 1997;5:197-216.

[84] Gauthier-Brunet V, Cabioc'h T, Chartier P, Jaouen M, Dubois S. Reaction synthesis of layered ternary Ti2AlC ceramic. Journal of the European Ceramic Society. 2009;29:187-94.

[85] Ivchenko V, Lesnaya M, Nemchenko V, Kosolapova TY. Some physical properties of ternary compounds in the system Ti-Al-C. Powder Metallurgy and Metal Ceramics. 1976;15:367-9.

[86] Bei GP, Gauthier-Brunet V, Tromas C, Dubois S. Synthesis, characterization, and intrinsic hardness of layered nanolaminate Ti3AlC2 and Ti3Al0.8Sn0.2C2 solid solution. Journal of the American Ceramic Society. 2012;95:102-7.

[87] Łopaciński M, Puszynski J, Lis J. Synthesis of ternary titanium aluminum carbides using self-propagating high-temperature synthesis technique. Journal of the American Ceramic Society. 2001;84:3051-3.

[88] Liu G, Chen K, Zhou H, Guo J, Ren K, Ferreira J. Layered growth of Ti2AlC and Ti3AlC2 in combustion synthesis. Materials Letters. 2007;61:779-84.

[89] Cabioc'h T, Eklund P, Mauchamp V, Jaouen M. Structural investigation of substoichiometry and solid solution effects in Ti2Al(Cx,N1−x)y compounds. Journal of the European Ceramic Society. 2012;32:1803-11.

[90] Salama I, El-Raghy T, Barsoum MW. Synthesis and mechanical properties of Nb2AlC and (Ti,Nb)2AlC. Journal of Alloys and Compounds. 2002;347:271-8.

[91] Sun Z, Hashimoto H, Tian W, Zou Y. Synthesis of the MAX phases by pulse discharge sintering. International Journal of Applied Ceramic Technology. 2010;7:704-18.

[92] Zhou W, Mei B, Zhu J, Hong X. Fabrication of high purity dense Ti2AlC-Ti3AlC2 composite by spark plasma sintering method. Journal of Materials Science. 2005;40:3559-60.

[93] Yang F, Kong FT, Chen YY, Xiao SL. Effect of spark plasma sintering temperature on the microstructure and mechanical properties of a Ti2AlC/TiAl composite. Journal of Alloys and Compounds. 2010;496:462-6.

[94] Zou Y, Sun ZM, Hashimoto H, Cheng L. Synthesis reactions for Ti3AlC2 through pulse discharge sintering TiH2/Al/C powder mixture. Journal of Alloys and Compounds. 2009;468:217-21.

[95] Zou Y, Sun Z, Hashimoto H, Tada S. Synthesis of high-purity polycrystalline Ti3AlC2 through pulse discharge sintering Ti/Al/TiC powders. Journal of Alloys and Compounds. 2008;456:456-60.

[96] Zhu J, Qi G, Wang F, Yang H. High purity Ti2AlC powder prepared by a novel method. In: Kim HS, Yang JF, Sekino T, Anpo M, Lee SW, editors. Eco-Materials Processing and Design XI 2010. p. 340-3.

[97] Wang C, Cheng L, Zhao Z. FEM analysis of the temperature and stress distribution in spark plasma sintering: Modelling and experimental validation. Computational Materials Science. 2010;49:351-62.

[98] Wang P, Mei B-c, Hong X-l, Zhou W-b. Synthesis of Ti2AlC by hot pressing and its mechanical and electrical properties. Transactions of Nonferrous Metals Society of China. 2007;17:1001-4.

[99] Gudlur P, Forness A, Lentz J, Radovic M, Muliana A. Thermal and mechanical properties of Al/Al2O3 composites at elevated temperatures. Materials Science and Engineering: A. 2012;531:18-27.

[100] Hashimoto S, Takeuchi M, Inoue K, Honda S, Awaji H, Fukuda K, et al. Pressureless sintering and mechanical properties of titanium aluminum carbide. Materials Letters. 2008;62:1480-3.

[101] Sun ZM, Hashimoto H, Zhang ZF, Yang SL, Tada S. Synthesis and characterization of a metallic ceramic material-Ti3SiC2. Materials Transactions. 2006;47:170-4.

[102] Chen D, Shirato K, Barsoum MW, El-Raghy T, Ritchie RO. Cyclic fatigue-crack growth and fracture properties in Ti3SiC2 ceramics at elevated temperatures. Journal of the American Ceramic Society. 2001;84:2914-20.

[103] Starostina AV, Prikhna TA, Karpets MV, Dub SN, Chartier P, Cabiosh T, et al. Synthesis of ternary compounds of the Ti-Al-C system at high pressures and temperatures. Journal of Superhard Materials. 2011;33:307-14.

[104] Chen JX, Zhou YC. Strengthening of Ti3AlC2 by incorporation of Al2O3. Scripta Materialia. 2004;50:897-901.

[105] Zhang DL, Cai ZH, Huang AJ, Yang R. Synthesis, microstructure, and mechanical properties of a novel Ti2AlC/TiC/Al2O3 in situ composite. Journal of the American Ceramic Society. 2006;89:3325-30.

[106] Spencer CB, Córdoba JM, Obando NH, Radovic M, Odén M, Hultman L, et al. The reactivity of Ti2AlC and Ti3SiC2 with SiC fibers and powders up to temperatures of 1550°C. Journal of the American Ceramic Society. 2011;94:1737-43.

[107] Guo S, Hu C, Gao H, Tanaka Y, Kagawa Y. SiC(SCS-6) fiber-reinforced Ti3AlC2 matrix composites: Interfacial characterization and mechanical behavior. Journal of the European Ceramic Society. 2015;35:1375-84.

[108] Guo S. Improvement of mechanical properties of SiC(SCS-6) fibre-reinforced Ti3AlC2 matrix composites with Ti barrier layer. Journal of the European Ceramic Society. 2016;36:1349-58.

[109] Jeon K. Processing and mechanical properties of Ti2AlC reinforced with alumina fibers. Master thesis. 2011.

[110] Lewis JA. Colloidal processing of ceramics. Journal of the American Ceramic Society. 2000;83:2341-59.

[111] Wilson DM. Statistical tensile strength of NextelTM 610 and NextelTM 720 fibres. Journal of Materials Science. 1997;32:2535-42.

[112] Radovic M, Lara-Curzio E, Riester L. Comparison of different experimental techniques for determination of elastic properties of solids. Materials Science and Engineering: A. 2004;368:56-70.

[113] Naik Parrikar P, Gao H, Radovic M, Shukla A. Static and dynamic thermo-mechanical behavior of Ti2AlC MAX phase and fiber reinforced Ti2AlC composites. In: Song B, Casem D, Kimberley J, editors. Dynamic Behavior of Materials, Volume 1: Springer International Publishing; 2015. p. 9-14.

[114] Kuhn H, Medlin D. ASM Handbook, Volume 08 - Mechanical Testing and Evaluation. ASM International.

[115] Radovic M, Lara-Curzio E. Mechanical properties of tape cast nickel-based anode materials for solid oxide fuel cells before and after reduction in hydrogen. Acta Materialia. 2004;52:5747-56.

[116] Radovic M, Lara-Curzio E, Nelson G. Fracture toughness and slow crack growth behavior of Ni-YSZ and YSZ as a function of porosity and temperature. Advances in Solid Oxide Fuel Cells II: Ceramic Engineering and Science Proceedings: John Wiley & Sons, Inc.; 2008. p. 373-81.

[117] Wilson D, Visser L. High performance oxide fibers for metal and ceramic composites. Composites Part A: Applied Science and Manufacturing. 2001;32:1143-53.

[118] Ingason AS, Petruhins A, Dahlqvist M, Magnus F, Mockute A, Alling B, et al. A nanolaminated magnetic phase: Mn2GaC. Materials Research Letters. 2013;2:89-93.

[119] Mockute A, Dahlqvist M, Emmerlich J, Hultman L, Schneider JM, Persson POÅ, et al. Synthesis and ab initio calculations of nanolaminated (Cr,Mn)2AlC compounds. Physical Review B. 2013;87:094113.

[120] Liu Z, Waki T, Tabata Y, Nakamura H. Mn-doping-induced itinerant-electron ferromagnetism in Cr2GeC. Physical Review B. 2014;89:054435.

[121] Zheng L, Wang J, Lu X, Li F, Wang J, Zhou Y. (Ti0.5Nb0.5)5AlC4: A new-layered compound belonging to MAX phases. Journal of the American Ceramic Society. 2010;93:3068-71.

[122] Zhou Y, Meng F, Zhang J. New MAX-phase compounds in the V–Cr–Al–C system. Journal of the American Ceramic Society. 2008;91:1357-60.

[123] Yu W, Li S, Sloof WG. Microstructure and mechanical properties of a Cr2Al(Si)C solid solution. Materials Science and Engineering: A. 2010;527:5997-6001.

[124] Lee JC, Park SW, Lee DB. Oxidation of Ti3Al0.3Si0.7C2 compounds at 900-1200° C in air. Current Nanoscience. 2014;10:97-100.

[125] Zhou YC, Chen JX, Wang JY. Strengthening of Ti3AlC2 by incorporation of Si to form Ti3Al1-xSixC2 solid solutions. Acta Materialia. 2006;54:1317-22.

[126] Szutkowska M, Jaworska L, Boniecki M, Stobierski L, Rozmus M. Mechanical behavior of diamond matrix composites with ceramic Ti3(Si,Ge)C2 bonding phase. International Journal of Refractory Metals and Hard Materials. 2015; 49: 302-306.

[127] Ganguly A, Zhen T, Barsoum MW. Synthesis and mechanical properties of Ti3GeC2 and Ti3(SixGe1−x)C2 (x = 0.5, 0.75) solid solutions. Journal of Alloys and Compounds. 2004;376:287-95.

[128] Son W, Gao H, Duong T, Talapatra A, Radovic M, Arr´oyave R. Effect of the M-A bonds on the mechanical properties in MAX phases. Unpublished paper.

[129] Wang JY, Zhou YC. First-principles study of equilibrium properties and electronic structure of Ti3Si0.75Al0.25C2 solid solution. Journal of Physics: Condensed Matter. 2003;15:5959.

[130] Zeng FJ, Xia QL. First-principles study of electronic structure and elastic properties of Si doping Ti3Al1-xSixC2 solid solutions. Advanced Materials Research: Trans Tech Publ; 2013. p. 122-6.

[131] Ali MS, Islam AKMA, Hossain MM, Parvin F. Phase stability, elastic, electronic, thermal and optical properties of Ti3Al1−xSixC2 (0≤x≤1): First principle study. Physica B: Condensed Matter. 2012;407:4221-8.

[132] Talapatra A, Duong T, Son W, Gao H, Radovic M, Arroyave R. A high throughput combinatorial study of the effect of M site alloying on the solid solution behavior of M2AlC MAX phases. Physical Review B. 2016, under review.

[133] Huang Z, Xu H, Zhai H, Wang Y, Zhou Y. Strengthening and tribological surface self-adaptability of Ti3AlC2 by incorporation of Sn to form Ti3Al(Sn)C2 solid solutions. Ceramics International. 2015;41:3701-9.

[134] Chen JX, Zhou YC. Effect of Si content on the oxidation resistance of Ti3Al1-xSixC2 (x<0.25) solid solutions at 1000–1400°C in air. Oxidation of Metals. 2006;65:123-35.

[135] Lee DB, Nguyen TD, Park SW. High-temperature oxidation of Ti3Al0.5Si0.5C2 compounds between 900 and 1200 °C in air. Journal of Alloys and Compounds. 2009;469:374-9.

[136] Zhang H, Zhou Y, Bao Y, Li M. Improving the oxidation resistance of Ti3SiC2 by forming a Ti3Si0.9Al0.1C2 solid solution. Acta Materialia. 2004;52:3631-7.

[137] Nguyen TD, Park SW, Lee DB. Cyclic-oxidation behavior of Ti3Al0. 7Si0. 3C2 compounds between 900 and 1100° C in air. Oxidation of Metals. 2009;72:299-309.

[138] Son W, Duong T, Talapatra A, Gao H, Radovic M, Arr´oyave R. Ab-initio Investigation of the finite-temperatures structural, elastic, and thermodynamic properties of Ti3AlC2 and Ti3SiC2. Unpublished paper.

[139] Barsoum MW, El-Raghy T, Rawn CJ, Porter WD, Wang H, Payzant EA, et al. Thermal properties of Ti3SiC2. Journal of Physics and Chemistry of Solids. 1999;60:429-39.

[140] Shih C, Meisner R, Porter W, Katoh Y, Zinkle SJ. Physical and thermal mechanical characterization of non-irradiated MAX phase materials (Ti-Si-C and Ti-Al-C systems) Fusion Reactor Materials Program. 2013;55.

[141] Chen JX, Zhou YC, Zhang J. Abnormal thermal expansion and thermal stability of Ti3Al1−xSixC2 solid solutions. Scripta Materialia. 2006;55:675-8.

[142] Molina-Aldareguia JM, Emmerlich J, Palmquist J-P, Jansson U, Hultman L. Kink formation around indents in laminated Ti3SiC2 thin films studied in the nanoscale. Scripta Materialia. 2003;49:155-60.

[143] Barsoum MW, Brodkin D, El-Raghy T. Layered machinable ceramics for high temperature applications. Scripta Materialia. 1997;36:535-41.

[144] Bao Y, Zhang H, Zhou Y. Punch-shear tests and size effects for evaluating the shear strength of machinable ceramics. Zeitschrift für Metallkunde. 2004;95:372-6.

[145] Wang X, Zhou Y. Oxidation behavior of Ti3AlC2 at 1000–1400 C in air. Corrosion Science. 2003;45:891-907.

[146] Wang X, Zhou Y. High-temperature oxidation behavior of Ti2AlC in air. Oxidation of Metals. 2003;59:303-20.

[147] Barsoum M, Ho-Duc L, Radovic M, El-Raghy T. Long time oxidation study of Ti3SiC2, Ti3SiC2/SiC, and Ti3SiC2/TiC composites in air. Journal of the Electrochemical Society. 2003;150:B166-B75.